TECHNISCHE UNIVERSITÄT WIEN
Vienna University of Technology

MEDICAL UNIVERSITY OF VIENNA

DIPLOMARBEIT

An ultra-flexible 3-channel receive-only coil array for 3T magnetic resonance imaging made of coaxial transmission line resonators

zur Erlangung des akademischen Grades

Diplom-Ingenieur

im Rahmen des Studiums

Technische Physik

eingereicht von

Michael Obermann, BSc.

Matrikelnummer 01227331

ausgeführt am Atominstitut der Österreichischen Universitäten
der Fakultät für Physik der Technischen Universität Wien,

in Zusammenarbeit mit der Medizinischen Universität Wien
Zentrum für Medizinische Physik und Biomedizinische Technik,
Abteilung MR Physik, Exzellenzzentrum Hochfeld-MR.

Betreuung
Betreuer: Em.Univ.Prof. Dipl.-Ing. Dr.techn. Gerald Badurek
Mitwirkung: Ass.-Prof. Dipl.-Ing. Dr. Elmar Laistler

Wien, 24.10.2018

Michael Obermann	Gerald Badurek

Contents

Danksagung

Zuallererst möchte ich mich bei Elmar Laistler, der nicht nur mein wichtigster Ansprechpartner war, sondern sich auch für jede auftretende Frage Zeit genommen hat, bedanken. Für die Betreuung seitens der TU Wien danke ich Prof. Gerald Badurek vielmals.
Von meinen KollegInnen möchte ich zuerst Michael Pichler, der bei allen praktischen Belangen jederzeit zur Seite stand, hervorheben. Sigrun Roat danke ich für die Berechnung der „noise correlation matrix“ sowie der „g-factor maps“. Weiters möchte ich mich bei Lena Nohava für die vielen interessanten und hilfreichen Gespräche bedanken. An dieser Stelle will ich außerdem allen weiteren KollegenInnen im MR-Zentrum für die äußerst freundliche und hilfsbereite Atmosphäre danken!

Besonderer Dank gilt natürlich meiner Freundin Anne-Sophie Zechmeister, die während des Entstehens dieser Arbeit nicht nur den Großteil der Betreuung unserer gemeinsamen Tochter Emilia übernommen hat, sondern auch immer die wesentlichste Stütze für mich war. Bei meinen Eltern Regina und Kurt möchte ich mich für den Rückhalt, vor allem während der Studienzeit, bedanken. Außerdem danke ich allen Verwandten und Freunden vielmals für die große Unterstützung unserer Familie. Ohne sie wäre diese Arbeit nicht zustande gekommen.

Diese Diplomarbeit wurde aus Mitteln des FWF in Kooperation mit ANR in Frankreich, mit der Projektnummer I 3618, unterstützt.

Zusammenfassung

Magnetresonanztomographie (MRT) ist ein etabliertes Verfahren in der nicht-invasiven medizinischen Bildgebung mit hohem Weichteilkontrast und dem Vorteil, ohne ionisierende Strahlung zu arbeiten. Zur Anregung der Kernspins sowie zum Empfang des MR Signals werden Hochfrequenzspulen, die ihre Resonanzfrequenz bei der Larmorfrequenz der untersuchten Atomkerne haben, eingesetzt. Ein dynamisches Forschungsfeld ist in diesem Zusammenhang die Verbesserung des erreichten Signal-zu-Rausch-Verhältnisses (SNR). Dazu können mehrere kleine Spulenelemente zu einem sogenannten „Array“ zusammengeschlossen werden. Durch das Verwenden mehrerer Spulen treten unerwünschte Kopplungen untereinander auf, welche sowohl durch eine wohlüberlegte Anordnung der Elemente (geometrisches Entkoppeln) als auch ein geeignetes Interface (Vorverstärker-Entkopplung) auf ein Minimum reduziert werden können. Zusätzlich erhöht sich das SNR, wenn die Spulen möglichst nahe am zu untersuchenden Bereich anliegen. Standardspulen-Arrays aus Kupferdraht haben ein fix angelötetes Interface und sind starr. Auf Grund der unelastischen Anordnung der Spulenelemente ist eine gute geometrische Entkopplung möglich.

In der hier dargelegten Diplomarbeit werden die Entwicklung und der Bau eines ultra-flexiblen, 3-Kanal Empfangsspulen-Arrays für 3 Tesla Magnetresonanztomographie beschrieben. Das Array besteht aus drei sogenannten Koaxialspulen mit jeweils einem eigenen Interface. Im Unterschied zu Standardspulen werden hier Koaxialkabel als Resonator verwendet. Durch Unterbrechungen im Innen- und Außenleiter wird das Dielektrikum zur Kapazität und die gesamte Struktur resonant. Nur am Spulenanschluss sind Lötstellen vorhanden, daher ist dieses Spulendesign weit flexibler als jenes der Standardspulen, welche Kapazitäten innerhalb des Spulendrahtes verlötet haben. Durch die Benützung von sehr dünnen Koaxialkabeln ergeben sich äußerst flexible und zudem sehr leichte Spulen mit vielfältigen neuen Anwendungsmöglichkeiten für die Magnetresonanztomographie. Als Beispiel sei das Bracoil-Projekt angeführt, welches sich mit dem Bau eines Arrays in T-Shirt-Form für Brust-MR beschäftigt. Die flexiblen Elemente passen sich dabei sehr gut der patientenabhängigen Körperform an.

Abstract

Magnetic resonance imaging (MRI) is a well established technique in non-invasive medical imaging with high soft tissue contrast and the advantage of working without ionizing radiation. High-frequency coils are used to excite the nuclear spins as well as to receive the MR signal, which have their resonance frequency at the Larmor frequency of the examined atomic nuclei. A dynamic field of research in this context is the improvement of the achieved signal-to-noise ratio (SNR). For this purpose, several small coil elements can be combined to form a so-called "array". By using several coils, undesired couplings occur between them, which can be reduced to a minimum both by a well-thought-out arrangement of the elements (geometric decoupling) within the array and by an appropriate interface (preamplifier decoupling). In addition, the SNR increases if the coils are close to the area to be investigated. Standard coil arrays made of copper wire have a fixed soldered interface and are rigid. Due to the inelastic arrangement of the coil elements, good geometric decoupling is possible.

The presented diploma thesis describes the development and construction of an ultra-flexible, 3-channel receive-only coil array for 3 Tesla magnetic resonance imaging. The array consists of three so-called coaxial coils, each with its own interface. In contrast to standard coils, coaxial cables are used as resonators. Through gaps of the inner and outer conductor, the dielectric becomes the capacitance and the entire structure resonates. There are only solder joints at the coil terminal, so this coil design is far more flexible than that of the standard coils, which have soldered capacitances inside the coil wire. If very thin coaxial cables are used, extremely flexible and also very light coils can be built with many new application possibilities for magnetic resonance imaging. One example is the Bracoil-project, which deals with the construction of a T-shirt-like array for breast MR. The flexible elements fit very well to the patient's body shape.

Chapter 1

Introduction

Nuclear magnetic resonance (NMR) represents the physical background of the manifold applied technique of magnetic resonance imaging (MRI). This non-ionizing-radiation imaging method was described by both Purcell et al. [1] and Bloch et al. [2] around 1946. Basically, NMR can be understood with the model of the quantum mechanical spin of nuclei. At first, the spins, aligned along a static magnetic field B_0, are in an equilibrium state. After perturbing them with an electromagnetic pulse B_1, the re-alignment can be measured.
Due to the strive for higher resolution and acquisition speed, which is achieved by an increase of signal to noise ratio (SNR), recent scientific development has shown the following tendency on the hardware side: A higher static magnetic field of the scanner as well as specialized coils for various applications, represented by the radiofrequency (RF) coil development. As a consequence of the reduced acquisition time using parallel imaging methods [3], [4], [5], a large scientific growth in RF coil design is obtained. Nowadays, receive-only surface coils are widely used, mostly, in form of an array of coil elements. The neighbouring coil elements are coupling, which is unwanted and must be reduced for a well-performing coil. For conventional loop coils a rigid array structure is obligatory to obtain a robust decoupling.
A new promising method to overcome the rigid structure was described lately by Zhang et al. [6]. Their idea is to use coaxial cables prepared with one gap of the inner and the outer conductor as receive-only RF surface coils. The coils form a self-resonant structure without any additional lumped components. Among others, promising benefits are the low weight and the ultra-flexibility of these coils.

The aim of this thesis is the development of a 3-channel receive-only coil array for a 3 Tesla MR scanner, consisting of three coaxial coils, each connected to a separate interface.
This thesis is structured as follows. Firstly, the second chapter illustrates the basics of the NMR phenomena and gives theoretical background information of radiofrequency coils. The required electromagnetic theory and general information about the resonance phenomenon, are described. Then the tuning and matching, the detuning as well as the decoupling of RF coils are outlined. Subsequently, different RF coil types are introduced, the standard coil as well as transmission line resonators (TLR). It needs to be mentioned, that the focus is on receive-

only surface coils. The new TLR design as described by Zhang et al.[6] using coaxial cables as receive-only surface coils is introduced and compared to standard loop coils.
The third chapter describes the methods used. It gives a description of measurement techniques such as the vector network analyzer, the software employed for impedance calculations, as well as the used components are outlined. Then the development of the single-channel coaxial coil is explained in detail. The characteristics of coaxial coils are studied including the investigation of the shape and the multi-gap resonance frequency dependence. To overcome the restriction in coil diameter for a given resonance frequency of the one-gap coaxial coil, the theoretical model as described by Zhang et al. is extended to a multi-gap coaxial coil model. Subsequently, the interfacing of the coil is presented. A modular interface to investigate tuning, matching and preamplifier decoupling, as well as the development of three compact interfaces is described, before outlining a performance evaluation of the single-channel coaxial coil and a comparison to standard loop coils as well as the MRI test measurements. Also, this chapter illustrates the 3-channel array development, including the layout of the elements within the array, as well as the two- and three-element decoupling. The implementation of the array on textile as well as MRI test measurements with the final array are described in detail in this section. Finally, the fourth chapter shows a detailed description of the results. The last chapter concludes the this thesis, and is structured into summary, discussion, and outlook, which includes the BRACOIL project, where the studied coaxial coils will be implemented as an 32-channel breast array with motion correction in the future.

Chapter 2

Theoretical background

2.1 Nuclear magnetic resonance

Every atomic nucleus has an angular momentum or nuclear spin $\vec{I}$, which is quantized as postulated by quantum physics. The nuclear spin magnitude has discrete values

$$|\vec{I}| = \hbar\sqrt{I(I+1)},$$

where I can either be an integer value, half-integer value or zero according to the number of protons and neutrons the nucleus consists of. The z-component of the nuclear spin $\vec{I}$ is also quantized,

$$I_Z = m\hbar, \quad \text{with} \quad m = -I, -I+1, ..., I-1, I, \tag{2.1}$$

where m refers to the spin quantum number. Due to the rotation of the (charged) protons, a magnetic field is built up which is related to a magnetic moment

$$\vec{\mu} = \gamma\vec{I}, \quad \mu_z = \gamma I_z. \tag{2.2}$$

γ is denoting the gyromagnetic ratio, which describes the ratio of mechanical to electrical properties of the nucleus. Without an external magnetic field $\vec{B}$ the spatial orientation of $\vec{I}$ is random and all 2I + 1 different discrete spin orientations are energetically equal.

However, by applying an external homogeneous static B-field, e.g. in z-direction: $\vec{B_0} = \begin{pmatrix} 0 \\ 0 \\ B_0 \end{pmatrix}$ without loss of generality, the nuclear spin starts to precess around the magnetic field.

$$\omega_0 = \gamma B_0, \tag{2.3}$$

where ω_0 is called the Larmor frequency. As described by the equation, the Larmor frequency depends on the particular nucleus as well as on the external magnetic field. Values of γ and ω_0 for different nuclei and different static magnetic fields are shown in Tab. 2.1.

Isotope	Spin I	Gyromagnetic ratio γ [MHz]	Resonance frequency ω_0 [MHz]		
			B_0 = 1.5 T	B_0 = 3 T	B_0 = 7 T
^{1}H	1/2	42.58	63.87	127.74	298.06
^{23}Na	3/2	11.27	16.905	33.81	78.89
^{31}P	1/2	17.25	25.875	51.75	120.75

Table 2.1: Gyromagnetic ratio and the calculated resonance frequency for different static magnetic fields.

Due to the external magnetic field, the potential energy splits into 2I + 1 equidistant energy levels (Zeeman levels) according to the spin quantum number m. This effect is called the Zeeman effect. In Fig 2.1 (a) the precessing spin $\vec{I}$ in an external B-field is shown, while the splitting of the z-component I_z (b) and the energy levels (c) are shown for the example I = 2.

With Eq. 2.1 and Eq. 2.2 one obtains

$$E_m = -\vec{\mu} \cdot \vec{B_0} = -\mu_z B_0 = -\gamma m \hbar B_0 \tag{2.4}$$

if the magnetic field direction in along the z-axis. With Eq. 2.3 the energy difference between two levels is

$$\Delta E = E_m - E_{m'} = \gamma \hbar B_0 = \hbar \omega_0,$$

According to the selection rules of quantum physics only, a transition between $\Delta m = \pm 1$ is allowed.

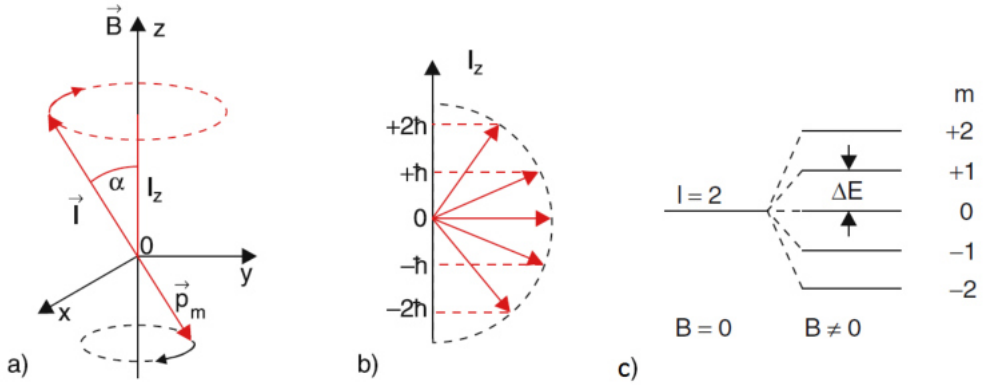

Figure 2.1: The vector model explaining the Zeeman effect. Showing: (a) the nuclear spin $\vec{I}$, (b) its z-component and (c) the energy splitting for I=2. Reproduced from W. Demtröder [7].

For an isolated nucleus in a homogeneous magnetic field the transition between two Zeeman levels is prohibited due to conservation of energy. However, by emitting or absorbing photons a transition is possible. The energy of the photon $E_{RF} = \hbar \omega_{RF}$ must be identical to the energy difference:

$$E_{RF} = \Delta E \quad \Leftrightarrow \quad \hbar \omega_{RF} = \hbar \gamma B_0 \quad \Leftrightarrow \quad \omega_{RF} = \omega_0. \tag{2.5}$$

In nuclear magnetic resonance (NMR) not only one spin but a large collective system of spins is observed. In an external field B_0 the population of the 2I + 1 spin states is described by the Boltzmann statistics. The state with the highest spin number m has the lowest energy. Due to the second law of thermodynamics, (i.e. the principle of minimum energy) this spin state will have a greater occupation number which leads to an macroscopic magnetisation $\vec{M}$. If a static B-field is considered in z-direction the magnetisation is given by the sum of all N magnetic moments,

$$|\vec{M}| = M_z = \sum_i^N (\mu_z)_i = \Delta n \cdot \mu_z,$$

where Δn denotes the difference in population number. Only this additional number of spins lead to a macroscopic magnetisation since the other spins cancel each other out.

As discussed above, the magnetisation $\vec{M}$ precesses along the external magnetic field $\vec{B}$ with the Larmor frequency ω_0. To detect an electromotive force, the equilibrium state as shown in Fig. 2.1 (a) has to be disturbed. This can be achieved by applying a magnetic field $\vec{B_1}$ perpendicular to $\vec{B_0}$ when the frequencies of both B-fields are equal. By applying the magnetic field for a finite time τ, a flip angle

$$\theta = \gamma B_1 \tau$$

is obtained. Whereas the angle of the flipped magnetisation is measured in a rotating reference frame. A very detailed description of the theoretical background (also describing the rotating frame) can be found e.g. in [8].
If a conducting loop is positioned close to the perturbed magnetisation $\vec{M}$, according to Faraday's law, an electomotive force ϵ is induced. The resonance frequency is in the radiofrequency (RF) range for the interesting nuclei in NMR [9], thus, the conducting loop is called radiofrequency coil.

2.2 Radiofrequency coils

A radiofrequency coil basically consists of a resonant circuit. The coils are used to transmit an RF signal into the object of interest and then detect the perturbation of the static magnetic field. The transmit signal, i.e. the magnetic field $\vec{B_1}$ to flip the magnetisation is called Tx-signal. The receive RF signal, used to detect the change in magnetic flux of the object is called Rx-signal. The Tx and Rx coils are designed to perform at the same frequency, respectively. RF coils can either be used for one of the two tasks or they are realized as receive and transmit coil. The focus is laid on receive coils, since the aim of this thesis is the production of a receive coil array.

2.2.1 Electromagnetic background

The magnetic flux Φ_m is defined as the quantity of magnetic field lines through an area, $\Phi_m = \int \vec{B} \cdot d\vec{A}$, where $\vec{B}$ is the magnetic field. According to Faraday's law of induction a change in

magnetic flux through a surface results in an electromotive force ε:

$$\varepsilon = -\frac{d\Phi_m}{dt}. \tag{2.6}$$

A wire which is bent to a coil is imagined. Due to the proportionality of the $\vec{B}$-field and the electric current I_C, which induces this field, a relation between the magnetic flux and the current can be found,

$$\Phi_m = \int \vec{B} \cdot d\vec{A} = L \cdot I_C.$$

The relation is called self-inductance of the coil with the proportionality constant L (inductance) and the SI-unit is Henry (1H = 1V $\cdot$ s/A). All conductors have an inductance, according to their size and shape. By comparing both equations above a relation between the electromotive force and the change of electrical current can be found:

$$\varepsilon = -L\frac{dI_C}{dt}. \tag{2.7}$$

A device of two conducting surfaces which are oppositely charged is called capacitor. The stored potential energy is defined by the capacitance

$$C = \frac{Q_c}{U},$$

with Q_c being the charge and U the voltage between the two surfaces. The SI-unit of the capacitance is Farad (1F = 1C/V). Additionally, a dielectric can be placed between the conducting surfaces to increase the capacitance.

If an alternating current (AC) is applied to an electrical circuit consisting of inductances and/or capacitance a phase displacement φ between U_{AC} and I_{AC} appears. The displacement can be considered by the complex impedance

$$Z = \frac{U_{AC}}{I_{AC}},$$

which is expressed in Ω. It yields $Z = R + iX$, where the real part R is called resistance (R), and the imaginary part X is the reactance. The phase displacement is described by

$$tan(\varphi) = \frac{Im(Z)}{Re(Z)} = \frac{X}{R}.$$

For the impedances of a perfect inductor (Z_L) and capacitor (Z_C) it yields

$$Z_L = i\omega L \quad \text{as well as} \quad Z_C = \frac{1}{i\omega C}, \tag{2.8}$$

where ω describes the angular frequency of the electrical current.

2.2.2 The resonance phenomenon

An electrical circuit connecting only a capacitor and an inductor is considered. At first the entire energy is stored in the capacitor. The capacitor discharges over time and its energy flows into the inductor producing an electromagnetic B-field. Due to the electromagnetic induction (Eq. 2.7) the capacitor is getting charged vice versa. For a lossless consideration the procedure is repeated with the opposite charge in the capacitor as well as opposite direction of the arising B-field. The energy oscillates back and forth between the two components with the so-called resonance frequency.Two basic resonant circuits and their fundamental differences will be described next.

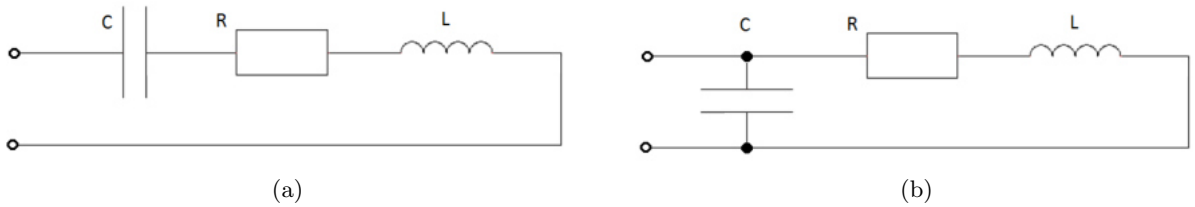

(a) (b)

Figure 2.2: Electrical circuit of a series resonant circuit (a) and a parallel resonant circuit (b).

Series resonant circuit

A sketch of the series resonant circuit can be seen in Fig. 2.2 (a). The total impedance of the RCL-circuit adds to

$$Z_{series} = R + i\omega L + \frac{1}{i\omega C} = R + i\left(\omega L - \frac{1}{\omega C}\right),$$

where R refers to the resistance due to ohmic losses. In case of

$$\omega L = \frac{1}{\omega C} \tag{2.9}$$

the reactances of L and C compensate each other completely and the energy is exchanged between L and C. This condition can only be fulfilled at one particular frequency, the resonance frequency $\omega = \omega_0$.

A chart of the real and the imaginary part of Z_{series} plotted over the frequency ω is shown in Fig. 2.3. Arbitrary values for the resistor R = 5 Ω, the capacitor C = 100 pF, and the inductor L = 100 nH are used. The imaginary part of the impedance has one zero-crossing at the resonance frequency ω_0. The function is monotonically increasing with the frequency. The real part of Z = R is constant for all frequencies.

The impedance compensation is not only feasible for RLC-circuits in series. In fact, the general resonance condition for an electrical circuit consisting of inductances and capacitors is found to be

$$Im\big(Z\big) = 0. \tag{2.10}$$

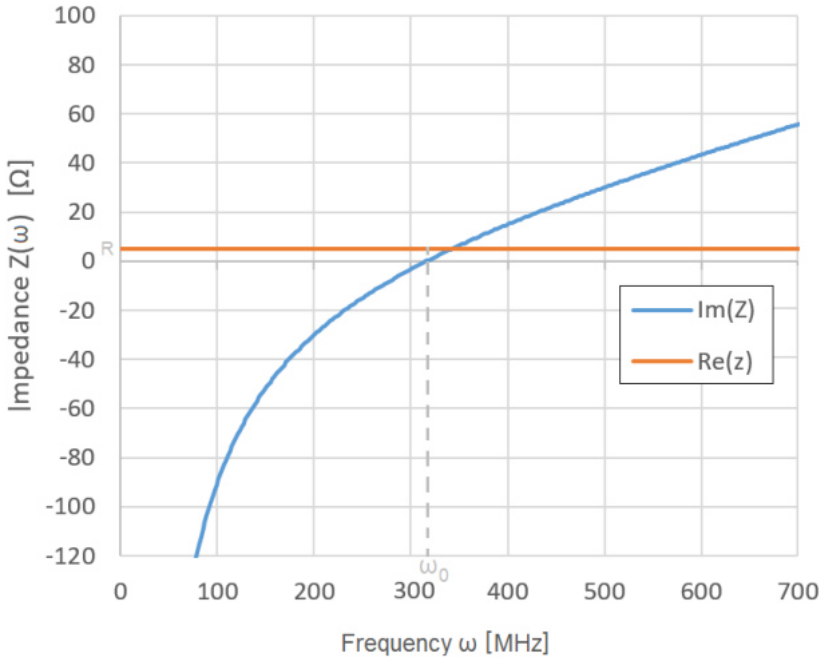

Figure 2.3: Chart of the real and imaginary part of the impedance of a series RLC-circuit.

Parallel resonant circuit

For the parallel resonant circuit, as shown in Fig. 2.2 (b) the total impedance adds to

$$\frac{1}{Z_{parallel}} = \frac{1}{R + i\omega L} + i\omega C.$$

With some algebraic manipulations the total impedance can be split into its real and imaginary part,

$$Z_{parallel} = \frac{\frac{R}{(\omega C)^2}}{R^2 + \left(\omega L - \frac{1}{\omega C}\right)^2} - \frac{i}{\omega C}\,\frac{R^2 + \omega L\left(\omega L - \frac{1}{\omega C}\right)}{R^2 + \left(\omega L - \frac{1}{\omega C}\right)^2},$$

which are plotted in Fig. 2.4 using the same values for R, C and L as described for the series resonant circuit. In contrast to the series RLC-circuit the real part is not constant but rather has one maximum located at the resonance frequency. The imaginary part of the impedance is increasing with ω to a maximum, then decreasing with a zero-crossing to a minimum and afterwards approaching zero.

2.2.3 Characterisation of RF coil performance

SNR

The signal to noise ratio (SNR) is a key parameter to determine the effectiveness of an MR experiment. If the SNR is not high enough, it is impossible to distinguish different tissues.

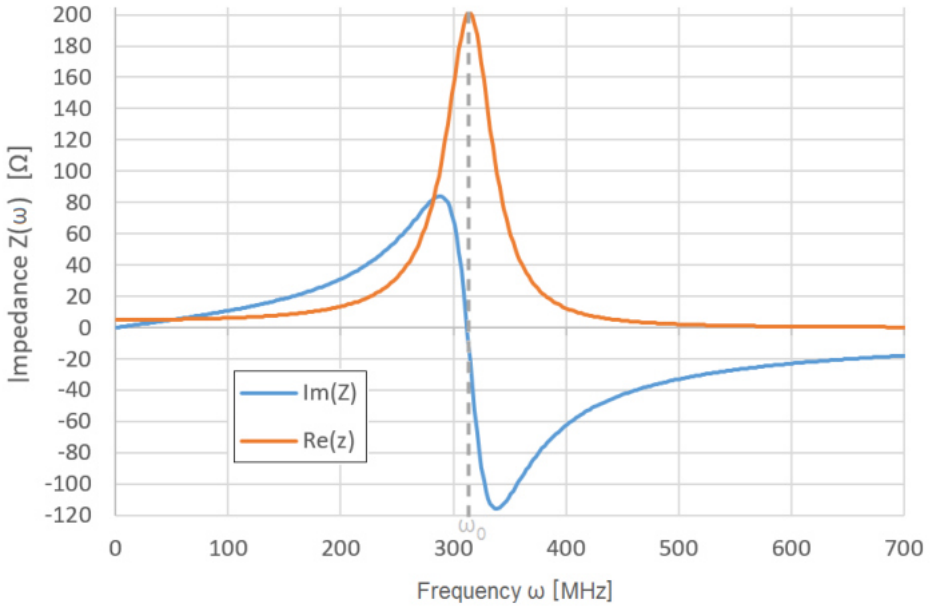

Figure 2.4: Chart of the real and imaginary part of the impedance of a parallel RLC-circuit.

Therefore, a maximum of the SNR is striven. Both, the signal voltage and the noise voltage are determined by the characteristics of the receive coil: The signal of the coil is proportional to the electromotive force ε induced by the varying magnetic flux (Eq. 2.6) of the sample. The noise originates mostly from ohmic losses in the coil electronics and the sample.
The most basic way to calculate SNR for a one-channel coil is to divide the mean signal intensity measured in a region of interest (ROI) by the standard deviation of the signal intensity obtained outside of the sample, where no tissue signal is obtained (noise).

Q-factor

The quality factor (also Q-factor) can be used to estimate and compare the expected sensitivity of the coil. The Q-factor is defined by the fraction of stored magnetic energy to the lost energy due to the coil's resistance, which is related to the dissipated energy. Q is usually measured in two different conditions: in the so-called loaded and unloaded condition, which means the measurement is performed with and without a sample. The unloaded and loaded Q-factor can be expressed by

$$Q_U = \frac{L\omega}{R_c} \quad \text{and} \quad Q_L = \frac{L\omega}{R_c + R_s},$$

where L and R_c are the inductance and the ohmic resistance of the coil. R_s refers to the sample resistance which is added to the coil resistance when it is loaded. Dividing both factors yield

$$\text{Q-ratio} = \frac{Q_U}{Q_L} = \frac{R_c + R_s}{R_c} = 1 + \frac{R_s}{R_c}. \tag{2.11}$$

Q-ratio > 2 is desired, since in that case $R_s > R_c$, i.e., the total noise is dominated by the unavoidable noise of the sample, and further reducing the coil noise will not improve the SNR significantly.

g-factor

As described in Sec. 2.2.7, parallel imaging [3], [4], [5] can be used to accelerate the signal acquisition. The under-sampled image is obtained faster by a fraction R than the fully sampled image with the drawback of a reduced SNR by a factor $1/\sqrt{R}$, where R is the acceleration factor. Generally, there is an additional reduction due to the overlapping coil sensitivity profiles in an array, which is described by a spatial varying geometry factor (g-factor). This leads to the following proportionality between under-sampled and fully sampled SNR:

$$SNR_R = \frac{SNR_{R=1}}{g \cdot \sqrt{R}}. \tag{2.12}$$

The g-factor can be calculated with the so called pseudo multiple replica method as described by Robson et al. [10]. Noise-only data and a non-accelerated image (SNR_{full}) are acquired to calculate accelerated images and the g-factor maps.

2.2.4 Tuning and matching

First, the resonance frequency ω_0 of the RF coil has to be set to the desired Larmor frequency, which depends on the nucleus of interest and the static magnetic field B_0. This method is called tuning of the coil and is obtained by setting the reactance of the electrical circuit to zero (Eq. 2.10).
The signal acquired by the coil is transferred to a preamplifier from where it is further connected to the MR scanner's receiver via coaxial cables. Often, the impedance that needs to be presented at the preamplifier input to obtain the optimal noise figure is $Z_0 = 50\ \Omega$. Also, the most commonly used characteristic impedance of coaxial cables is 50 Ω. Thus, it is necessary to match the purely resistive impedance of coil to that same value,

$$Re(Z) = Z_0 = 50\ \Omega.$$

A sketch showing the impedance transformation of the matching can be seen in Fig. 2.9. The impedance of the coil Z_{coil} is transformed to $Z_{source} = Z_0 = 50\,\Omega$. Without matching the coil to Z_0 reflections occur and create signal loss.
Depending on the electrical circuit of the radiofrequency coil, there are several ways to match a coil, a detailed description can be found [11]. The matching of the two basic RF coil circuits will be described next.

Matching a series resonant circuit

The easiest way to obtain both conditions $Re(Z) = Z_0 = 50\ \Omega$ and $Im(Z) = 0$ at the resonance frequency is to connect a resistance in series to the electrical circuit. The value of this resistance has to be such that it adds with the coil losses to Z_0 in total. For the example described in Sec. 2.2.2 a value of 45 Ω would be necessary. Although the additional resistance shifts the real part of the impedance (Fig. 2.3) to a constant value of 50 Ω as desired, energy would be lost in the additional resistance and noise would be added, drastically degrading the RF coil's performance. Therefore, another scheme is usually employed for the MR coils: the parallel resonant circuit.

Matching a parallel resonant circuit

For the parallel resonant circuit there exists an elegant way to match the circuit to Z_0 without adding noise. By connecting a capacitor C_M in series to the electrical circuit as shown in Fig. 2.5, a shift of the imaginary part of the impedance can be obtained. The capacitor C_M shifts the imaginary part of Z while the real part stays unchanged. A chart of the described situation using the same values for R, L, and C as in Fig. 2.4 and $C_M = 260$ nF can be seen in Fig 2.6. At the resonance frequency ω_0 the resistance $Z_0 = 50\ \Omega$ is obtained.

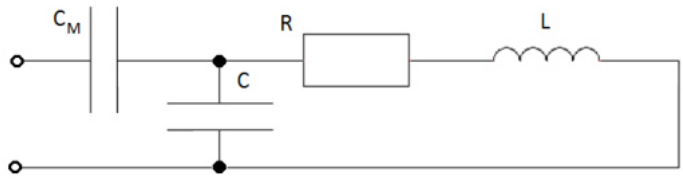

Figure 2.5: Sketch of the parallel RLC-circuit with an additional capacitor C_M in series for matching the coil.

2.2.5 Detuning

During transmission of the RF signal large amounts of energy are sent from the transmit coils into the sample. If the transmit and receive coils are separate coils, it is very important to detune the Rx coils during transmission. Since the resonance frequencies of both, Tx and Rx coils are equal, the Tx signal would be coupled to the receive coils and could destroy its preamplifier. The detuning is commonly realized by creating a high impedance of the receive coil at the Larmor frequency while transmitting the signal.
For standard coils an additional electrical circuit, as shown in Fig. [12], to detune the RF coil while transmitting the signal is connected. It consists of an inductor L an active PIN diode and two RF chokes. During the receive mode the PIN diode is reverse biased, thus being removed from the circuit. By applying a DC signal (V_{dc}) during transmission the PIN diode is switched (forward biased) and creates an additional parallel resonant circuit consisting of L and C_{m2}. This circuit in combination with the RF coil circuit produce two resonances, both shifted from

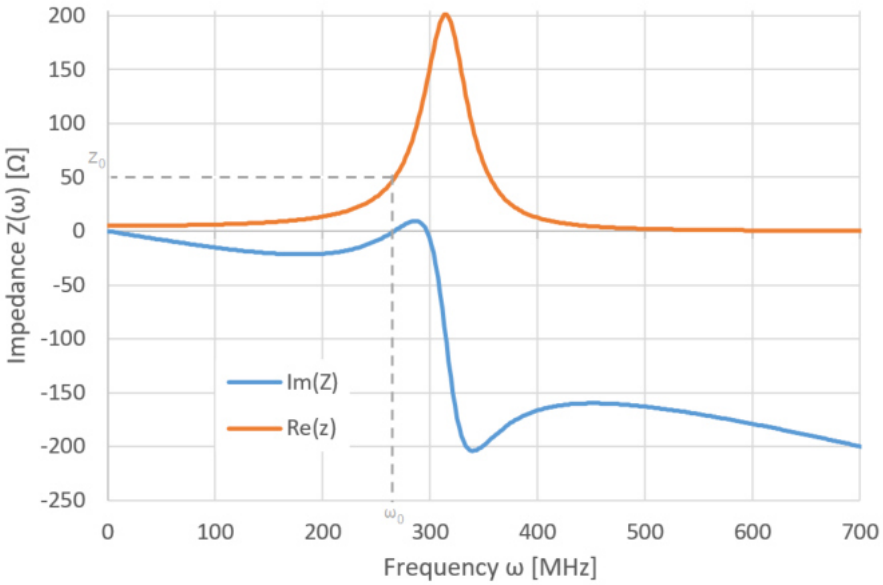

Figure 2.6: Chart of the real and imaginary part of the impedance over the frequency for a matched parallel resonant circuit.

the original resonance frequency. The RF chokes are used to block the high frequency from entering the DC-circuit, while the matching capacitors are also used to block the DC current flowing on the receive cable.

2.2.6 Decoupling

In case of using more than one coil (i.e an array of coils), the interactions between the elements must be carefully balanced. When two coils are considered, it is found that the magnetic flux of one resonant circuit influences the other one and an induction voltage in the second coil is created, as shown in Fig. 2.7 (a). The mutual inductance M_{12} depends on the geometry, and in particular on the distance between the resonant circuits. The coupling coefficient k is defined as:

$$k = \frac{M_{12}}{\sqrt{L_1 L_2}},$$

with L_i being the inductance of coil i = 1, 2. If k is larger than the critical coupling

$$k_c = \frac{M_{12}}{\sqrt{Q_1 Q_2}},$$

where Q_i refers to the quality factors of the coils, the curve splits into two peaks, as shown in Fig. 2.7 (b). This unwanted peak splitting results in low sensitivity of the coil at the Larmor frequency, and can be reduced by geometrical decoupling and preamplifier decoupling, as described in the following.

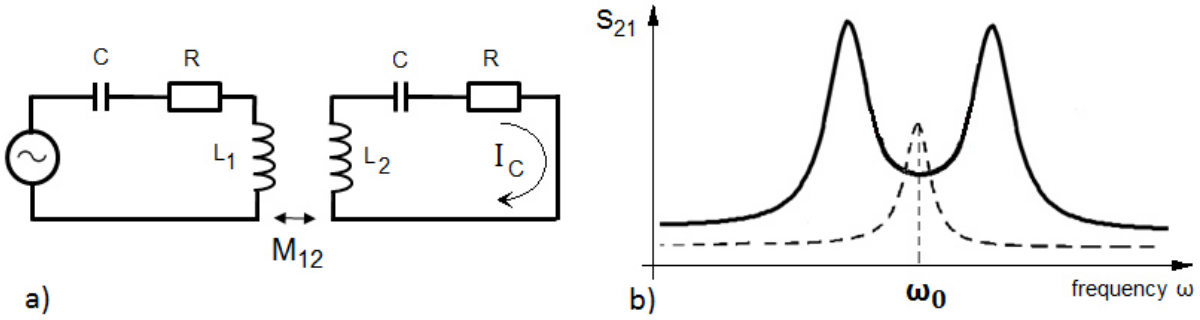

Figure 2.7: (a): Electrical circuit of the mutual coupling of two resonant circuits, the left circuit induces a current I_c into the right circuit. (b): The resonance curve for anon-coupled resonant circuit (dashed curve) and for over-coupling ($k > k_c$) a peak splitting occurs (solid curve).

Geometrical decoupling

Geometrical decoupling is used to reduce the coupling strength between two RF coils. The coupling coefficient k of two inductive coupled resonant circuits depends on the distance to each other. For a particular overlap distance (d_{opt}) $M_{12} \to 0$, which can be found experimentally. d_{opt} depends on the coil geometry; for two identical, circular loops with a diameter d_{coil} the optimal overlap distance

$$d_{opt} \approx 0.75 \cdot d_{coil} \tag{2.13}$$

was found by Roemer et al. [13]. To understand the geometrical decoupling, it is thought of a current, applied to one of the two loops. As shown in Fig. 2.8, a magnetic flux is generated in loop 1 due to I_1. If the second loop is nearby, the magnetic flux induces a current I_2 which generates magnetic flux in loop 2. For a perfect overlap the magnetic fluxes of the overlapping region and the non-overlapping region of loop 2 compensate each other fully. Since the flux density is much higher close to the wire, a small overlap is sufficient to compensate the fluxes.

Preamplifier decoupling

The inductive coupling arises due to a current flow in the coupled coil. The so-called preamplifier decoupling method reduces this current. Standard coils have a low impedance at the coil port (short). By transforming the input impedance Z_{in} of the preamplifier to high a impedance (open) of the coil port, the current flow on the coil can be suppressed. A sketch showing the relation can be seen in Fig. 2.9. For a well-decoupled standard loop coil $Z_{coil} \ll Z_{decoupl.}$.

2.2.7 Radiofrequency coil types

Several radiofrequency coils types are used and a short summary will be given, detailed information of various coils can be found in literature [12].
Usually a categorization between volume and surface coils is done: Volume coils surround the anatomy to be imaged completely. Since they are larger a more homogeneous Tx field is produced but a smaller sensitivity is obtained, whereas surface coils are smaller and closer to the

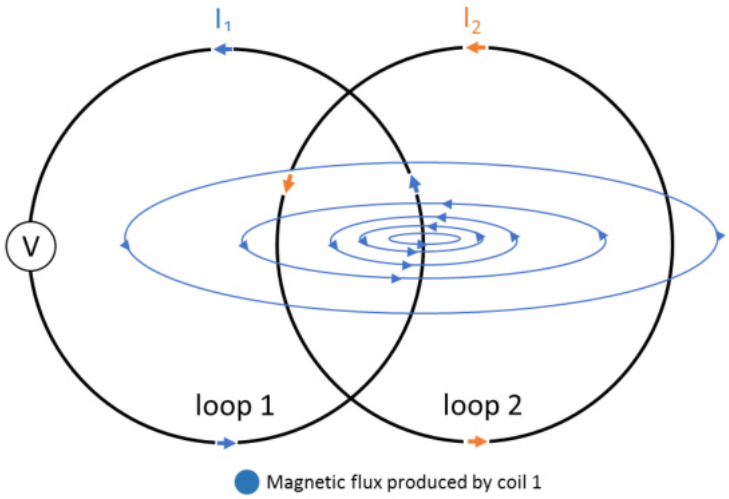

Figure 2.8: Sketch of the geometric decoupling of two circular loops with an applied current I_1 generating a magnetic flux. It induces a current I_2, which generates magnetic flux in loop 2. For an optimal overlap the fluxes compensate each other.

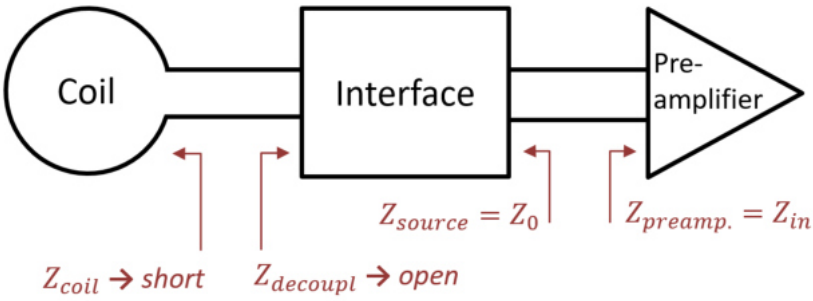

Figure 2.9: Sketch of the impedances for matching and preamplifier decoupling of a standard coil.

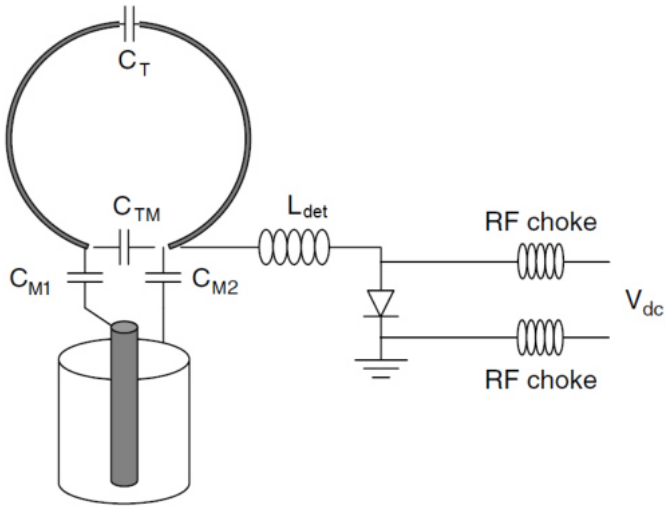

Figure 2.10: Standard RF receive coil on top with a tuning, matching and an active detuning network, reproduced from Vaughan et al. [12].

ROI. They have a higher sensitivity near the surface, but limited field of view.

Coil arrays

Most receive coils are built as arrays, i.e. they are consisting of several coils. Generally, there are advantages using an array of smaller coils positioned near to the ROI than using one large coil for the whole sample. If the coils are located near the region of interest only noise is detected from this region instead of the whole sample. The coils act as a spatial filter; less noise is added. Also, following Biot-Savarts's law, the magnetic field produced by a conductive loop with current I is the bigger, the smaller the loop is. By the principle of reciprocity, this means that in a smaller loop higher current is induced by a given source. These two effects result in a larger sensitivity. Additionally, parallel imaging techniques [3],[5], [4] can be used with an array of coils. These methods accelerate the acquisition of imaging data by acquiring a reduced amount of data compared to the fully sampled data. The image is then reconstructed from the undersampled data.

2.2.7.1 Standard coil design

Conventional receive-only coils consist of at least an inductor and a capacitor parallel to each other obtain a parallel resonant circuit as described earlier. The inductor is formed by the copper wire and the capacitor is positioned in between. This soldered arrangement forms a rigid structure. A sketch of a standard receive-only RF coil can be seen in Fig. 2.10. It shows the coil on top, connected to the tuning capacitor; then the matching, realized by two capacitors follows. The matching capacitors are connected to the receive coaxial cable which transmits the received MR signal.

2.2.7.2 Transmission line resonators

Other surface coil designs such as transmission line resonators (TLR) were invented [14] and further developed [15], [16]. In contrast to conventional coils TLRs have their capacitance distributed along the transmission line. Therefore, the arrangement is self-resonant and does not require soldered components, which allows more flexibility. A basic TLR with a parallel plate transmission line is shown in Fig. 2.11, both conductors are separated by a substrate and have one gap. The shape of the conductors forms the inductance and the capacitance is developed along the conductors by the distance between the conductors and the dielectric.

Recently, a TLR design with coaxial conductors was studied by Zhang et al. [6]. The coils were made of coaxial cables with one gap of the outer shield conductor (outer gap) and opposite to it the coil port was located with another gap of the inner conductor (inner gap). A sketch of this one-gap coaxial coil (CC) can be seen in Fig. 2.12.

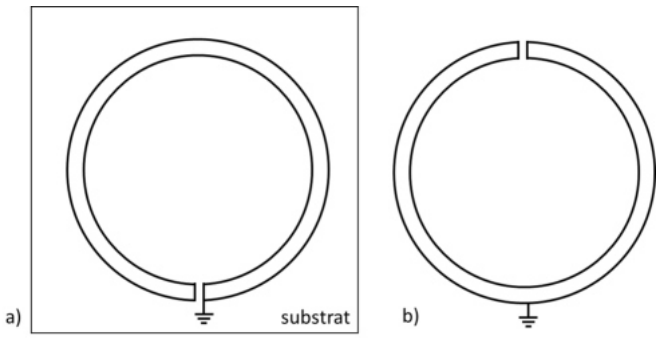

Figure 2.11: Front side (a) and backside (b) of a transmission line resonator. The lower conductor is shown detached from the substrate for more clarity.

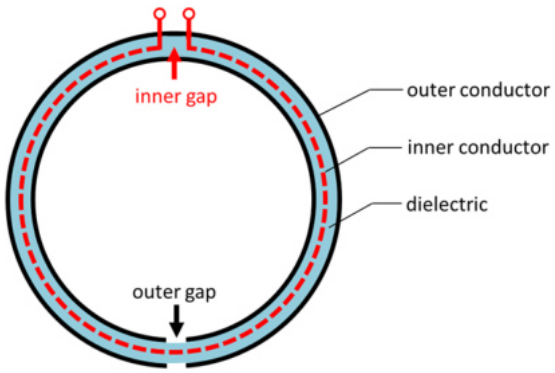

Figure 2.12: Sketch of a coaxial coil with inner and outer gap and the coil port.

Current distribution

According to Zhang et al., the current density of the inner conductor increases roughly linearly from the inner gap to a maximum at the position where the the outer gap is located. The current

then decreases symmetrically to the other side of the inner gap. This current is mirrored by an opposing current on the inner surface of the outer conductor. Due to skin depth effects the current flows through the outer gap from the inner to the outer surface. The current then travels uniformly along the outer surface of the outer conductor.

Resonance frequency restriction

Similar to parallel-plate TLRs, the inductance of the resonant circuit is formed by the circular arrangement of the coaxial cable while the capacitance is distributed between the inner and outer conductor in the dielectric with a relative permittivity ϵ_r.
The resonance frequency of the one-gap coaxial coil as described by Zhang et al. is restricted: Since there are no lumped components inside the coaxial coil its ω_0 is obtained by the characteristics of the used coaxial cable and the diameter of the coil. The cable is defined by the relative permittivity of the dielectric and the radii of the inner conductor and the outer tubular shield. Thus, if a particular coaxial cable is used and a particular resonance frequency is desired, the coil diameter is fixed.

2.2.7.3 Comparison of standard coils and coaxial coils

Several interesting differences between conventional loop coils and coaxial coils exist, which will be described in this section:

High impedance and low impedance coil

Standard loop coils have a low impedance at the coil port, thus a high impedance is required to suppress currents for best decoupling, whereas coaxial coils have a high impedance at the coil port and a low impedance is needed for current suppression. As stated by Zhang [6] with a "reverse preamplifier decoupling" the suppression can be obtained; the impedance at the port has to be "significantly lower than the intrinsic impedance" of the coaxial coil.

Detuning

The detuning of conventional coils is fulfilled by a second resonant circuit which can be switched during transmission. With this method the resonance frequency is shifted away from the Larmor frequency. In contrast to the copper coils, coaxial coils can be detuned by shorting the inner and outer conductor.

Ultra flexibility

There are no soldering joints except for the coil port which makes the whole resonant circuit much more flexible compared to conventional loop coils. To demonstrate the flexibility of this arrangement, a picture of the CC unbent and bent can be seen in Fig. 2.13.

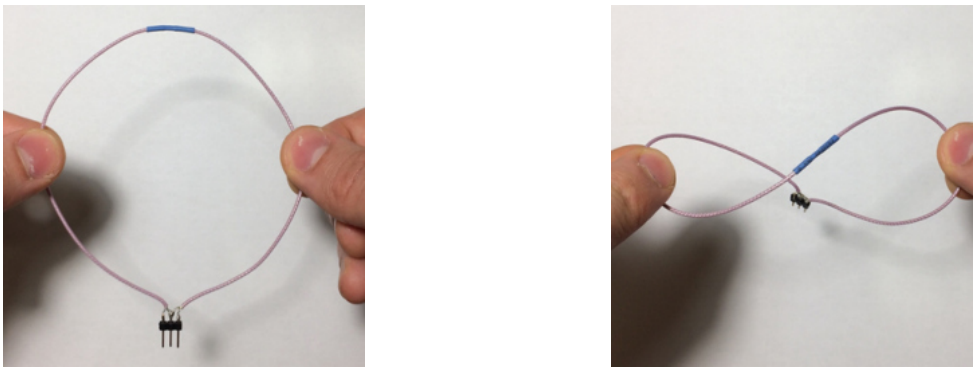

(a) (b)

Figure 2.13: One coaxial coil unbent (a) and bent (b) to demonstrate the flexibility of this resonant circuit. The outer gap is located l.h.s at the top (covered by a heat shrink tube) and the coil port, which also forms the inner gap, is located at the bottom.

Chapter 3

Methods

The aim of this thesis is a flexible three-channel receive-only coil array for a 3 Tesla whole-body MR scanner (Magnetom Prisma-Fit 3T, Siemens AG, Erlangen, Germany). The array consists of three coaxial coils, each with one interface to connect the coil to the scanner.
The measurement techniques is outlined in Sec. 3.1. In Sec. 3.2 the development of a single-channel CC is described, including an investigation of the properties of coaxial coils, the interfacing and the performance testing. The single-channel interfaces were tested on a phantom and compared to a standard loop coil of the same size. In Sec. 3.3 the implementation of an array of three coaxial coils with three interfaces is described, containing the layout of the three coils within the array, inter-element decoupling, as well as the implementation on a textile substrate. MR measurements of the final 3-channel coaxial coil array are performed on a phantom and two fruits.

3.1 Measurement techniques and materials

3.1.1 Vector network analyzer

The vector network analyzer (VNA) is an instrument to measure the parameters of an electrical network. It provides either the reflection or the transmission of electrical wave signals by measuring the magnitude and phase. In this work a Agilent Technologies E5071C network analyzer with the Configurable Multiport Test Set E5092A was used.

Scattering parameters

The frequency dependent scattering parameters (S-parameters) are used to describe the relation between input and output terminals of the VNA. A detailed description of single- and multiport networks can be studied [17]. Basically, as shown in Fig. 3.1 (a,b) the port-indexed current flows into the VNA and the voltage is recorded. Using both, the current i_n and the voltage u_n the incident and reflected normalized power waves a_n and b_n can be defined,

$$a_n = \frac{1}{2\sqrt{Z_0}}\big(u_n + Z_0 i_n\big) \quad \text{and} \quad b_n = \frac{1}{2\sqrt{Z_0}}\big(u_n - Z_0 i_n\big). \tag{3.1}$$

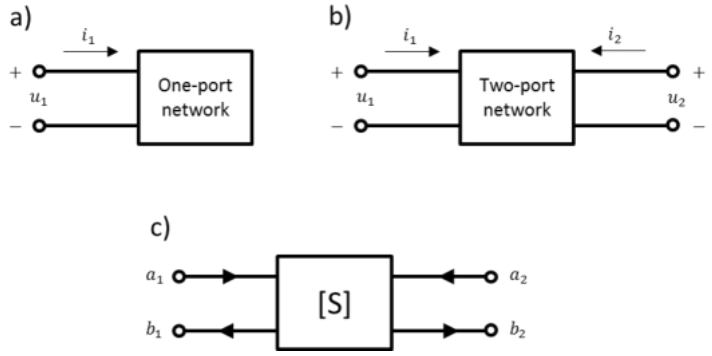

Figure 3.1: Sketch for single port network (a) and double port network (b) with the port-indexed currents and voltages for the explanation of the S-parameters (c).

The index n refers the port number and Z_0 describes the characteristic impedance of the connecting lines of input and output of the network. For a two-port network the S-parameters can be defined using

$$\begin{pmatrix} b_1 \\ b_2 \end{pmatrix} = \begin{pmatrix} S_{11} & S_{12} \\ S_{21} & S_{22} \end{pmatrix} \begin{pmatrix} a_1 \\ a_2 \end{pmatrix}, \quad \text{with} \quad S_{11} = \left.\frac{b_1}{a_1}\right|_{a_2=0}, \quad S_{21} = \left.\frac{b_2}{a_1}\right|_{a_2=0}, \quad \text{etc.}$$

Commonly the logarithm of the magnitude of the S-parameters is expressed as a loss (-) or a gain (+) in dB,

$$S_{ij[dB]} = -10 \log \left|S_{ij}\right|^2 = -20 \log \left|S_{ij}\right|. \tag{3.2}$$

Mixed mode measurement

All of the devices signals described above are referenced to a common ground potential (a so-called unbalanced device). In contrast, a balanced device is composed of two identical halves i.e. any relative amplitude and phase relation can be used. A balanced device can be decomposed into a differential (D) and a common mode (C) component.
Mathematically, there are only a few differences between single-ended S-parameters and the mixed-mode S-parameters. In fact, an easy transition between them exists, for instance

$$S_{DD11} = \frac{1}{2}\left(S_{11} - S_{12} - S_{21} + S_{22}\right),$$

where the name convention for the parameters follows an easy rule: The first and second subscript stand for the mode response and the mode stimulus (differential or common mode), while the numbers of the subscript refer to the port number.

Smith chart

A graphical method to investigate the complex impedance of the device under test (DUT) is the Smith chart. In this thesis it is used to assist in solving matching circuits and problems with transmission lines. An explanation of the real and imaginary axis of the normalized impedance

z as well as particular points of z are shown in Fig. 3.2.

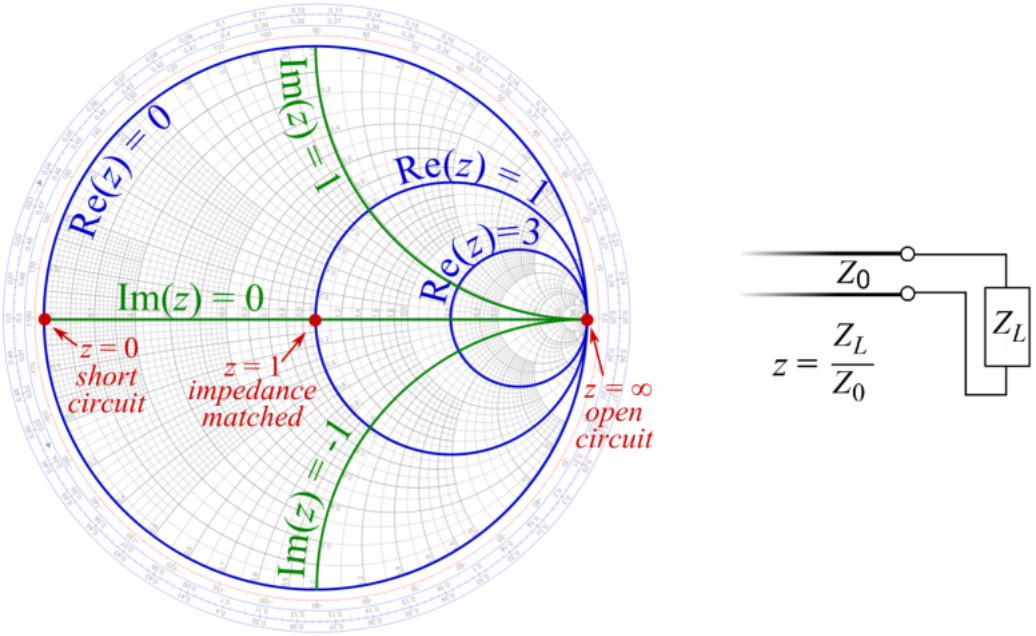

Figure 3.2: The Smith chart (l.h.s.) and the normalized impedance z, reproduced from the webside wikipedia.org [18].

3.1.2 Impedance calculation software

In this work, an open-access software called Pasan [19], is used to solve impedance matching problems. The software calculates the impedance Z_{in} either for one particular frequency ("calculate chart") or a frequency range ("scan"). Two screenshots of the program interface with some lumped components can be seen in Fig. 3.3 and Fig. 3.4. The electrical circuit with some components is shown twice, for a particular frequency (123 MHz) and for a frequency range (100 MHz to 140 MHz). The values can be set in the preferences of the program. Up to five components such as inductors, capacitors, resistors, transmission line, etc. can placed in the "diagram" at the top, r.h.s. of the program. The values of the components can either be changed by typing a particular value or clicking directly inside the Smith chart. A transmission line can be added to obtain a phase shift. Either the length of the transmission line or the phase in degree can be used, also the characteristic impedance and other parameters can be specified. The origin of the phase starts at the left side (short) the open is located at 90° clockwise or −90° counter clockwise.

3.1.3 Q-factor measurement

The Q-factor at a given resonance frequency can be easily obtained with a double-loop probe and the network analyzer. Q is obtained at the resonance frequency, as shown in Fig. 3.5. For

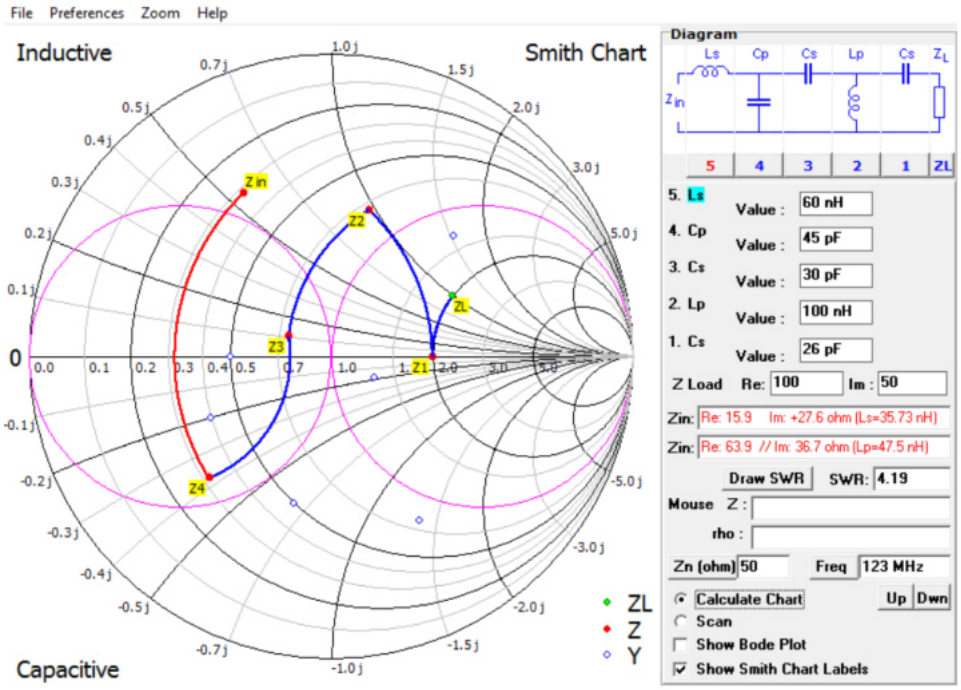

Figure 3.3: Program interface of the software Pasan with some lumped components for a particular frequency.

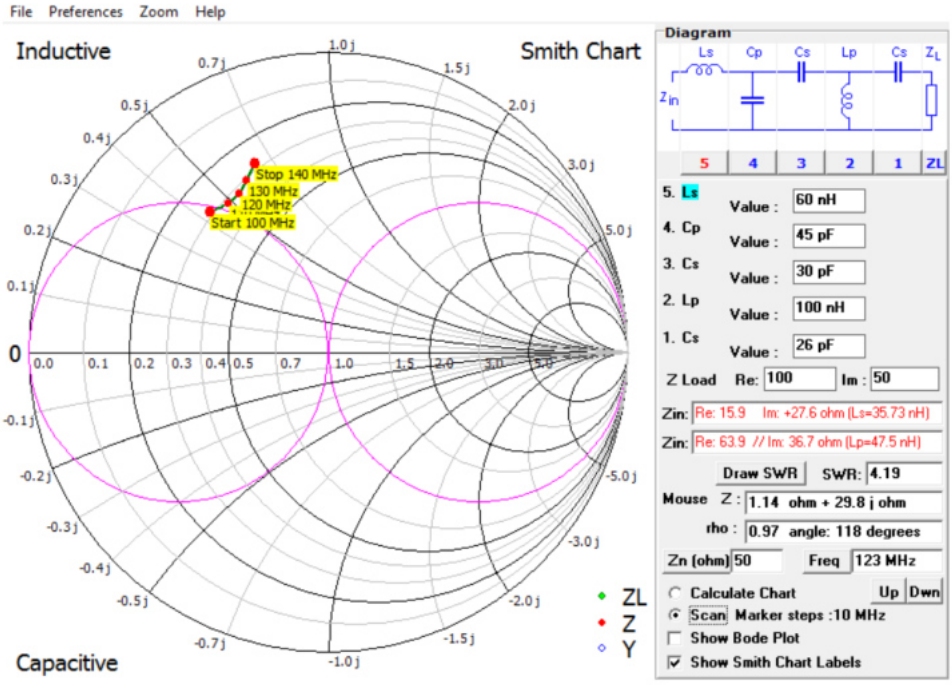

Figure 3.4: Interface of Pasan with some lumped components for a frequency range.

the S_{21} measurement the Q-factor is obtained by

$$Q = \frac{\omega_0}{\Delta\omega_0},$$

where $\Delta\omega_0$ is the bandwidth of the response curve at - 3dB. This can be automatically evaluated by the network analyzer.

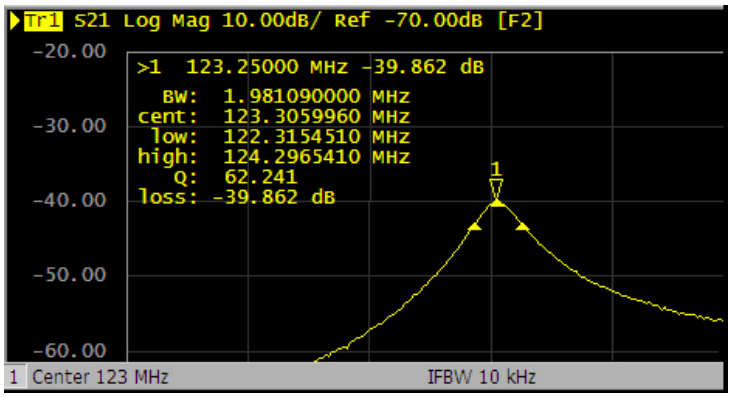

Figure 3.5: Q-factor obtained with the network analyzer using a double-loop probe.

3.1.4 Double-loop probe

One important instrument used to investigate the resonance frequency of an electrical resonator is the double-loop probe [20]. Basically, it consists of two geometrically decoupled loops which are connected to a two-port network analyzer. If a coil is approached to the device, coupling can be measured as follows: an electrical signal is sent into one loop of the double-loop probe and couples to the probe resonator. The resonator couples to the second loop and thereby transmits a signal to the VNA, i.e. the transmission parameter S_{21} can be obtained. Without any resonator nearby, it yields $S_{21} < -80$ dB for well-decoupled loops.

3.1.5 Components

3.1.5.1 Thin coaxial cable

Since the CC should be flexible and light-weight, thin coaxial cables from the cable assembly of an unused Siemens receive MR-plug were chosen. For the coaxial cables no data sheet was available, however the dimensions were measured using calipers. As shown in Fig. 3.6, the cables have following dimensions: The inner conductor has a diameter $d_i = 0.2$ mm and is coated with the dielectric with an outer diameter $d_d = 0.58$ mm. The dielectric is surrounded by a tubular conducting shield with a diameter $d_o = 0.9$ mm. The conducting shield is protected by an insulating outer jacket with $d_j = 1.16$ mm. This cables are used for all coaxial coils, if not additionally specified. From phase measurements, the velocity factor of the cable was

determined to be $VF \approx 74\%$. The factor corresponds with

$$VF = \frac{1}{\sqrt{\epsilon_r \mu_r}} \approx \frac{1}{\sqrt{\epsilon_r}} \quad \text{to} \quad \epsilon_r \approx \frac{1}{VF^2} \approx 1.8.$$

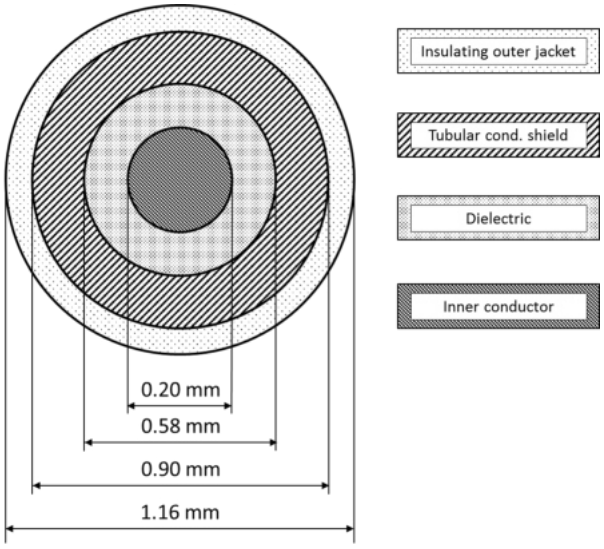

Figure 3.6: Cross section with the related dimensions of the thin coaxial cable from the Siemens MR plug.

Thick coaxial cable

Thick coaxial cables (K_02252_D, Huber + Suhner, Herisau, Switzerland) were also used. The dimensions are: centre conductor diameter 0.54 mm, the dielectric diameter is 1.55 mm, the outer conductor has a diameter of 2.5 mm and the diameter of the jacket is 3 mm. The impedance of the cable is 50 Ω and the velocity factor of signal propagation is $VF = 69\%$.

Self-made inductors

The inductors used for the modular interface were self-made. They were easily built by winding a copper wire to a solenoid. The inductance was determined by the wire diameter, the solenoid diameter and the number of turns. Approximations for the inductance of a solenoid can be found [21]. Basically, the inductance increases with decreasing wire diameter. It decreases with increasing solenoid diameter and increasing number of turns.
A wire diameter of 0.75 mm was used for all inductors. Drill bits with different diameters were used for winding the solenoids. To measure the inductance, the inductors were connected to a capacitor with known capacitance, forming an L-C resonant circuit. The resonance frequency obtained with a double-loop probe in combination with the known capacitance was used to calculate an approximation of the inductance of the solenoid (Eq. 2.9). Different capacitors

were used to calculate the mean value of the inductance. This method can only be used as an approximation of the real value of the inductor.

Square air core inductors

Inductors (1515SQ, 2222SQ, 2929SQ, Coilcraft Inc., Illinois, USA) were used for the compact interface which is described after the modular interface. This so-called square air core inductors are smaller than the self-wound inductors and have a well defined inductance with a tolerance of 5%.

Preamplifier

Low input impedance and low noise figure preamplifiers were used (MPA123R20, HI-Q.A. Inc, Ontario, Canada). The real part of the impedance is fixed $Re(Z_{preamp}) \approx 1.5\,\Omega$ and the imaginary part can be adjusted with a small screw: $\mathrm{Im}(Z_{preamp})$: $3\,\Omega$ to $32\,\Omega$. The optimal noise matching of the preamplifiers is at 50 Ω, meaning that at this impedance the signal is amplified with the lowest noise rate.

Cable traps

Shield currents (or common mode currents) are currents running on the outer shield of coaxial cables. One cause of shield currents in MRI is the electromotive force induced in the shield of the cable of the receive-only coil by the transmit coil. They can damage the receive coil and cause serious patient burns. Therefore, such currents must be reduced for the safety of the patient and the coil. For the MR measurements performed for this thesis floating traps [22] on the connecting cables from coil to scanner were used to reduce the common mode currents.
The traps consist of a hollow cylinder, made of Teflon and split in two halves. Both forms are coated on the inside and the outside lateral surface area with copper. Additionally, one end of both cylinder-halves is plated with copper to shorten inner and outer cylinder, while at the other ends a capacitor is placed, respectively. This arrangement creates a resonant circuit with a frequency according to its capacitance and inductance. The inductance is obtained by the coated copper and the capacity is developed due to the dielectric (Teflon) of the cylinder as well as the capacitors, which are used to tune the trap to the Larmor frequency.

Phantom

A torso phantom, filled with tissue-equivalent gel ($\sigma = 0.60$ S/m, $\epsilon = 62$) was used for bench test and MR measurements. Additionally, the flat bottom of the phantom was used to measure the coupling of two coil elements.

Textile

Three different textiles for the implementation of the array from the company Stoff Palette, Donaueschingen, Germany, were used. An ultra-thin and flexible tissue (TG1111), a red foam

padding (TG1019250), and a water-proof synthetic leather (TG1013001), which is water-proof and can be cleaned and disinfected easily, were used..

3.2 Single-channel coaxial coil development

The static magnetic field B_0 of the scanner is ≈ 2.89 T, therefore a Larmor frequency $f_0 \approx 123$ MHz, according to Eq. 2.3, is obtained. Since the resonance frequency of the single-channel receive coil depends mostly on the coaxial coil, it is studied first.

3.2.1 Properties of the coaxial coil

3.2.1.1 Coil shape

The resonance frequency of the coil depends on the inductance which changes with the shape of the coil. To study this behaviour, an investigation of the dependence between the coil shape and the resonance frequency was performed.
A measurement of a circular and an elliptical coil with a double-loop probe connected to the VNA was executed. CCs with one, two and three gaps and an arbitrary diameter of approximately 90 mm were used. The experimental setup of the S_{21} measurement can be seen in Fig. 3.7. The total distance between the double-loop probe and the investigated CC was approximately 40 mm, whereas the plastic plates had a total thickness of around 8 mm. All measurements were performed twice, unloaded and loaded, whereas the loaded measurements were performed with a box-shaped phantom filled with a human tissue equivalent gel.

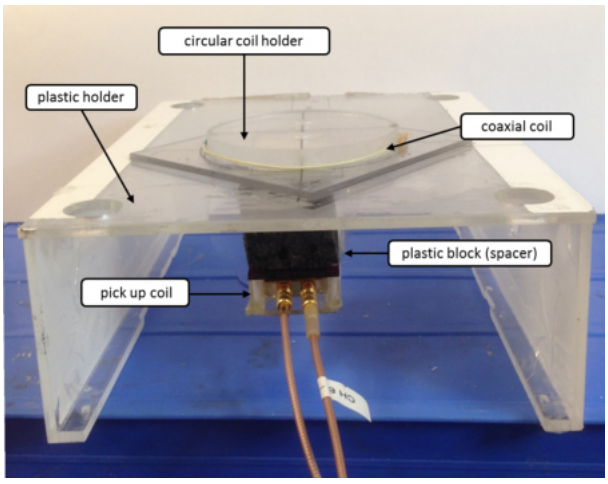

Figure 3.7: Picture of the resonance frequency measurement setup for coaxial coils with a circular and elliptic shape.

Two coil holders were built to hold the flexible coil ether in a circular or an elliptic shape. The ellipse had the same circumference as the circle and a semi-minor axis of $\frac{d_{coil}}{4}$. Thereby, for the ellipse parameters one obtains: semi-major axis $\approx$ 59 mm, semi-minor axis $\approx$ 22 mm

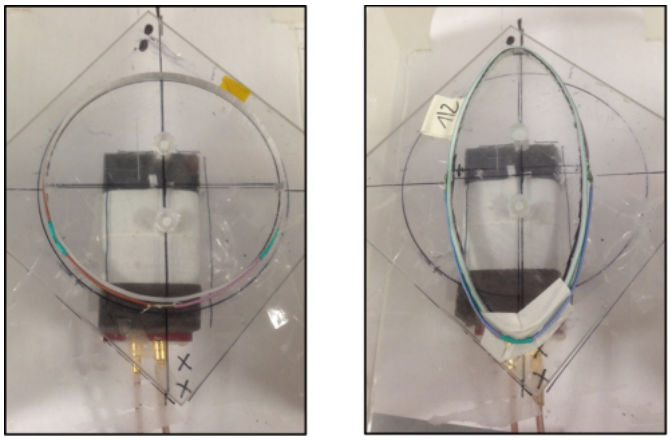

Figure 3.8: Circular (l.h.s) and elliptic (r.h.s) experimental setup for measuring the resonance frequency.

and linear eccentricity ≈ 54 mm. Both coil holders can be seen in Fig. 3.8. The measurement was performed for one, two and three gaps, without connecting it to an interface.

3.2.1.2 The multi-gap coaxial coil

The previously mentioned restriction in the choice of the coil diameter can be overcome by changing the number of gaps n_g. The number of gaps changes the current distribution along the coil and with it the resonance frequency is changed, which is described later in more detail. Each coaxial coil was built with a pairwise number of gaps. For example, a two-gap coil refers to a coil with two inner and two outer gaps. The multiple gaps are positioned alternately (inner - outer gap) and equidistantly along the coil as shown in Fig. 3.9.

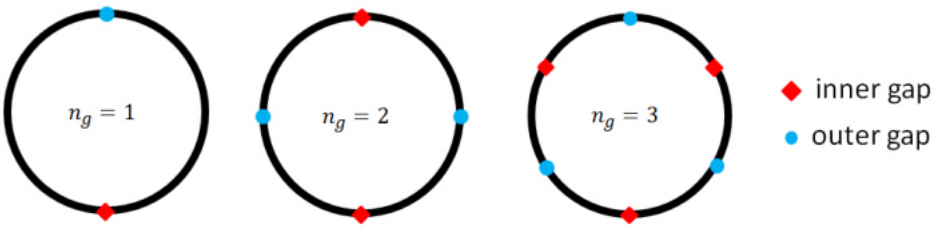

Figure 3.9: Coaxial coils with different number of gaps n_g. From left to right one-gap, two-gap and three-gap coaxial coil.

Resonance frequency

A model to describe the resonance frequency of the coaxial coil with multiple gaps was investigated. For the one-gap CC the dependence of ω_0 has already been described by Zhang et al., and is summarized:

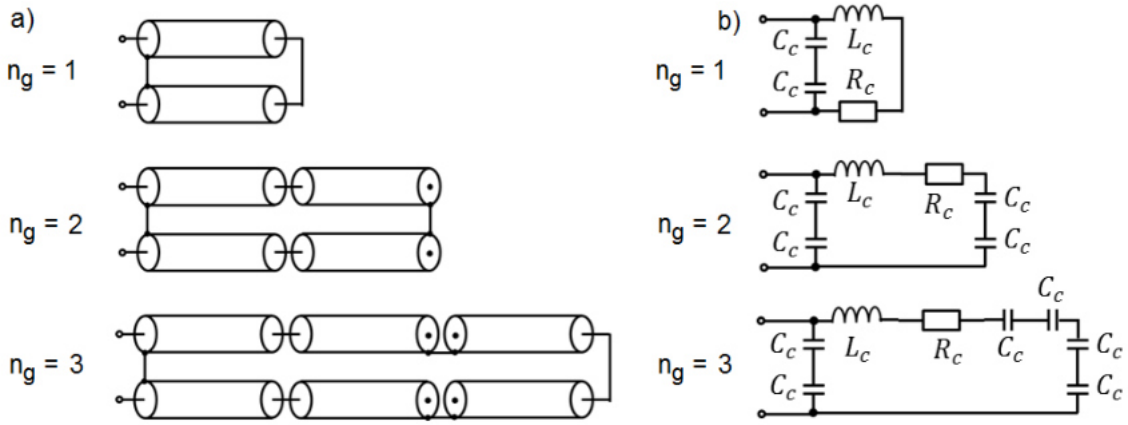

Figure 3.10: A sketch of coaxial coils consisting of coaxial stubs (a) and their equivalent circuits (b) for 1, 2 and 3 gaps.

The one-gap CC can be thought of as "two open-ended coaxial stubs of length l connected in series by the centre conductor". Each arm has an impedance

$$Z_{coax} = -iZ_0 \cot\left(\frac{\omega_0 l\sqrt{\epsilon_r}}{c}\right), \tag{3.3}$$

with $Z_0 = 50\ \Omega$ being the characteristic impedance of the coaxial cable. Zhang et al. approximated the inductive impedance of the coaxial coil by the self inductance of a conventional loop of similar size

$$Z_L = i\omega_0\mu_0\frac{d_{coil}}{2}\left(ln(\frac{8d_{coil}}{d_1}) - 2\right), \tag{3.4}$$

where μ_0 is the vacuum permeability, d_{coil} and d_1 refer to the coil diameter and the diameter of the outer conductor. As stated by Zhang et al., the equivalent circuit is a parallel resonant circuit. A sketch of the one-gap CC can be seen on top of Fig. 3.10 (a). It shows the two coaxial stubs, connected on the right hand side by the inner conductors (outer gap) and connected by the outer conductor on the port on the left hand side (inner gap). The stated parallel resonator of the one-gap CC is shown on top of 3.10 (b). The total impedance Z_{n_g1} can be added to

$$\frac{1}{Z_{n_g=1}} = \frac{1}{2Z_{coax}} + \frac{1}{Z_L + R_C}, \tag{3.5}$$

where R_C describes the coil losses and is added to Z_L, contrarily to Zhang's description.

As mentioned, the model presented by Zhang et al. describes the one-gap CC. A description of how it can be extended for multi-gap coaxial coils is given in the following:
The two-gap coaxial coil can be thought of 4 coaxial stubs, which are connected as shown. Z_L, R_C and the two capacitors in parallel C_c stay the same while two additional capacitors C_c in series are added. For $n_g = 3$ another two coaxial stubs and thereby two capacitors in the equivalent circuit are added. The total impedances for two gaps ($Z_{n_g=2}$) and three gaps ($Z_{n_g=3}$)

can be calculated,

$$\frac{1}{Z_{n_g=2}} = \frac{1}{2Z_{coax}} + \frac{1}{Z_L + R_C + 2Z_{coax}} \quad \text{and} \quad \frac{1}{Z_{n_g=3}} = \frac{1}{2Z_{coax}} + \frac{1}{Z_L + R_C + 2 \cdot 2Z_{coax}}.$$

Thus, a generalisation to describe the relation between the impedance and the resonance frequency for a number of gaps n_g can be found:

$$\frac{1}{Z_{n_g}} = \frac{1}{2Z_{coax}} + \frac{1}{Z_L + R_C + 2(n_g - 1)Z_{coax}}. \tag{3.6}$$

The resonance condition ($Im(Z_{n_g}) = X_{n_g} = 0$) of the multi-gap coaxial coil can be found:

$$X_{n_g} = 2n_g X_{coax} + X_L = 0. \tag{3.7}$$

Resonance frequency of multi-gap coaxial coils

To study the relation between n_g and f_0, circular coaxial coils with one, two and three gaps (shown in Fig. 3.9) with an arbitrary diameter $d \approx 90$ mm were built. The resonance frequency was obtained with an S_{21} measurement, as described above.
The one-gap coaxial coil was chosen for the 3-channel array implementation, since the resonance frequency for $d_{coil} \approx 90$ mm was close to the desired Larmor frequency for protons.

3.2.1.3 Coil diameter

By choosing the coaxial cable and deciding the coaxial coil to have one gap, the only parameter left to obtain the correct resonance frequency for protons is the coil diameter d_{coil}. Empirically it was found that for a desired Larmor frequency $f_0 \approx 123$ MHz the correct CC diameter is around 80 mm. The one-gap coaxial coils were built from coaxial cables with a total length l = 255 mm. Since the cable ends are partly overlapping when building an inner gap, the diameter reduces to around 80 mm. A picture of the one-gap coaxial coil is shown in Fig. 2.13 (a).

3.2.1.4 Practical implementation of gaps

To build an outer gap, the outer conductor of the coaxial cable is cut out for a gap width of around 4 mm. The insulating outer jacket and the tubular conducting shield are carefully removed. For additional protection a heat shrink tube was used to cover the gap.
To produce an inner gap, two coaxial cables are soldered together as follows: the isolation of the outer conductor is removed at the cable ends ($\approx 4mm$). Then the inner conductor is separated from the outer conductor. Since the tubular conducting shield consists of a netting of thin cables, it is necessary to carefully separate them from the dielectric with the inner conductor. Then the outer conductors are soldered together partly overlapping such that a gap size of around 4 mm is obtained.

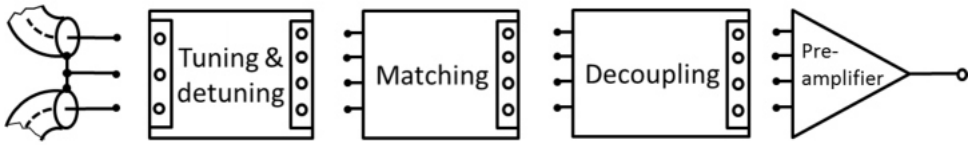

Figure 3.11: The modules of the interface, on the l.h.s. the one-gap coaxial coil, truncated.

3.2.2 Interfacing the coil to the scanner

To connect the coaxial coil to the NMR scanner an interface is necessary. As described in Sec. 2.2 this interfacing consists of an electrical network which can be divided into tuning and active detuning, matching, and preamplifier decoupling. The signal is then amplified using a low noise preamplifier.

First, a modular system of the interface was built to allow a separate investigation of its three parts: tuning and detuning, matching and decoupling. As shown in Fig. 3.11 each module is provided with pin connectors. The modules can be plugged as shown to add up to the total interface. The CC is provided with a 3-pin plug; the outer pin connectors are the ports of the coaxial coil and the inner connector is the ground. The tuning module is equipped with a 3-pin socket to plug the CC and a 4-pin socket to connect to the matching module. The two inner pins of this socket make one port and the two outer pins make the second port. A separate investigation of the CC connected to the tuning module is possible with a 4-pin plug. It can be connected to the VNA to measure the S_{11} parameter. Then the matching module follows, equipped with a 4-pin plug to connect to the tuning and a 4-pin socket to connect to the phase-shifter module. The phase shifter is also equipped with a 4-pin connector to connect to the preamplifier. A separate investigation of the matching or phase-shifting module is possible by using two 4-pin connectors and measuring the transmission, S_{21}. Additionally, a measurement of the coil, the tuning and matching is possible using S_{11} with or without the phase-shifting module. The preamplifier is equipped with a 4-pin plug on one the input side and on the output side a MCX socket to connect to the MR plug is located.

A sketch of the final modular electrical circuit can be seen in Fig. 3.12. From left to right it shows: The one-gap coaxial coil, followed by the tuning (the capacitor and inductance are subscripted with "T") and the active decoupling with PIN diodes. Then the matching and a phase shifter is shown as well as the preamplifier.

3.2.2.1 Tuning and detuning

To tune the coaxial coil to the right resonance frequency, the reactance X has to be set to zero as described in Eq. 2.10. The tuning and detuning module consists of lumped components, which are shown in Fig. 3.13 (a). The inductance L_{Teq} used for tuning was placed parallel to

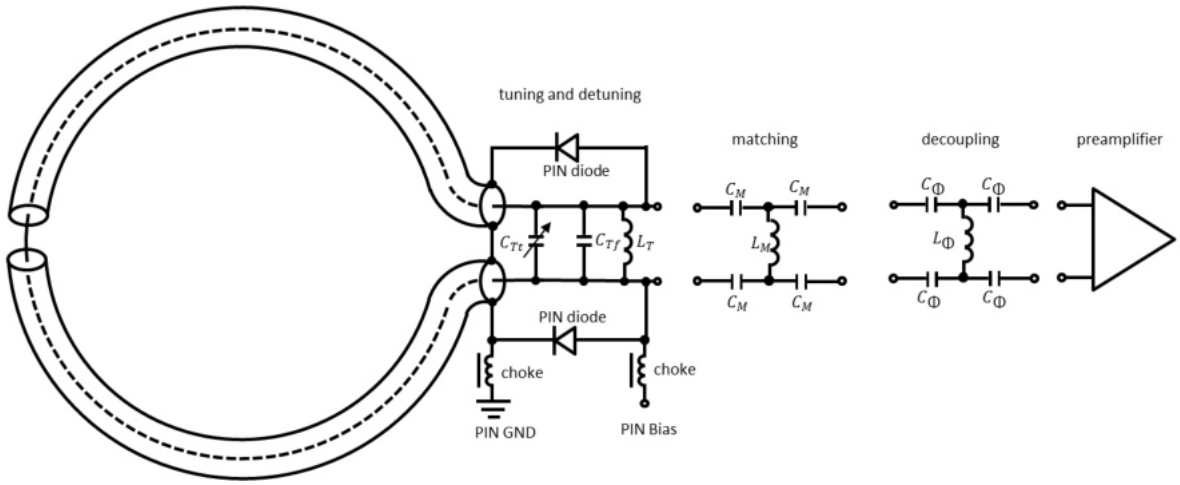

Figure 3.12: Sketch of the electrical circuit to connect a coaxial coil with the MR scanner. The one-gap CC is on the l.h.s, in the middle the electrical interface and the preamplifier on the r.h.s..

the ports, thus the DC signal used for detuning can reach both PIN diodes. Two chokes were placed at the DC port to block the RF signal. Two high-value capacitors C_B were placed in series at each port to block the DC signal for detuning. The outer conductors of the coaxial coil were connected at the coil ends (inner gap). By forward biasing the PIN diodes the inner and outer conductor were shorted via this connection at the inner gap. For more clarity it is referred to the detuning circuit with an applied DC, shown in Fig. 3.13 (b).

To tune the coil, experimentally an inductance $L_{Teq} \approx 500$ nH was found. The size of a

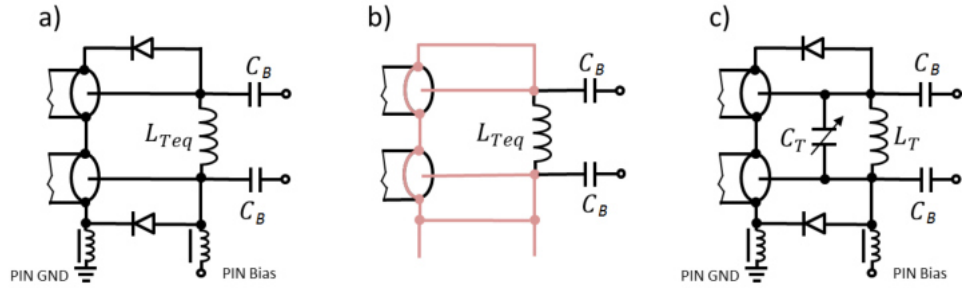

Figure 3.13: Basic tuning and detuning network (a) and the electric circuit with applied DC current (b). Changed tuning interface with smaller inductance L_T and parallel capacitor (c).

self-made air core solenoid with this value is large and a fine tuning to $X \to 0$ is only possible by pulling the turns of the solenoid apart or pushing them together. Thus, the inductor was changed to a "tunable inductance" by connecting a trimmer (i.e. an adjustable capacitor) in parallel to the inductor which can be seen in Fig 3.13 (c). Although this configuration connects the two ports for an RF signal via the tunable capacitor, the electrical behaviour stays the same. By looking at the tunable capacitor parallel to the inductance L_T as stand-alone circuit, one finds that it yields to an equivalent inductance L_{Teq}:

$$\frac{1}{Z_{Teq}} = \frac{1}{Z_L} + \frac{1}{Z_C} \quad \Leftrightarrow \quad \frac{1}{i\omega_0 L_{Teq}} = \frac{1}{i\omega_0 L_T} + i\omega_0 C_T, \tag{3.8}$$

where L_T refers to the new, smaller tuning inductor. With the equation above using the obtained $L_{Teq} \approx 500$ nH a combination of C_T and $L_T < L_{Teq}$ can be obtained. Additionally, as one can see, C_T and L_T form a parallel resonant circuit, creating an additional resonance depending on the values of the lumped components.
A chart showing the equivalent inductance $L_{Teq}(C_T)$ at the Larmor frequency for different smaller inductances L_T as described by Eq. 3.8 can be seen in Fig. 3.14. L_{Teq} is increasing with C_T to a singularity for a value of C_T fulfilling the resonance condition. The curves are very similar but shifted horizontally depending on L_T. $L_T = 100$ nH is chosen, thus $C_T \approx 13.4$ pF is obtained.

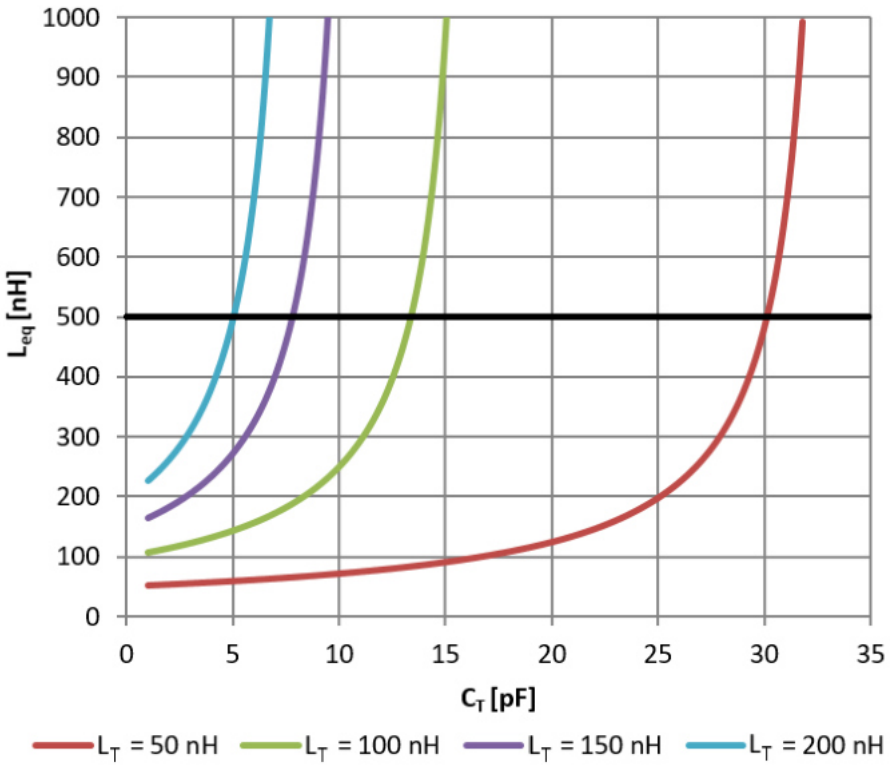

Figure 3.14: The inductance L_{Teq} over the tunable parallel capacitance C_T for different (smaller) inductances L_T. The desired inductance $L_{Teq} = 500$ nH is marked.

The capacitance was split into a fixed capacitor C_{Tf} and a tunable capacitor C_{Tt} in parallel to allow a fine tuning. The final electrical circuit of the tuning nodule can be seen in the final interface, Fig. 3.12. As one can see, there are no blocking capacitors C_B in series since this is achieved by the matching interface, which will be discussed in the next section.

A picture of the built modular tuning and detuning module can be seen in Fig. 3.15. The following lumped components, as corresponding to the picture, are shown:

1) Fixed tuning capacitor $C_{Tf} = 12$ pF.

2) Tuning inductor $L_T \approx 100$ nH.

3) Black 4-pin socket to connect to the matching module.

4) Adjustable tuning capacitor C_{Tt} : 2 to 6 pF.

5) Two chokes with $L_{choke} = 5.6$ μH to block the DC signal.

6) Two PIN diodes for detuning the coil when forward biased.

7) Black 3-pin socket to connect the coaxial coil to the tuning module.

8) DC cable.

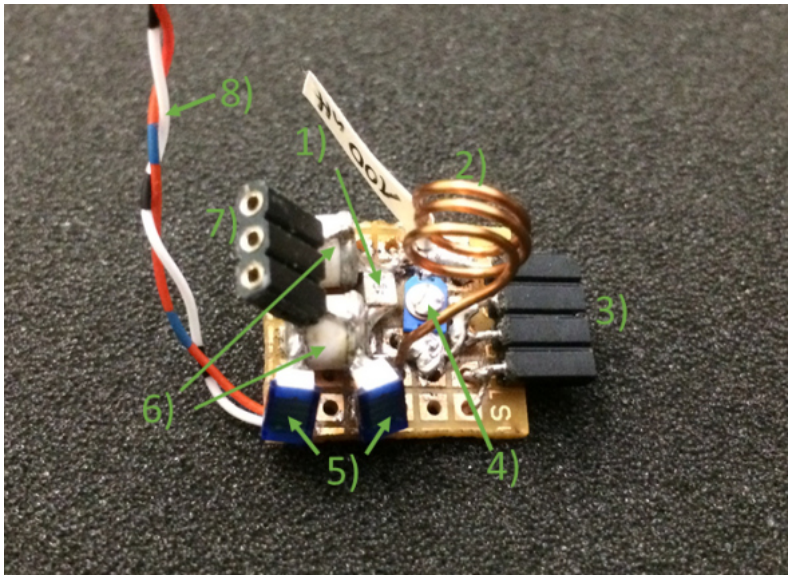

Figure 3.15: Picture of the final modular tuning and detuning module.

Additionally, the tuning was compared to the impedance matching software Pasan. The obtained Smith chart can be seen in Fig. 3.16, where the loaded impedance Z_{Load} refers to the coaxial coil, which was approximated with $Re(Z_{Load}) \approx 1.5$ $k\Omega$ and $Im(Z_{Load}) \approx 1$ $k\Omega$. It can be seen that for the parallel capacitor with a value of 17 pF the tuning was satisfied best, which is different to the calculated capacitance described above. The reason for the discrepancy probably comes from the not very accurate measurement of the inductance of the solenoid, which is discussed in detail later.

The S-parameter measurement of the tuning interface was performed on a torso phantom (3.1.5.1). The details of the S_{11} measurement with the vector network analyzer can be seen in Sec. 4.1.1.3.

3.2.2.2 Matching

After tuning the coil to zero reactance ($X \longrightarrow 0$), impedance matching to the standard impedance $Z_0 = 50\,\Omega$ was performed. The matching interface was produced as a separate

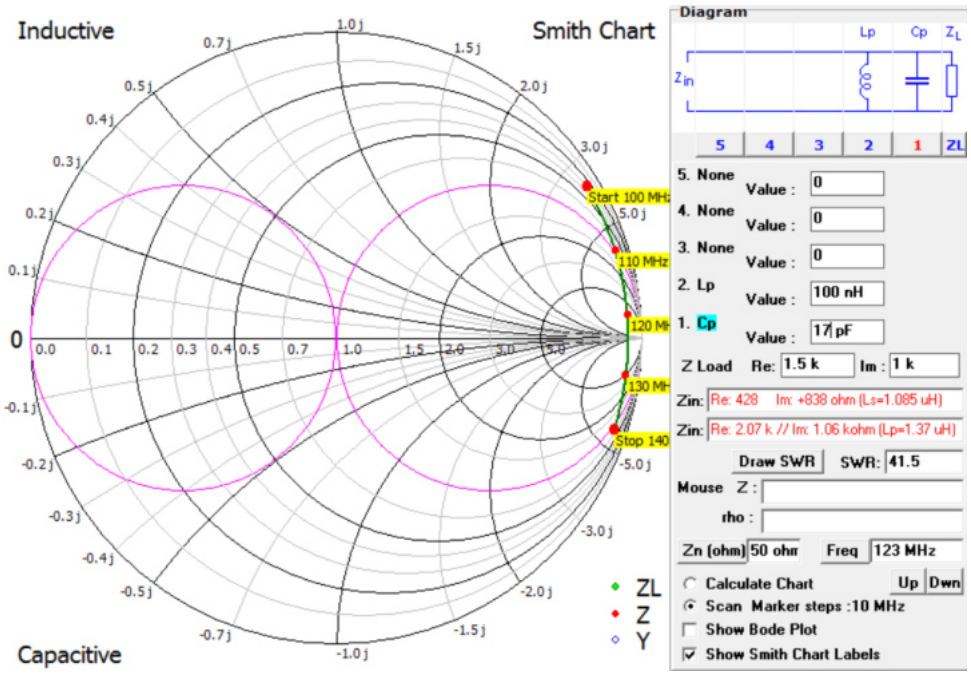

Figure 3.16: Smith chart of the electrical circuit of the tuning interface obtained with the software Pasan for a frequency range.

module and can be plugged to the tuning module with the coil. The large resistive impedance ($R > 500\,\Omega$) of the coil was transformed to Z_0 using a combination of two capacitors in series and in between one inductor parallel to the ports, as shown in Fig. 3.17.

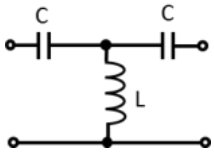

Figure 3.17: Basic electrical circuit to match the coil to the standard impedance $Z_0 = 50\,\Omega$.

The values of the lumped components for the matching module were obtained theoretically using Pasan, as shown in Fig. 3.18. The actual values are described below, while for the general behaviour the following was found: The matching circuit depended much more on Z_{load} than the tuning. For example, if the coil resistance was changed from $Re(Z_{load}) = 1.5\ k\Omega$ to $2\ k\Omega$ the matching inductance L_M had to be changed from 430 nH to 460 nH. The Smith chart of the matching circuit with a frequency range is shown in Fig. 3.19. One can see that the imaginary part of the obtained impedance depends strongly on the frequency of interest at Z_0.

Each matching capacitor was replaced by two capacitors of double the value in series, to obtain a symmetrical electrical circuit, as shown in the final interface. As already mentioned in the tuning and detuning section, the splitting also allowed to omit the two blocking capacitors C_B in the tuning module. A picture of the built matching module is shown in Fig. 3.20 with the

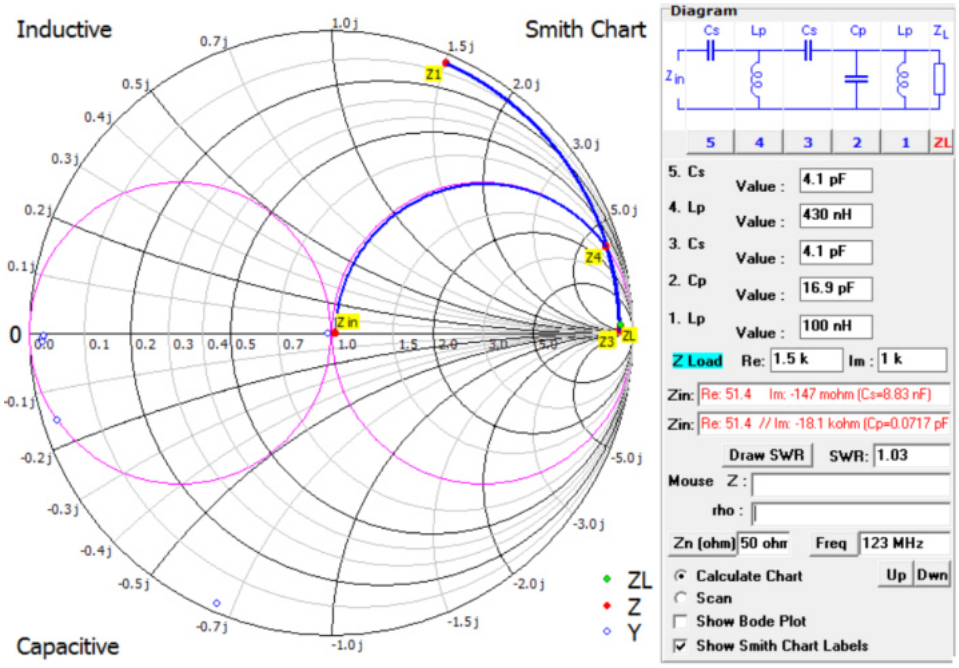

Figure 3.18: Matching of the coaxial coil for the desired resonance frequency of 123 MHz.

following components and their values:

1) Four matching capacitors $C_M = 8.2$ pF.
2) Black 4-pin socket to plug the decoupling module.
3) Large self-wound matching inductor $L_M \approx 500$ nH.
4) Black 4-pin connector to plug the tuning module.

The results of matching the built module interface is shown in Sec. 4.1.1.3.

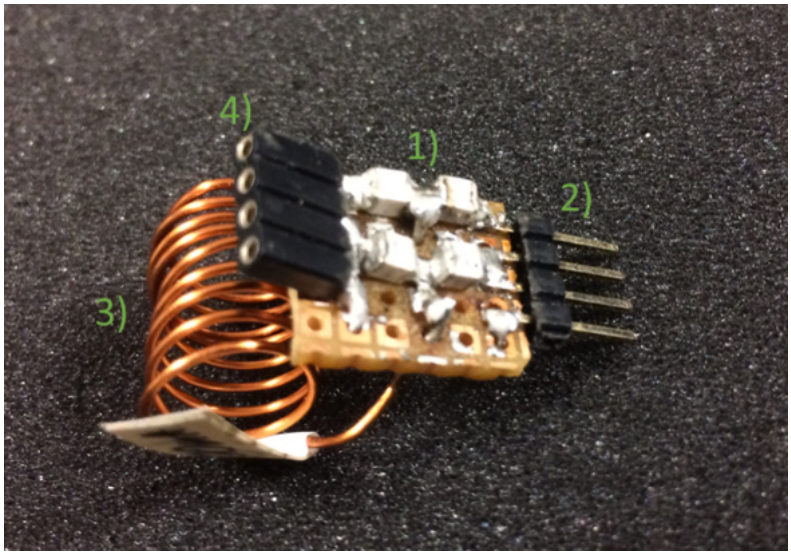

Figure 3.20: Final built matching module.

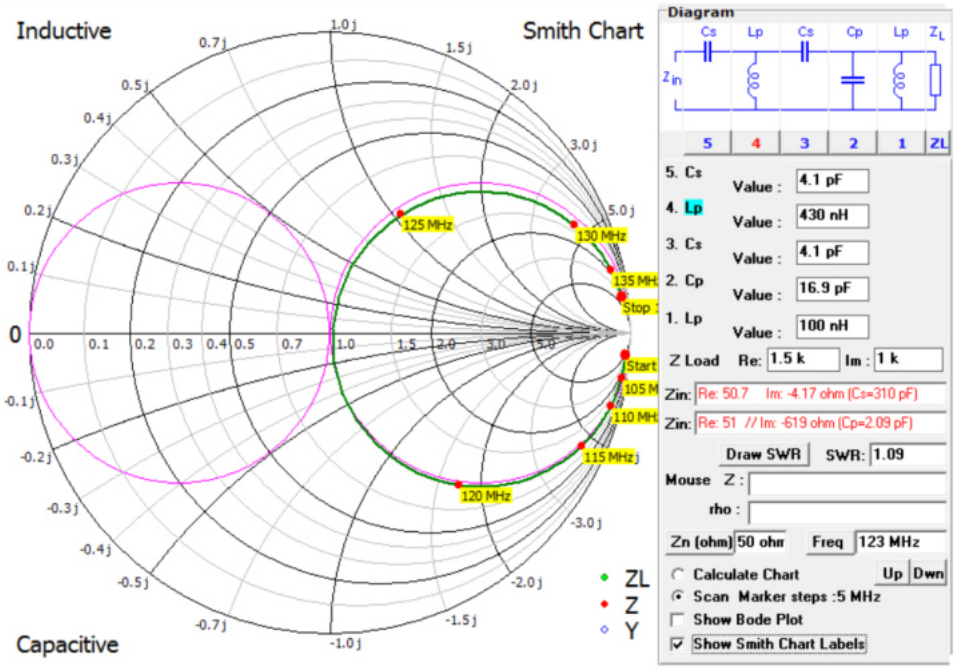

Figure 3.19: Matching of the coaxial coil, for a frequency range of 100 MHz to 140 MHz.

3.2.2.3 Decoupling

After tuning and matching the coil to f_0 and Z_0, the third module of the interface is the decoupling module. Together with tuning and matching it transforms the low input impedance of the preamplifier to a short at the coil port, having the same current-suppressing consequence as the active detuning circuit, thereby reducing the mutual coupling between coil elements.
Since the previous tuning and matching of the coil should not be influenced by the preamplifier decoupling module, a phase shifter can be used to fulfill the task without influencing the matching: In the Smith chart, a phase shifting is represented by a rotation around the matched impedance in the middle of the Smith chart. Since the impedance of the coil was already matched to $Re(Z_{coil}) = 50\,\Omega$ and $Im(Z_{coil}) = 0$ an arbitrary rotation e.g. with a transmission line did not change the impedance.
A phase shift can be obtained either with a transmission line (e.g. a coaxial cable) or lumped components. Especially for an array of coils the additional cables would be disturbing. Thus, a solution with lumped components is preferred. Each of the two high and two low pass filters shown in Fig. 3.21 can be used as a phase shifter. Since each filter consists of two identical lumped components and the inductors are self-built by winding copper wire to a solenoid, it is preferred to use a configuration consisting of only one inductance to avoid inductance variations. The electrical circuit (a), a so-called high-pass tee is chosen.

The values of the lumped components can be calculated using

$$L_1 = \frac{Z}{\omega_0 sin(\phi)} \quad \text{and} \quad C_1 = \frac{sin(\phi)}{\omega_0 Z\big(1 - cos(\phi)\big)},$$

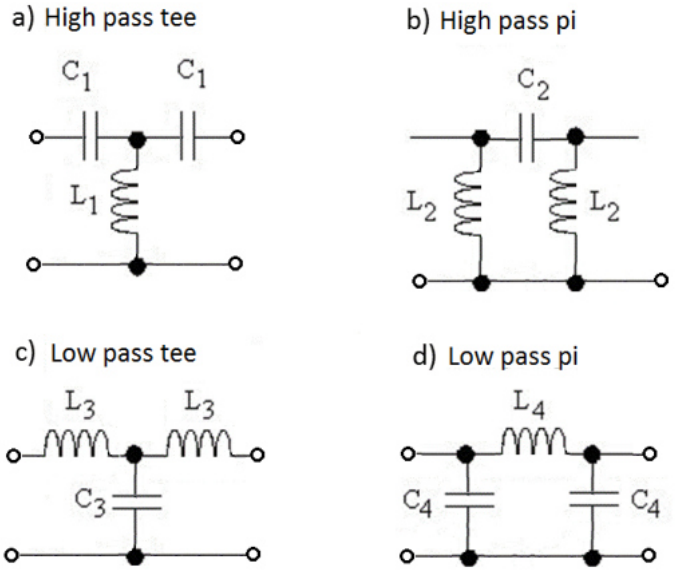

Figure 3.21: Four different phase shifters which can be used for the preamplifier decoupling. The high pass tee in (a) was chosen for the interface.

where ϕ is the phase shift and $Z = \sqrt{Z_{in} Z_{out}}$ is the impedance. The equations and more detailed information about phase shifters can be found [23]. For a frequency $\omega_0 = \frac{f_0}{2\pi} \approx \frac{123MHz}{2\pi}$, an input and output impedance of $Z_{in} = Z_{out} = Z_0$ and a desired phase shift of $\phi = 90° \approx 1.57$ rad the inductance $L_1 \approx 64$ nH and the capacitance $C_1 \approx 26$ pF were obtained.
For the interface the capacitors were arranged symmetrically by splitting each capacitor of double the value in series to the ports the same way it was done for the matching module. The electric circuit can be seen in the final interface Figure 3.12. A picture of the built module can be seen in Fig. 3.22 with following components and their corresponding values:

1) The self-built inductor $L_\Phi \approx 70$ nH.

2) Two capacitors are split into four with $C_\Phi = 36$ pF.

3) 4-pin socket to connect the preamplifier.

4) Black 4-pin connector to plug the matching module.

These values were found to accomplish the preamplifier decoupling best, which results in an phase shift of 110°.

Additionally, the preamplifier decoupling was examined theoretically using Pasan and then compared to reality by measuring the modules with the network analyzer. Therefore the interface had to be examined from the other side than considered for the tuning and matching. As shown in Fig. 3.23, without the phase shifting module, an open was obtained for the desired resonance frequency. If a phase shifter in combination with a low impedance preamplifier as described above is used instead, shown in Fig. 3.24, an impedance $Z_{decoupl} \ll Z_{no-\Phi}$ is obtained. The frequency depending curve in combination with the phase shifter, shown in the Smith chart r.h.s.

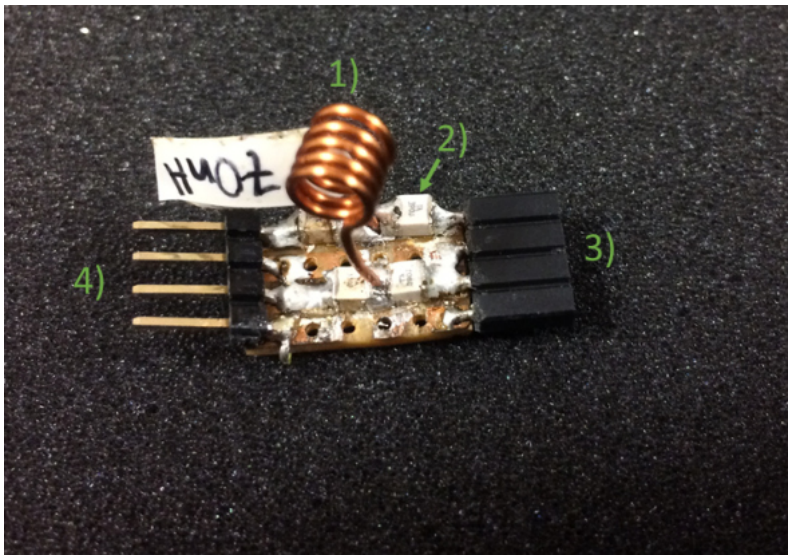

Figure 3.22: Picture of the final built decoupling module.

depends strongly on the load impedance (the impedance of the preamplifier). The resistance of the preamplifier is 1.5 Ω, the reactance of the preamplifier can be changed within a range from 3 Ω to 32 Ω . This behaviour is discussed later in more detail.

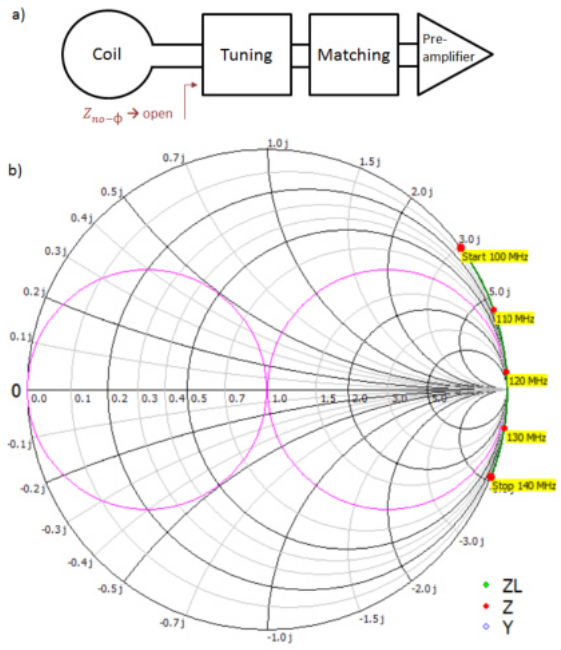

Figure 3.23: Preamplifier decoupling investigation without phase shifter. Sketch of the impedance (a) and the Smith chart for a frequency range (b).

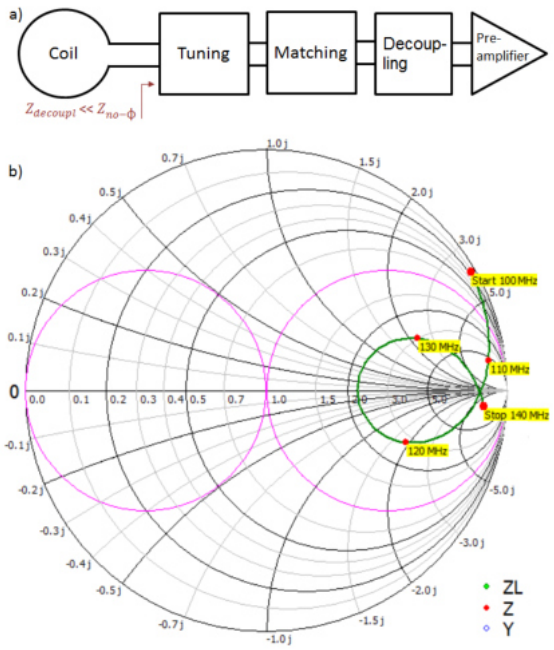

Figure 3.24: Preamplifier decoupling investigation with phase shifter. Sketch of the impedance (a) and the Smith chart for a frequency range (b).

The impedances of the interface with and without the decoupling module were measured with

the VNA. This comparison was performed with a mixed-mode measurement as described in Sec. 3.1.1. The 3-pin coil socket of the tuning module together with a self-built adapter was used to plug the two ports of the VNA. As shown in Fig. 3.25 (a) the self-built adapter has a common ground (pin in the middle) and the two ports are located on the outer pins, shown in Fig. 3.25 (b). The measurement details are shown in Sec. 4.1.1.3.

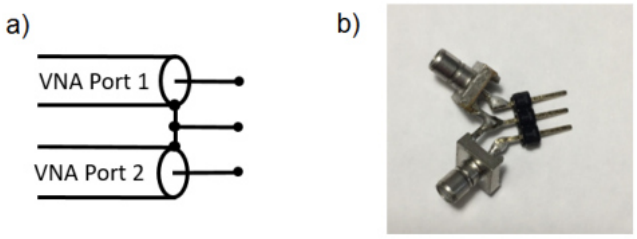

Figure 3.25: A sketch (a) and a picture (b) of the self-built adapter for a SDD11 measurement with the vector network analyzer.

3.2.2.4 Compact interface redesign

For the coaxial coil array, which is described in detail later, three compact interfaces with all lumped components on a smaller single copper-plated circuit board were designed and built. Only one pin socket for the coaxial coil and one socket for the preamplifier was used. The inductors were changed to smaller, industrially manufactured ones: As described earlier, the inductance of the self-built inductors was obtained by building a resonant circuit with a known capacitance and measuring the resonance frequency. The inductance was calculated from this frequency. Since this method is not very accurate, changing to the smaller air core inductors will also change the values of the other lumped components of the interface.
The electrical circuit of the compact interface can be seen Fig. 3.26. As shown in the electrical circuit of the modular interface in Fig. 3.12, two matching capacitors were neighbouring the decoupling capacitors. At both ports they can be combined: C_M is in series to C_Φ an can be added to $C_{M\Phi}$.

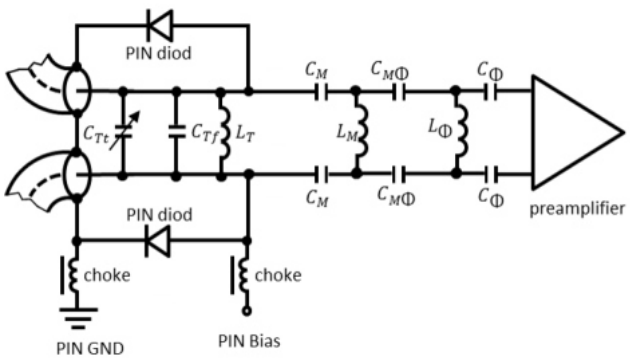

Figure 3.26: Electrical circuit of the compact interface. The coaxial coil is only indicated on the l.h.s.

For the electrical circuit of the compact interface a copper-plated circuit board was used. The board was fully covered with copper and the electrical circuit was machined into the circuit board using a rotary tool. The electrical circuit board of Interface 1 is shown in Fig. 3.27 (a) and the electrical circuit board of the interfaces 2 and 3 are shown in Fig. 3.27 (b).

Figure 3.27: Circuit boards of the three interfaces: (a) Interface 1, (b) Interface 2 and Interface 3. The white dots indicate drilled holes.

Interface 1

By combining all components on one interface and using the square air core inductors, modifications need to be performed to obtain a good tuning, matching and preamplifier decoupling, which are summarized in Tab. 3.1.

Lumped component	Interface 1	Interface 2	Interface 3
tuning inductance L_T [nH]	68	68	68
tuning trimmer capacitor C_{Tt} [pF]	2 - 6	2 - 6	2 - 6
fixed tuning capacitor C_{Tf} [pF]	18	22	18
matching inductance L_M [nH]	360	500	430
matching capacitor C_M [pF]	8.2	8.2	8.2
decoupling inductor L_Φ [nH]	68	68	68
decoupling capacitor C_Φ [pF]	39	39	39
combined capacitor $C_{\Phi M}$ [pF]	6.8	6.8	6.8

Table 3.1: Values of the lumped components of the compact interfaces.

A picture of the Interface 1 can be seen in Fig. 3.28. The coaxial coil connected to the interface is shown partly on the l.h.s., while the preamplifier, which is connected to other side of the interface, is shown on the r.h.s. The 3-pin socket for the coaxial coil was directly soldered on the PIN diodes. The 4-pin socket for the preamplifier was placed in the four holes of the circuit board and soldered. The two outer pins of the socket were connected by the yellow cable and the inner pins are directly connected. As shown, a preamplifier with 90° pins is connected to the interface.

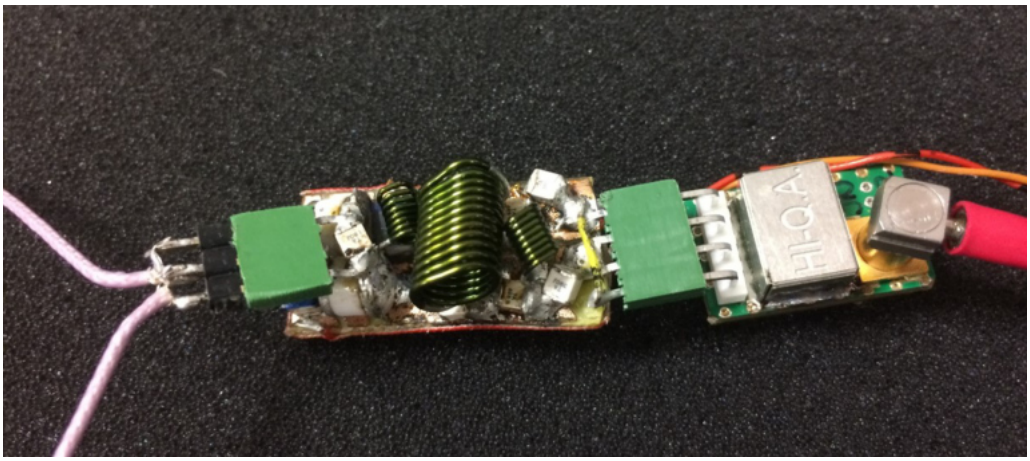

Figure 3.28: Picture of the Interface 1 with the connected coaxial coil (partly shown, l.h.s.) and the preamplifier (r.h.s).

Interface 2

Some changes compared to the Interface 1 were done on Interface 2. The circuit board is shown in Fig. 3.27 (b). Three drilled holes in the board (l.h.s.) were used to connect the coaxial coil from the bottom with a 3-pin socket. To reduce the total length of the interface the 4-pin socket for the preamplifier was arranged vertically and the pins of the preamplifier were bent to a u-shape. The pins of the green 4-pin socket were positioned in the holes of the interface on the right hand side. Additionally, the outer pins of the socket were connected via a connection on the interface. Another difference to Interface 1 is that the adjustable capacitor was placed on top of the PIN diodes for easily accessible tuning. A picture of Interface 2 is shown in Fig 3.29.
The values of the lumped components are also shown in Tab. 3.1.

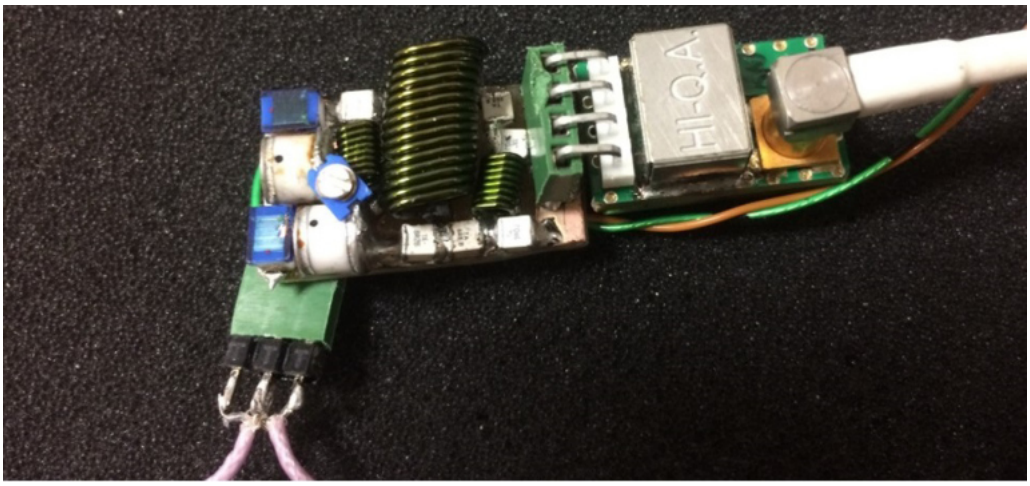

Figure 3.29: The built Interface 2 connected to the coaxial coil and the preamplifier.

Interface 3

The same circuit board as described for Interface 2 was used for the Interface 3. Only the socket for the coaxial coil was positioned in line with the interface, as shown in Fig. 3.30. Experimentally it was found that the matching inductance $L_{M3} = 430$ nH and consequently the related fixed tuning capacitance $C_{Tf3} = 18$ pF had to be changed for a well tuning and matching. All other values of the lumped components stayed the same, and can be seen in Tab. 3.1.
Although Interfaces 2 and 3 are nearly identically (the position of the coaxial coil socket should not change the electrical behaviour) different tuning and matching components are necessary.

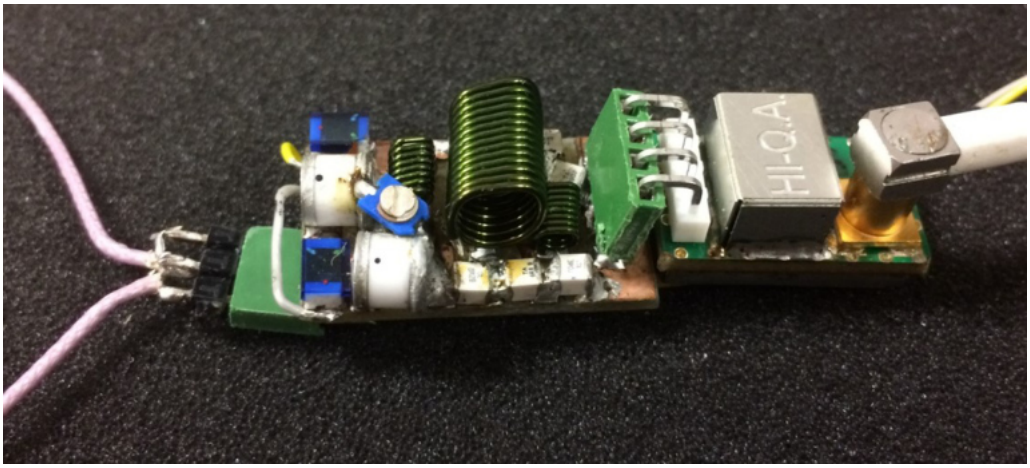

Figure 3.30: Picture of the built Interface 3 with the coaxial coil and the preamplifier.

3.2.3 Testing the radiofrequency coil's performance

3.2.3.1 Bench test experiments

The Q-factor, which is described in Sec. 2.2.3, was measured with the double-loop probe. An unloaded and a loaded measurement on a phantom was performed. The measurement of coaxial coils was performed with and without the compact Interface 1 to study its influence. Different coils were used to study their behaviour:

- ◇ Thin coaxial coil
  The thin coaxial cable from the Siemens receive MR-plug was used as one-gap coaxial coil with a diameter of approximately 80 mm.

- ◇ Thick coaxial coil
  A different, thicker coaxial cable from the company Hubner + Suhner, as described in Sec. 3.1.5 was used. The diameter of the coil was approximately 90 mm.

- ◇ Conventional loop coil
  The coaxial coils were compared to a conventional loop coil with a standard interface, as shown in Fig. 2.10 and a diameter of approximately 80 mm. The tuning capacitor is

adjustable: C_T : 6.5 pF to 30 pF, for the matching the capacitors C_{m1} : 33 pF plus an adjustable capacitor in parallel also with a range of 6.5 pF to 30 pF was used as well as $C_{m2} = 27$ pF and the inductor for detuning $L = 68$ nH were used.
Another coil without an interface was used. The standard loop coil consisted of one capacitor with 120 pF in series to another 120 pF which was soldered parallel to a trimmer (2 to 6 pF) for fine tuning.

The detailed results of the Q-factor measurement loaded and unloaded for the three different coils are shown in Sec. 4.1.1.4.

Additionally, a resonance frequency spectrum was measured with the Interface 2: the CC with the interface was connected to a 50 Ω resistance, plugged in the preamplifier port. The spectrum was measured with the double-loop probe and can be seen in Fig. 4.7 for a frequency range of 10 MHz to 550 MHz.

3.2.3.2 MR experiments

Experimental Setup

The performance of the single-channel coaxial coil was evaluated in a whole-body MR scanner Magnetom Prisma-Fit 3T, Siemens Healthineers, Erlangen, Germany. One coaxial coil with a diameter of around 80 mm was connected to a compact interface. The interface was connected with the preamplifier, which was connected to a coaxial cable and plugged into an 8-channel receive plug. On the cable of the receive plug floating cable traps tuned to 123 MHz were positioned. The DC cable of the interface for detuning the coil was also connected to the receive plug. Another cable trap was placed around the coaxial cable and the DC cable to reduce common mode currents.

Phantom imaging

MR sequences to compare the performance of a conventional loop coil with a single-channel coaxial coil were performed. A standard loop coil with an interface as described in Sec. 3.2.3.1 was compared to a coaxial coil with the same diameter of 80 mm, connected to a compact interface. Each receive-coil was placed on the chest of the torso phantom. In the middle of the coil a vitamin pill was positioned to easily locate the coil. A picture of the experimental setup with the direction of the B-field is shown in Fig. 3.31.
The MR sequence was performed twice in succession, for the CC and for the conventional coil. It is important to place the coils at the same position to provide a reasonable comparison. A 2D gradient echo sequence with sagittal slices was run with the following parameters:

- ◇ repetition time $T_R = 300$ ms
- ◇ slice thickness: 2 mm, 12 slices
- ◇ echo time $T_E = 10$ ms
- ◇ acquisition matrix: 256×256

- ◇ field of view (FoV): $192 \times 192\ mm^2$
- ◇ Resolution: $0.75 \times 0.75\ mm^2$
- ◇ Number of averages: 1
- ◇ Acquisition time $T_A = 1:16$ min
- ◇ Bandwidth: 130 Hz/px
- ◇ flip angle $\alpha = 60°$

To calculate the SNR, the mean signal intensity in the region of interest (ROI) was divided by the standard deviation of the signal intensity outside of the torso phantom. As ROI, an area in the phantom gel and in the vitamin pill were selected. The SNR was calculated for each ROI, for both, the CC and the copper coil.

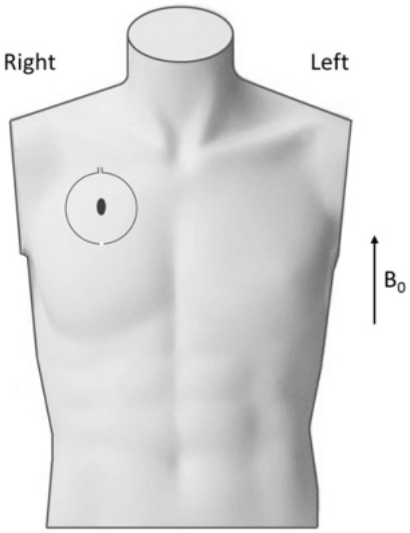

Figure 3.31: Experimental setup of the single-channel coaxial coil on a torso phantom. The measurement was performed twice, for the coaxial coil and the conventional coil. In the picture the coaxial coil, the vitamin pill and the B-field direction are shown.

Fruit imaging

Additionally, MR measurements with the 1-channel coaxial coil were performed using an orange. The coil was positioned around the fruit as shown in Fig. 3.32 with an indicated B_0-field direction. Coronal slices using a T_2 weighted double echo 3D sequence (T2 de3D) with the following parameters were acquired:

- ◇ repetition time $T_R = 16.65$ ms
- ◇ echo time $T_E = 5.69$ ms
- ◇ acquisition matrix: $192 \times 192 \times 176$
- ◇ FoV: $79 \times 79 \times 73\ mm^3$
- ◇ Resolution: $(0.42\ mm)^3$
- ◇ Number of averages: 1
- ◇ Acquisition time $T_A = 7:21$ min
- ◇ Bandwidth: 195 Hz/px
- ◇ flip angle $\alpha = 25°$

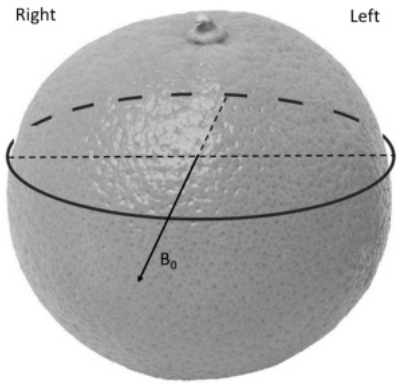

Figure 3.32: Experimental setup of the MR measurement of an orange. The position of the coaxial coil and the B_0-field direction of the scanner are shown.

3.3 3-channel coaxial coil array development

In this section the development of the 3-channel coaxial coil array is described. The array consists of the three coaxial coils, each connected to one of the compact interfaces described in the previous section.
The layout of the coils within the array (inter-element decoupling), the implementation of the 3-channel array and the final MRI test measurements on a phantom are described in this section.

3.3.1 Array layout

When several coils are used, it is important to consider the arrangement of the coils to each other. Due to mutual inductive coupling unwanted interactions among the coils occur. To reduce them to a minimum, geometric decoupling was employed and the following layout was designed.
The three coaxial coils were positioned along an equilateral triangle: Each coil center was placed at one corner of the triangle as shown in Fig. 3.33. The coils were built with a diameter $d_{coil} \approx 80$ mm. The distances between the centers of the coils have an optimal distance d_{opt}. Since the coaxial coils might behave differently compared to conventional loop coils, the value of d_{opt} was studied experimentally, which is described next.

3.3.1.1 Two-element decoupling

The optimal distance d_{opt} between two circular coaxial coils was studied; whereas d_{opt} is defined as the distance between the centers of two coils when their mutual coupling is minimal. d_{opt} of two conventional loop coils can be calculated as described by Römer et al. using Eq. 2.13 [13]. The optimal distance for two coaxial coils was obtained experimentally by measuring the S-parameters:
Two identical coaxial coils with a diameter $d_{coil} \approx 80$ mm were positioned on the flat bottom phantom of the torso phantom. One coil was fixed at a particular position while the position of the other coil was varied. A sketch of the experimental setup is shown in Fig. 3.34. Both coils

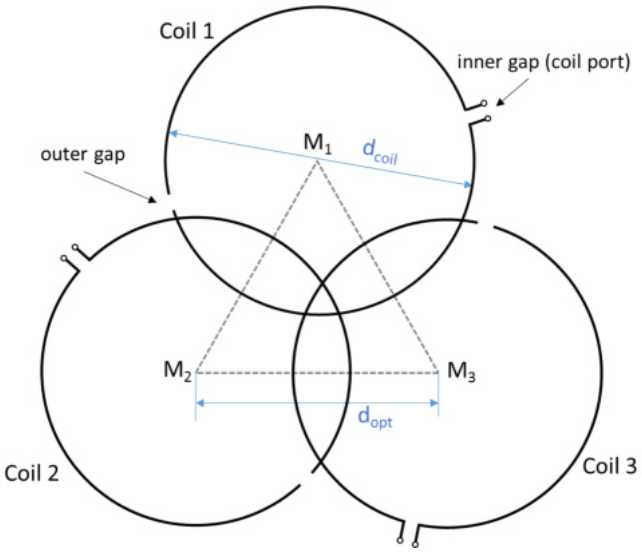

Figure 3.33: Layout of the coaxial coil array. Three identical coaxial coils with a diameter d_{coil} were positioned at the corners of a equilateral triangle with a side d_{opt}.

were connected via a compact interface without the preamplifier to the network analyzer. Port 1 and 2 were connected to coil 1 and coil 2, S_{11} as well as S_{22} was measured. Additionally, the coupling of the coils was obtained with the S_{21} parameter by sending the VNA signal to coil 2 and obtaining the signal at coil 1. The coupling was measured at 123 MHz. The distance d between the two coils was varied from 160 mm to zero, where the coils were on top of each other.

An optimal distance $d_{opt} \approx 62$ mm was obtained, which is similar to the calculated distance for conventional loop coils, given by Roemer [13]. The detailed results of the measurements are shown in Sec. 4.2.1.1.

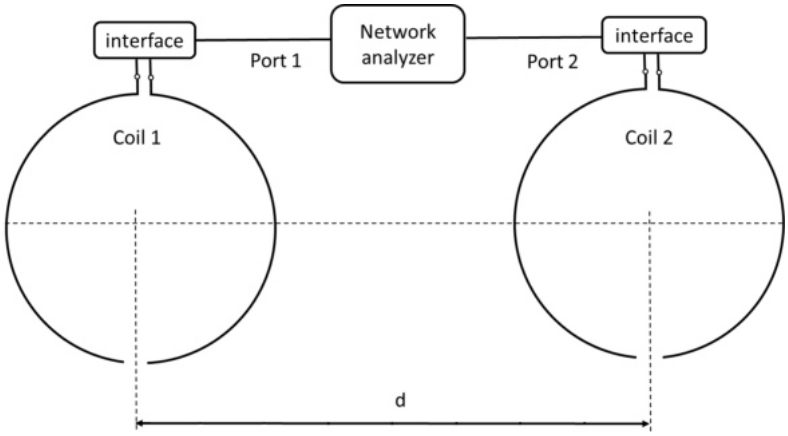

Figure 3.34: Sketch of the experimental setup for determining the optimal distance d_{opt} between two elements for decoupling. The distance between the identical coils was varied and the S-parameters were obtained to find the lowest coupling.

3.3.1.2 Three-element decoupling

After implementing the array on textile tissue as described in Sec. 3.3.2 the S-parameter measurement was repeated for the three coil array. The three port measurement was performed twice on different positions on the phantom; at a flat position and at a position where the array was bent strongly (under the axilla, at the latissimus dorsi of the torso phantom). The details of the measurements are shown in section 4.2.1.2.

3.3.2 Implementation

Three thin coaxial cables prepared with one outer gap were woven into a thin wide-meshed textile tissue such that the equilateral triangle layout, as described above, was obtained. Thereby, a fixed position of the coils within the array for a good inter-element decoupling was obtained, while the array stayed very flexible. The thin textile allowed a very flexible movement of the coils when the array was positioned on a curved shape. In contrast to the single-channel connectors, here the ends of the cables were soldered onto a small copper circuit-board with three short copper pins to connect to the interface. The reason for this change was that the black connectors turned out to be slightly ferro-magnetic, thus, producing artefacts in the MR images.
The wide-meshed textile tissue with the coils was sewn onto a slightly more rigid, light-weight red foam padding ($\approx$ 3 mm thick) to protect the array with the interfaces and the preamplifier. A white synthetic leather was sewn as the outermost layer. A picture of the three textiles with the woven coils is shown in Fig. 3.35.

The final implemented array with all components is shown in Fig. 3.36. The ports of the three coaxial coils were connected to the interfaces. Each compact interface was connected to a preamplifier which was then connected via a coaxial cable to the MR scanner. Additionally, one floating cable trap was placed around the DC cable and coaxial cable for each interface.

3.3.3 MRI test measurements with the final array

The MR performance of the final implemented 3-channel coaxial coil array was tested in the whole-body MR scanner on a torso phantom as well as on a pineapple and on a melon.
A black, a blue, and a brown CC were connected (in this order) to a compact interface and a preamplifier, numbered with 1, 2 and 3. The DC cables of the interfaces and the coaxial cables connecting the receive coil were plugged into a custom-built 8-channel receive plug adapter. A picture of the setup scanning a water melon can be seen in Fig. 3.38.

3.3.3.1 Torso phantom measurements

Phantom measurements were performed to check if the array is functioning properly. The array was positioned in the middle of the chest of the phantom, as indicated in Fig. 3.37 and connected to the scanner as described above.
A gradient echo 3D scan with transversal slices was performed using the following parameters:

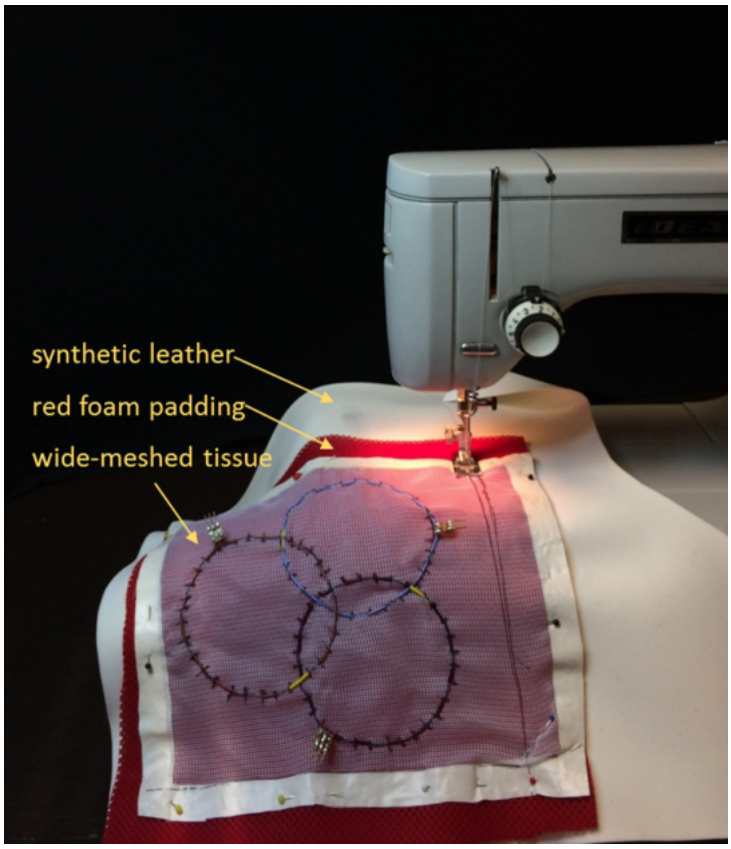

Figure 3.35: Picture of the different textile tissues with the woven coaxial coils while sewing.

- ◇ repetition time $T_R = 6.3$ ms
- ◇ echo time $T_E = 2.64$ ms
- ◇ slice thickness: 3 mm, 104 slices
- ◇ acquisition matrix: $192 \times 156 \times 104$
- ◇ FoV: $318 \times 258 \times 312\ mm^3$
- ◇ Resolution: $1.65 \times 1.65 \times 3\ mm^3$
- ◇ Number of averages: 1
- ◇ Acquisition time $T_A = 1:42$ min
- ◇ Bandwidth: 510 Hz/px
- ◇ flip angle $\alpha = 5°$

3.3.3.2 Noise correlation and g-factor maps

To obtain the geometry factor (described in Sec. 2.2.3), the noise correlation and a fully sampled 2D gradient echo were measured. The array was positioned on the torso phantom as described above. Without any excitation puls, the receive array was used to measure the noise, which is correlated due to the overlapping sensitivity profiles and coupling of the coils. This data was used to calculate the noise correlation matrix. 2D gradient echo scans with coronal and transversal slices and phase encoding in right-left direction was performed:

- ◇ repetition time $T_R = 470$ ms
- ◇ echo time $T_E = 3.23$ ms
- ◇ slice thickness: 3 mm
- ◇ acquisition matrix: 288×288

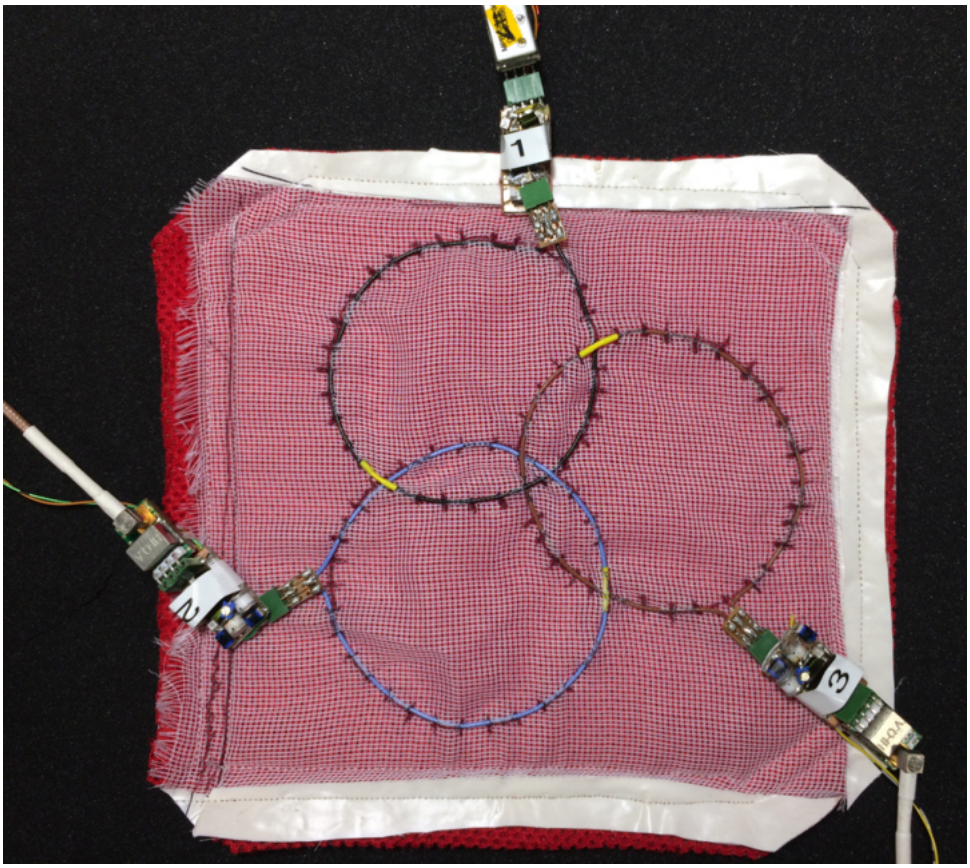

Figure 3.36: Final 3-channel array implemented on textile tissue. The three identical coils ($d_{coil} \approx$ 80 mm) were connected to the compact interfaces (labelled with 1, 2, and 3) and the preamplifiers. The coaxial cables and the DC cables are shown partly.

- ◇ FoV: $312 \times 312\ mm^2$ (coronal)
- ◇ FoV: $381 \times 381\ mm^2$ (transversal)
- ◇ Resolution: $1.08 \times 1.08\ mm^2$ (coronal)
- ◇ Resolution: $1.32 \times 1.32\ mm^2$ (transversal)
- ◇ Number of averages: 1
- ◇ Acquisition time $T_A = 2:14$ min
- ◇ Bandwidth: 510 Hz/px
- ◇ flip angle $\alpha = 20°$

Using the pseudo-multiple replica methode [10] the accelerated SNR maps for R=2 and R=3 were calculated. The accelerated SNR maps were divided by the non-accelerated map and the root of the acceleration factor to obtain the g-factor maps:

$$g = \frac{SNR_R}{SNR_{full}}\sqrt{R}.$$

The noise correlation matrix Ψ as well as the SNR and the g-factor maps for different acceleration factors are shown in the Results, Sec. 4.2.2.1.

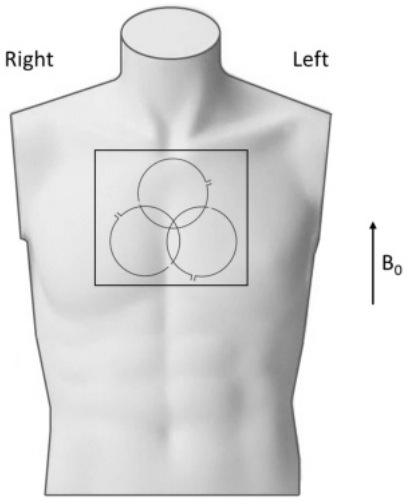

Figure 3.37: Experimental setup of the torso phantom measurement with the final 3-channel coaxial coil array.

3.3.3.3 Fruit MR measurements

Additional MR experiments with a pineapple and a watermelon were performed to demonstrate the flexibility of the 3-channel coaxial coil array.

Watermelon

Two MR scans with a watermelon were performed. The position of the array on the melon is shown for both scans in Fig. 3.38 (a), (b). A picture of the experimental setup with the 3-channel array, the interfaces connected to the receive plug and the cable traps is shown in 3.38 (c). A T_2 weighted double echo 3D (T2 de3D) sequence with transversal slices was performed:

- ◇ repetition time $T_R = 15.71$ ms
- ◇ echo time $T_E = 5.22$ ms
- ◇ slice thickness: 3 mm
- ◇ acquisition matrix: $320 \times 290 \times 256$
- ◇ FoV: $230 \times 208 \times 184$ mm^3
- ◇ Resolution: 0.72 mm^3
- ◇ Number of averages: 1
- ◇ Acquisition time $T_A = 15:15$ min
- ◇ Bandwidth: 200 Hz/px
- ◇ flip angle $\alpha = 25°$

Another T2 de3D with coronal slices using following parameters was run:

- ◇ repetition time $T_R = 14.97$ ms
- ◇ echo time $T_E = 4.85$ ms
- ◇ slice thickness: 3 mm
- ◇ acquisition matrix: $256 \times 256 \times 20$
- ◇ FoV: $131 \times 131 \times 40$ mm^3
- ◇ Resolution: $0.51 \times 0.51 \times 2$ mm^3
- ◇ Number of averages: 16
- ◇ Acquisition time $T_A = 10:05$ min
- ◇ Bandwidth: 195 Hz/px
- ◇ flip angle $\alpha = 25°$

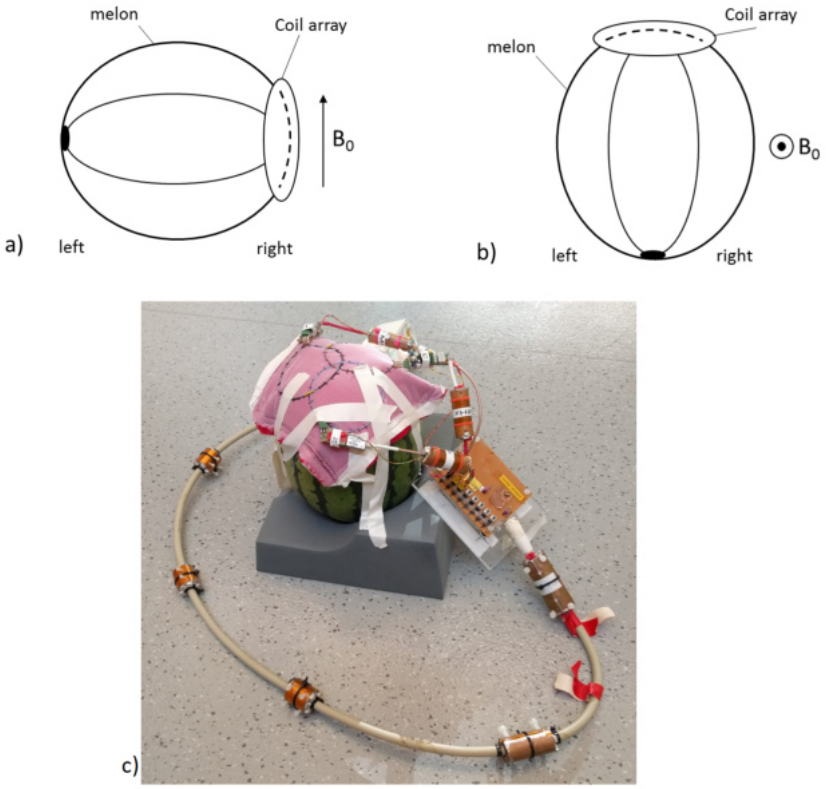

Figure 3.38: Sketch of the array position on the watermelon for the transversal setup (a) and the coronal setup (b) and a picture of the experimental setup with all components (c).

Pineapple

For this measurement the coil array was positioned on the side of the fruit; a picture of the experimental setup with the B_0-field direction is shown in Fig. 3.39.
A T_2 weighted double echo 3D (T2 de3D) sequence was performed:

- ◇ repetition time $T_R = 15.98$ ms
- ◇ echo time $T_E = 5.35$ ms
- ◇ slice thickness: 3 mm
- ◇ acquisition matrix: $256 \times 232 \times 208$
- ◇ FoV: $154 \times 139 \times 125$ mm^3
- ◇ Resolution: 0.6 mm^3
- ◇ Number of averages: 1
- ◇ Acquisition time $T_A = 10:05$ min
- ◇ Bandwidth: 195 Hz/px
- ◇ flip angle $\alpha = 25°$

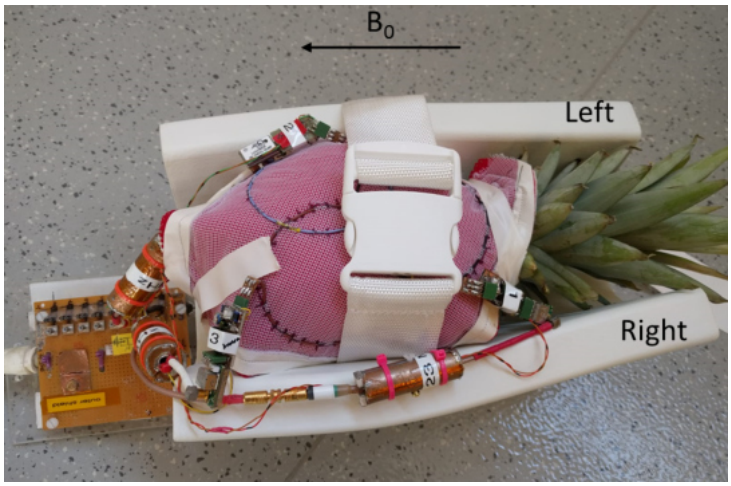

Figure 3.39: Experimental setup of the MR measurement of a pineapple. The coil array, the three interfaces with the cables and their cable traps are shown. L.h.s on the bottom the 8-channel receive plug adapter is partly visible.

Chapter 4

Results

4.1 Single-channel coaxial coil

4.1.1 Bench tests

4.1.1.1 Coaxial coil shape

The results of the comparison of coaxial coils with circular and elliptic shape is shown in Tab. 4.1. Only the shift between the circular and the elliptic measurement was studied here, the overall behaviour is discussed below. CCs with one, two, and three gaps, and a diameter of approximately 90 mm were used.

number of gaps	Coaxial coil shape	Resonance frequency f_0 [MHz]			Quality factor Q			S-parameter S_{21} [dB]	
		unloaded	loaded	change unl./l. [%]	unloaded	loaded	ratio unl./l.	unloaded	loaded
$n_g = 1$	circular	111.4	110.6	0.7%	146.0	49.0	3.0	-43.4	-52.4
	elliptic	114.7	113.9	0.7%	140.0	59.0	2.4	-46.1	-53.2
	shift circular/elliptic [%]	2.9%	2.9%	-	4.3%	16.9%	-	5.9%	1.5%
$n_g = 2$	circular	227.6	224.0	1.6%	160.0	16.0	10.0	-39.2	-57.7
	elliptic	233.8	231.7	0.9%	162.0	21.0	7.7	-41.6	-58
	shift circular/elliptic [%]	2.7%	3.3%	-	1.2%	23.8%	-	5.8%	0.5%
$n_g = 3$	circular	339.9	350.0	2.9%	131.0	8.0	16.4	-39.6	-64
	elliptic	351.2	351.3	0.0%	165.0	15.0	11.0	-40.6	-63.7
	shift circular/elliptic [%]	3.2%	0.4%	-	20.6%	46.7%	-	2.5%	0.5%

Table 4.1: Measurement of the resonance frequency, the Q-factor and the S-parameters for coaxial coils without an interface for a different number of gaps. A circular and an elliptic shape was investigated.

The resonance frequency between both setups changed only by a few percent. The mean value of the difference of f_0 was around 3% and 2% for an unloaded and loaded measurement, respectively. The change in quality factor for an unloaded measurement was relatively small for one and two gaps, but was considerably high for three gaps. The loaded Q-factor differs much more between the elliptic and circular setup, which can be explained by the smaller sample volume seen by the elliptic coil. Also for the loaded Q, the difference between circular and elliptic coil increases with the number of gaps. The reason for this is unclear so far.
The S_{21}-parameter for a different number of gaps, using the double-loop probe at a constant

distance to the coil are also presented in Tab. 4.1. Only the circular coil shape was studied in this case.

4.1.1.2 Resonance frequency of multi-gap coaxial coils

The resonance frequency was increasing with the number of gaps n_g. Empirically it was found that

$$f_{0,n_g} \approx n_g \cdot f_{0,1}$$

is a good approximation, where $n_g = 1, 2$ or 3 and $f_{0,1}$ is the resonance frequency of the one-gap CC. For a diameter $d \approx 90$ mm $f_{0,1} \approx 111$ MHz was obtained. Since the value of f_0 of the one-gap coaxial coil was close to the Larmor frequency for protons, this configuration was chosen for the 3-channel array. By changing the coil diameter to 80 mm, the correct resonance frequency of 123 MHz could be obtained.
The frequency change between unloaded and loaded was small. It increased with the number of gaps from around 1 % to 3 %.
The ratio of the quality factors was increasing with the number of gaps. For the one-gap CC Q-ratio ≈ 3, which means that a low sample dominance of the coil was obtained, while for three gaps a ratio of around 16 was obtained. It is noteworthy that the unloaded $Q_u = \frac{L\omega}{R_c}$ does not increase with frequency, and since L is not changing by the number of gaps, this means that R_c is increasing strongly with n_g. The reason for this behaviour still has to be investigated in future studies.

4.1.1.3 Single-channel interface

Tuning

For a desired frequency of 123 MHz the tuning condition X = 0 is fulfilled well, as seen in Fig. 4.1. By comparing the measured Smith chart to the calculated chart using Pasan (Fig. 3.16) it was found that both curves are similar, only a small tilt of the measured curve can be observed.

Detuning

The S_{21} measurement of the resonance frequency tuned and detuned obtained with the double-loop probe can be seen in Fig. 4.2 (a) and (b). In contrast to conventional loop coils the coils were detuned over a large frequency range.

Matching

The S_{11} parameter with the one-channel matching interface on the phantom is shown in Fig. 4.3 in a Smith diagram (yellow) and in an overlapping attenuation diagram (Log-Mag) showing the S-parameter in dB over the frequency range (cyan). One can see that the coil is well matched to $Z_0 = 50\,\Omega$ ($R \approx 49.5\,\Omega$, $X \approx 0.3\,\Omega$) at the desired resonance frequency of $f_0 \approx 123$ MHz

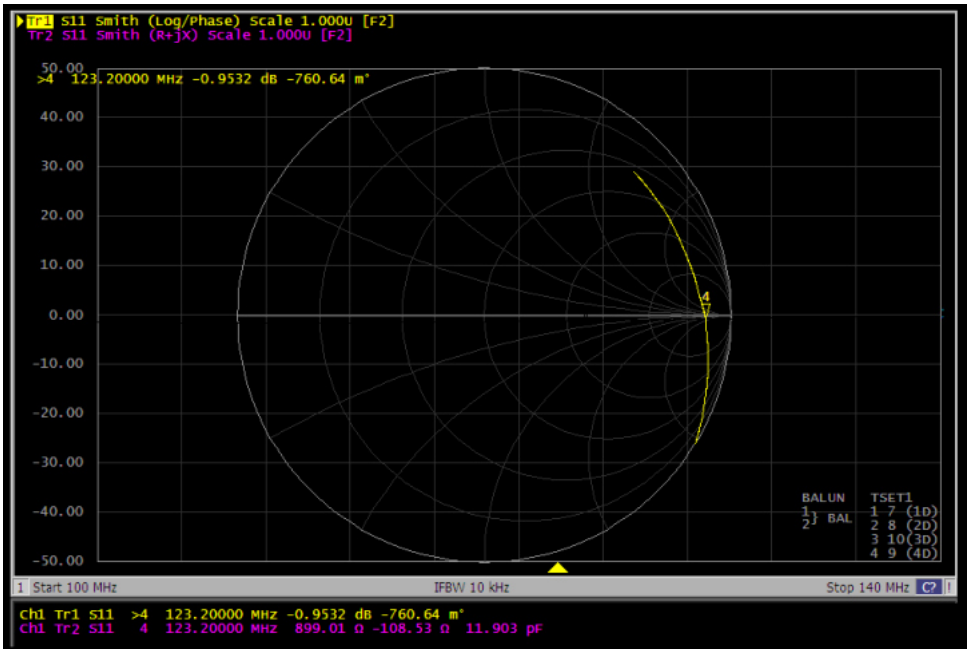

Figure 4.1: S_{11} measurement of the modular tuning interface with the vector network analyzer.

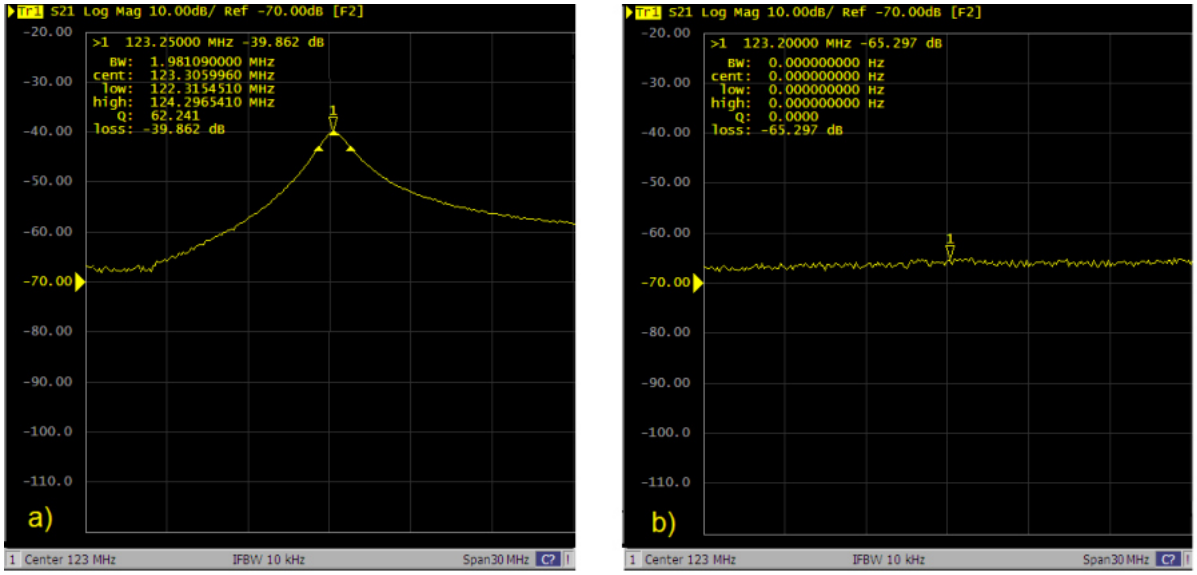

Figure 4.2: VNA measurement of the resonance frequency using a double-loop probe. The resonance frequency of tuned coil (a) and the detuned coil (b).

with $S_{11} \approx -43.9$ dB. The obtained Smith chart can be compared to the theoretical described circuit using Pasan, which is shown in Fig. 3.19. One can see that both charts are similar, a small shift of the measured parameter exists.

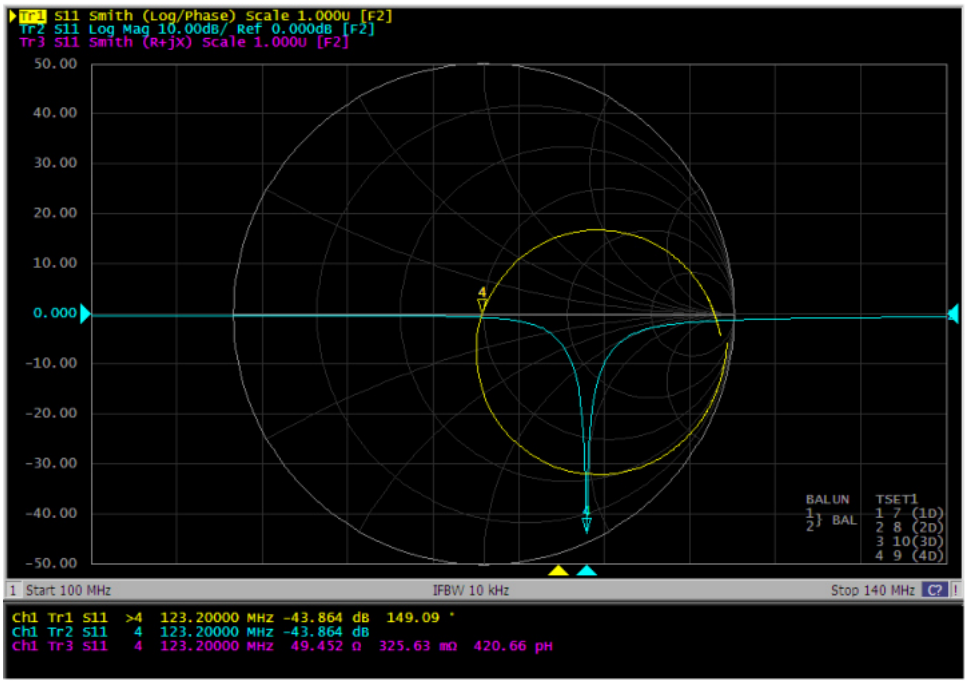

Figure 4.3: S_{11} measurement with the network analyzer of the modular matching interface.

Preamplifier decoupling

The mixed mode measurement of the impedance without and with the phase shifter are shown in Fig. 4.4 and Fig. 4.5. As expected, without the phase shifter a near open (705 - j1338 Ω) was obtained. Using the high pass tee network, a smaller impedance (375 + j20 Ω) was obtained. The minimum impedance (the Marker 1 in the figure) strongly depends on the impedance of the load, i.e. the preamplifier impedance. Since the reactance of the preamplifier can be adjusted, the minimum can be set to the desired resonance frequency. The measurement was compared to the calculation in Pasan: The general behaviour of the curves was similar. However, one can see that for the mixed mode measurement with the decoupling interface the minimum impedance was much larger compared to the minimum obtained theoretically with Pasan. The size of the "loop" strongly depends on the resistance of the load. A measurement with no load (i.e a short) and a load of approximately 2.8 Ω can be seen in Fig. 4.6 (a) and (b). Without a load the "loop" was much larger and very similar to Pasan. With the connected preamplifier, the measured impedance decreased and for higher resistances the curve changed and no resistive minimum was obtained any more.

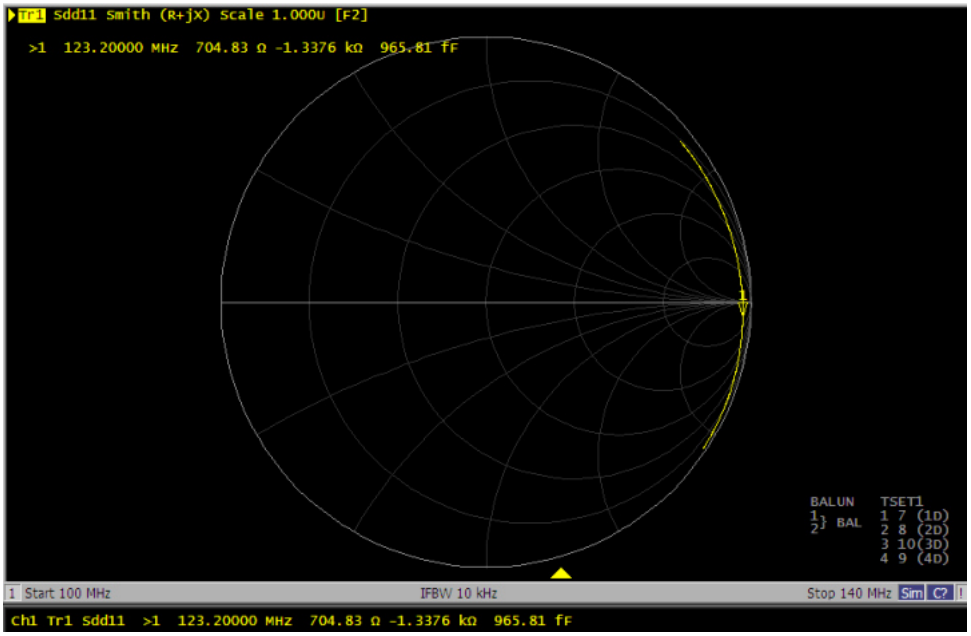

Figure 4.4: Smith chart of the mixed mode measurement S_{DD11} without the decoupling network.

4.1.1.4 Performance evaluation and comparison to standard loop coils

Loaded and unloaded Q-factors obtained with the double-loop probe are shown in Tab. 4.2 for three different coils. From the measurements with an interface, one can see that the highest Q-ratio was observed for the conventional coil (≈ 3.6). The thin coaxial cable had the lowest Q-ratio (≈ 1.5). The ratio of the Q-factors without interface was clearly larger than with interface.

Measurement with interface	$f_{0,L}$ [MHz]	Q_U	Q_L	Q-ratio
thin coaxial coil	123	96	66	1.5
thick coaxial coil	124	105	53	2.0
conventional copper coil	122	98	27	3.6

Measurement without interface	$f_{0,L}$ [MHz]	Q_U	Q_L	Q-ratio
thin coaxial coil	124	125	31	4.0
thick coaxial coil	120	235	22	10.7
conventional copper coil	122	330	28	11.8

Table 4.2: Q-factors measurement for different coils, with the interfaces (top) and without the interfaces (bottom).

Due to the electrical circuit of the interface, which also forms additional resonant circuits, additional peaks appear in the frequency spectrum. One resonance appears at 77.5 MHz and another resonance around 374 MHz. The S_{21} parameter was measured for a CC connected to the tuning and matching module and is shown in Fig. 4.7 for a frequency range from 10 MHz to 550 MHz.

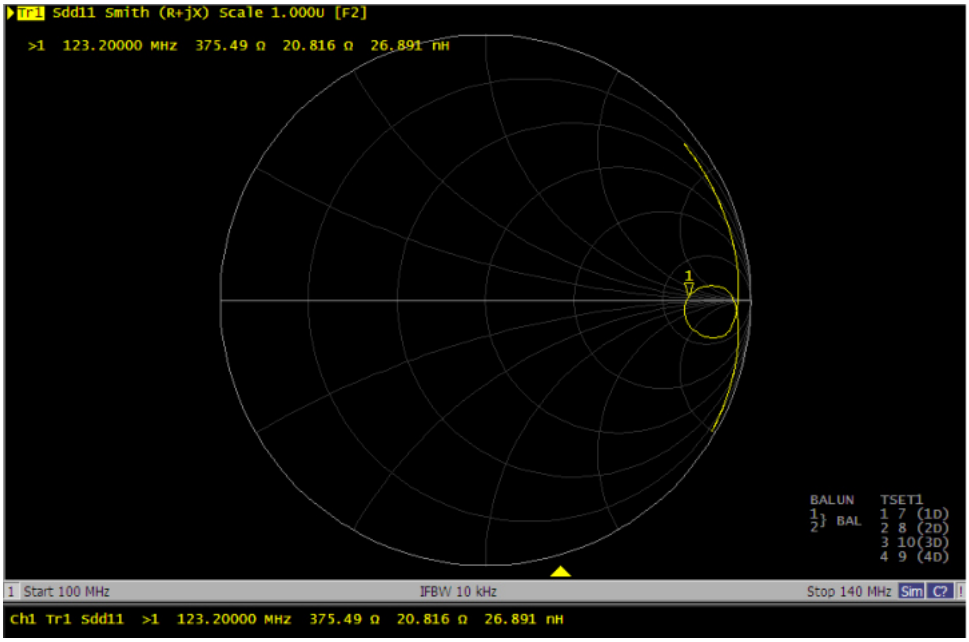

Figure 4.5: Smith chart of the mixed mode measurement S_{DD11} with the decoupling network.

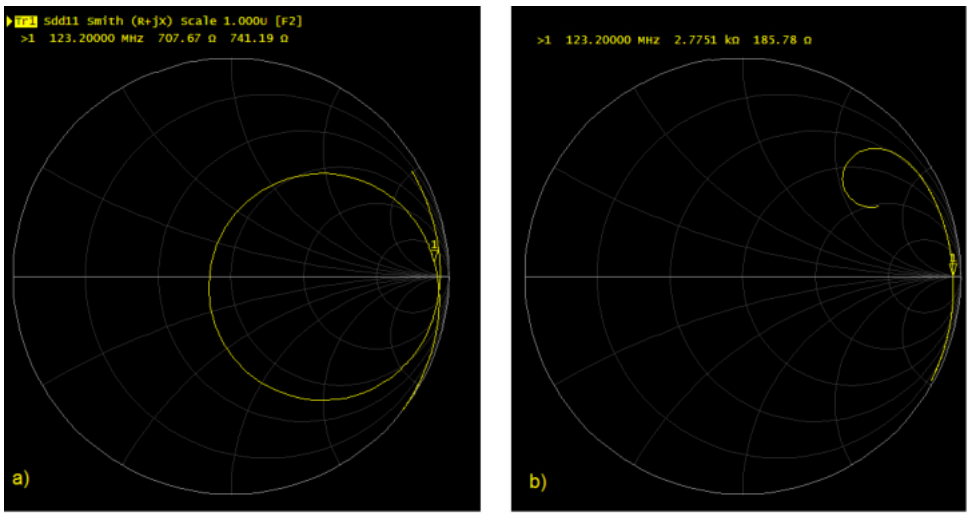

Figure 4.6: Smith chart of the mixed mode measurement S_{DD11} with the decoupling module with no load (short) (a) and a load of $2.8\,\Omega$ (b).

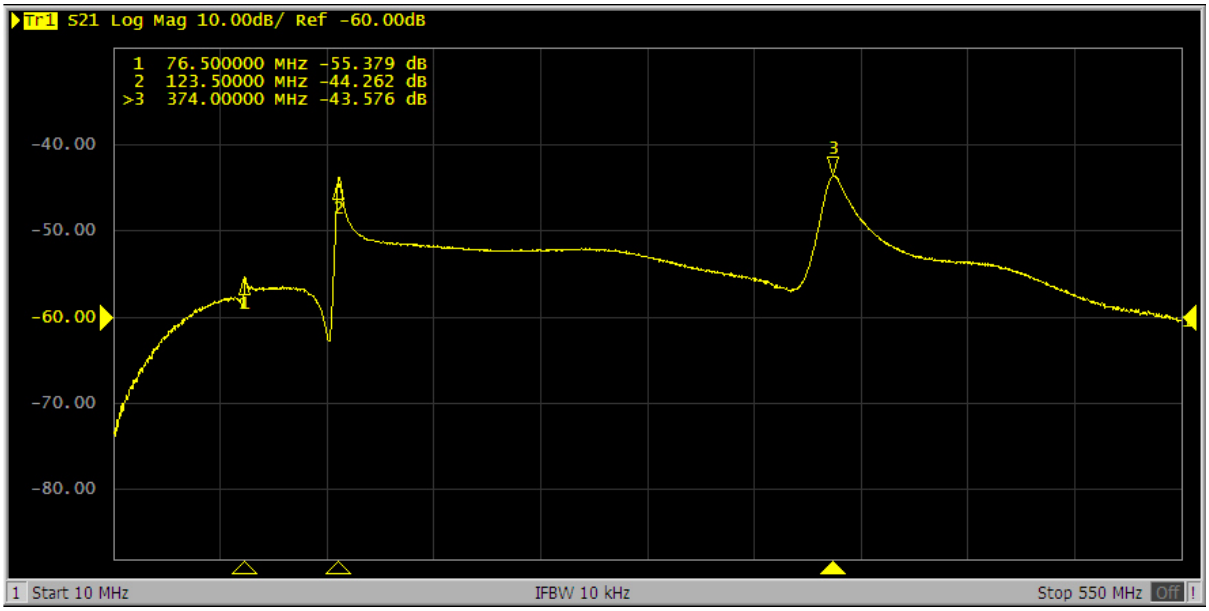

Figure 4.7: Additional peaks at ≈ 78 MHz (Marker 1) and ≈ 374 MHz (Marker 3) are observed, but are far away from $f_0 \approx 123$ MHz (Marker 2).

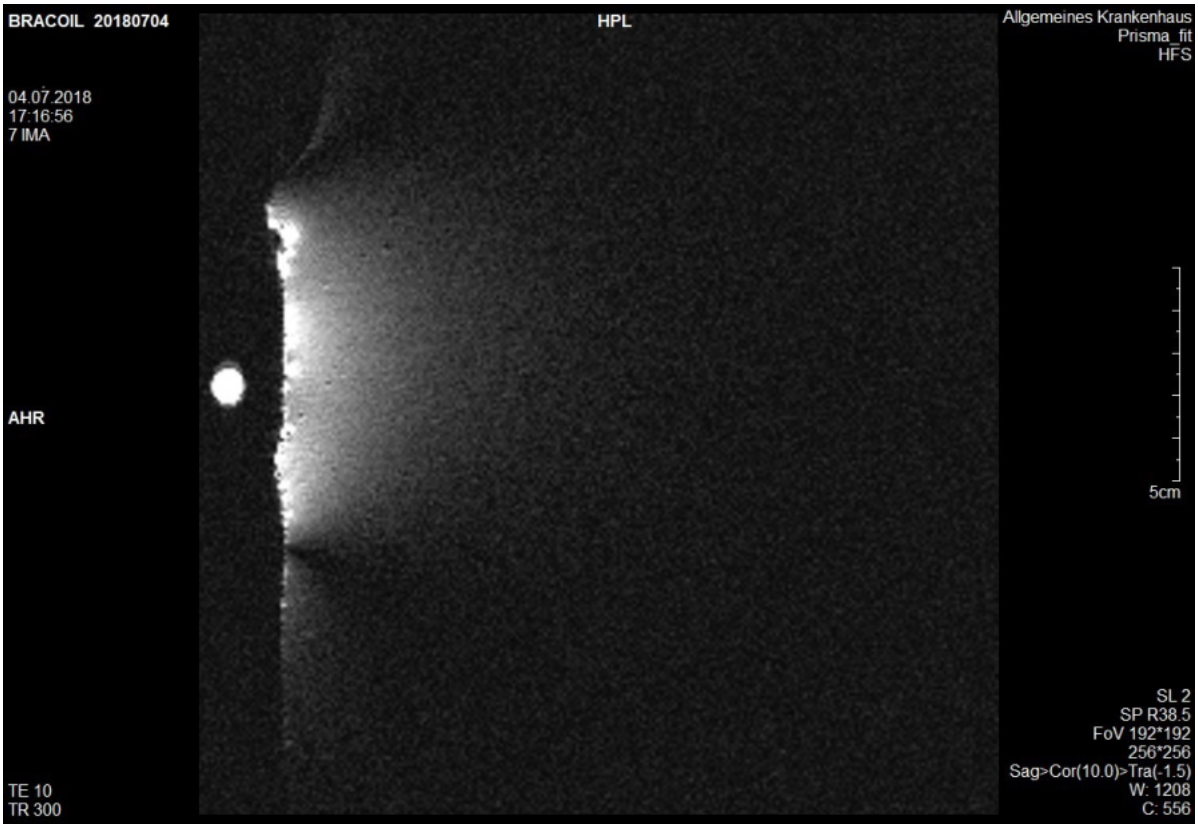

Figure 4.8: Sagittal MR scan of the torso phantom with the single-channel coaxial coil.

4.1.2 MR experiments

4.1.2.1 Phantom imaging

The SNR was obtained for the single-channel coaxial coil and was compared to a conventional loop coil, as described in the Methods section . A sagittal image obtained with the coaxial coil can be seen in Fig. 4.8. It shows the surface of the torso phantom (l.h.s) with the collarbone at the top of the high SNR region. Additionally, on the left border of the scan, the vitamin pill is visible as a circular shape. The quantitative SNR results are shown in Tab. 4.3.
The signal to noise ratio was measured for the phantom gel and the vitamin pill using different combinations of coaxial coils, interfaces and preamplifiers. As can be observed, the signal and the noise were higher using preamplifier 2, regardless of the CC and the interface. The mean SNR in the gel using a CC was $17.8 \pm 5\%$. In the vitamin pill the SNR was higher (since it is closer ot the coil), the mean value is $72.4 \pm 4\%$.
As shown in the first row, the SNR for the conventional coil is higher than for the CCs.
By comparing the averaged SNR of the coaxial coils with the conventional loop coil it was found that the SNR of the loop coils was approximately 1.3 times higher in the gel and around 1.4 times higher in the vitamin pill.

Coil		Phantom gel			Vitamin pill		
		Signal	Noise	SNR	Signal	Noise	SNR
conventional coil		57.5	2.5	23.0	255.6	2.5	102.2
Coaxial coil	Int. 1, orange CC, preamp. 1	508.0	30.1	16.9	2 130.0	30.0	71.0
	Int. 1, orange CC, preamp. 2	880.4	47.1	18.7	3 543.5	47.1	75.2
	Int. 1, blue CC, preamp. 1	557.7	32.4	17.2	2 237.5	32.4	69.1
	Int. 3, blue CC, preamp. 2	939.5	50.5	18.6	3 746.0	50.5	74.2

Table 4.3: SNR calculation for a single-channel coaxial coil and a conventional loop coil. The calculation was obtained twice, for an ROI in the phantom and in the vitamin pill using different interfaces, coaxial coils and preamplifiers.

4.1.2.2 Fruit imaging

The picture of the 3D T_2 weighted double echo image of the orange is shown in Fig. 4.9. The details of the fruit can be clearly distinguished. The skin is more highlighted on the bottom and the left-side of the picture. This shows that the coil was not positioned perfectly in sagittal orientation on the fruit.

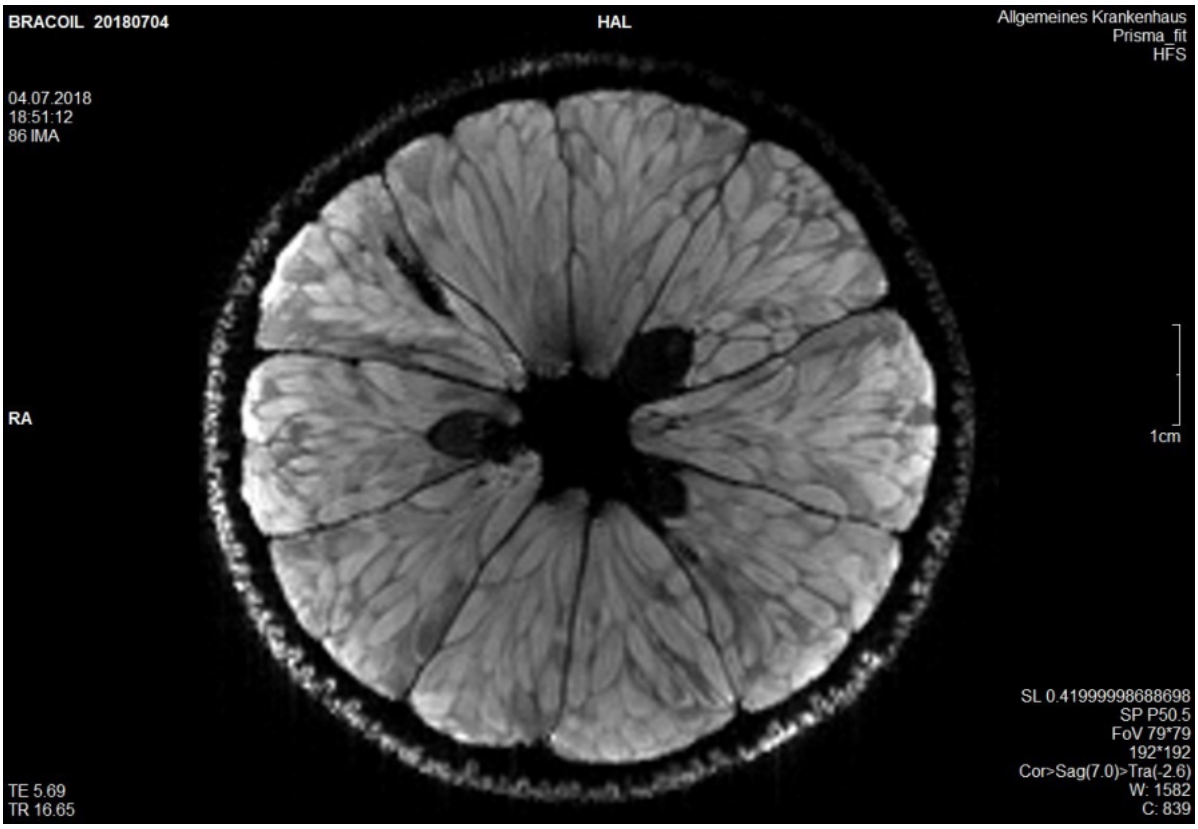

Figure 4.9: MR scan of an orange fruit with the single-channel coaxial coil.

4.2 3-channel coaxial coil array

4.2.1 Bench tests

4.2.1.1 Two-element decoupling

The results of the geometrical decoupling experiment of two coaxial coils on the bottom of the torso phantom with varied coil are shown in Fig. 4.10. The value of the coupling stayed below -22 dB until an approach of around 90 mm (nearly touching coils). Further investigations are necessary for this loosely coupled region since a decreasing coupling with increasing coil distance was expected but not obtained. For a smaller distance between the coils the coupling strength increased strongly with a local maximum around $d \approx 80$ mm and decreased to a local minimum around 65 mm. For even smaller distances between the to coils the coupling strength increased again. Only at a very close approach of around 35 mm the S_{21} peak starts to get broader and split ≈ 30 mm. Two peaks, one below and one above 123 MHz appeared, thus, the curve stopped at this distance.

A second measurement with a smaller step size of the coil distance around the local minimum was performed to determine the minimum coupling strength more precise. The values were slightly different compared to the first chart due to the new experimental setup, but this did not change the position of the minimum coupling. The optimal coupling distance between the coils was found to be between 61 mm and 62 mm. A distance $d_{opt} \approx 62$ mm was therefore

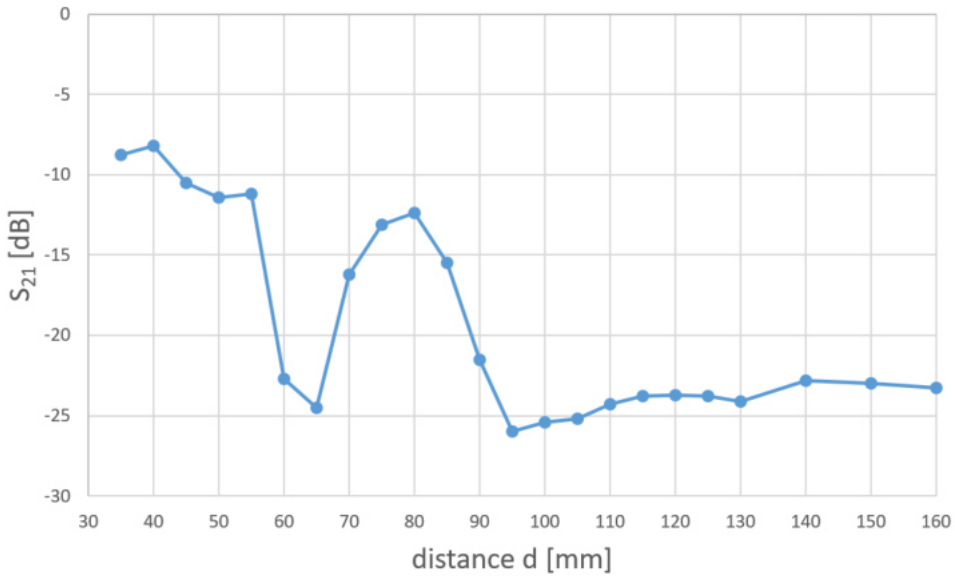

Figure 4.10: Coupling strength measurement obtained for an optimal geometrical decoupling distance d_{opt} between two coils with $d_{coil} \approx 80$ mm.

a)

S_{ij} [dB], flat measurement			
i\j	1	2	3
1	-29.7		
2	-17.6	-48.6	
3	-19.5	-14.5	-30.5

b)

S_{ij} [dB], bent measurement			
i\j	1	2	3
1	-33.7		
2	-16.1	-29.8	
3	-17.4	-14.7	-24.3

Table 4.4: S-parameter matrix obtained for the 3-channel array twice, flat (a) and bent (b).

chosen for the array.

4.2.1.2 Three-element decoupling

The results of the measurement of the S-parameters of the final array in flat and bent position on the phantom are shown in Tab. 4.4. Slightly different values were obtained for both configuration, but the overall behaviour was similar.
Fig. 4.12 shows the S_{ii} parameters, where the index i = 1, 2, 3. In Fig. 4.13 the coupling between two coils, is shown by measuring S_{32}, S_{31} and S_{21}. The decoupling was < -14 dB and matching < -24 dB for all cases, indicating very robust performance.

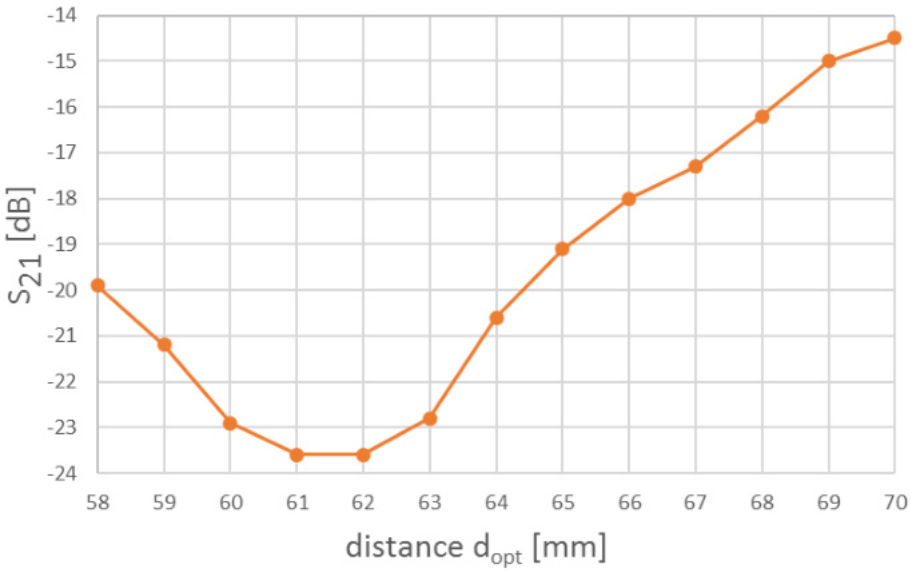

Figure 4.11: Additional measurement of the coupling strength for two coaxial coils with smaller distance step-size near the expected minimum.

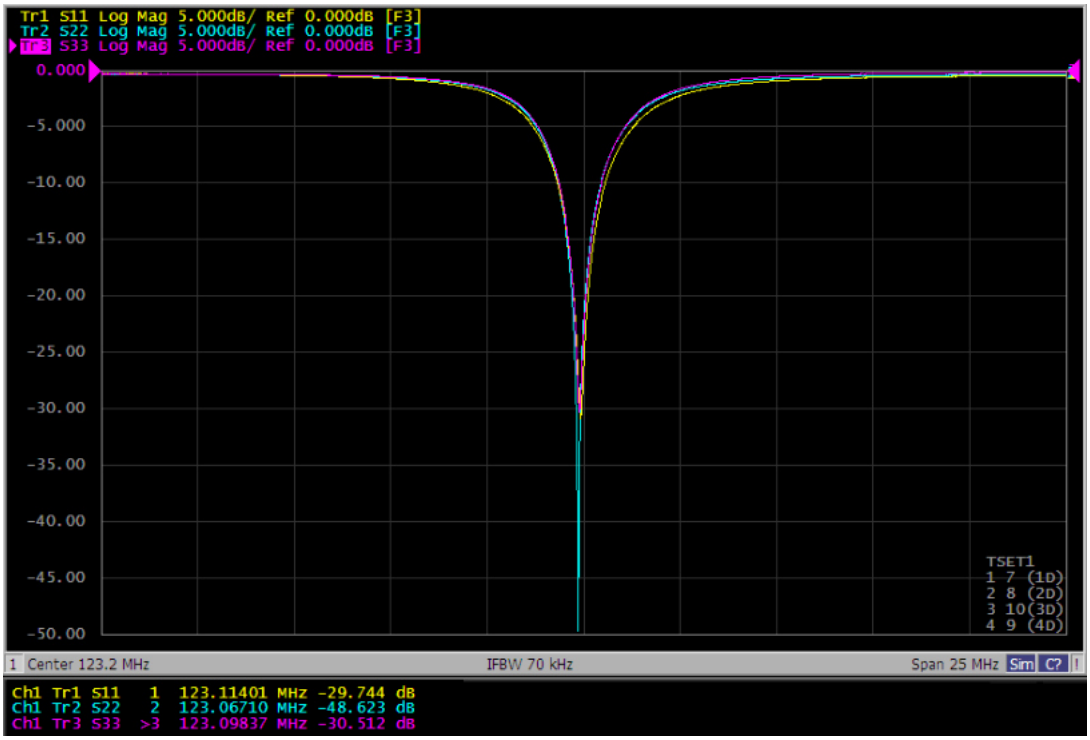

Figure 4.12: S_{ii} parameter measurement for the 3-channel coaxial coil array. The markers at the minimums were not displayed in the chart for better visibility.

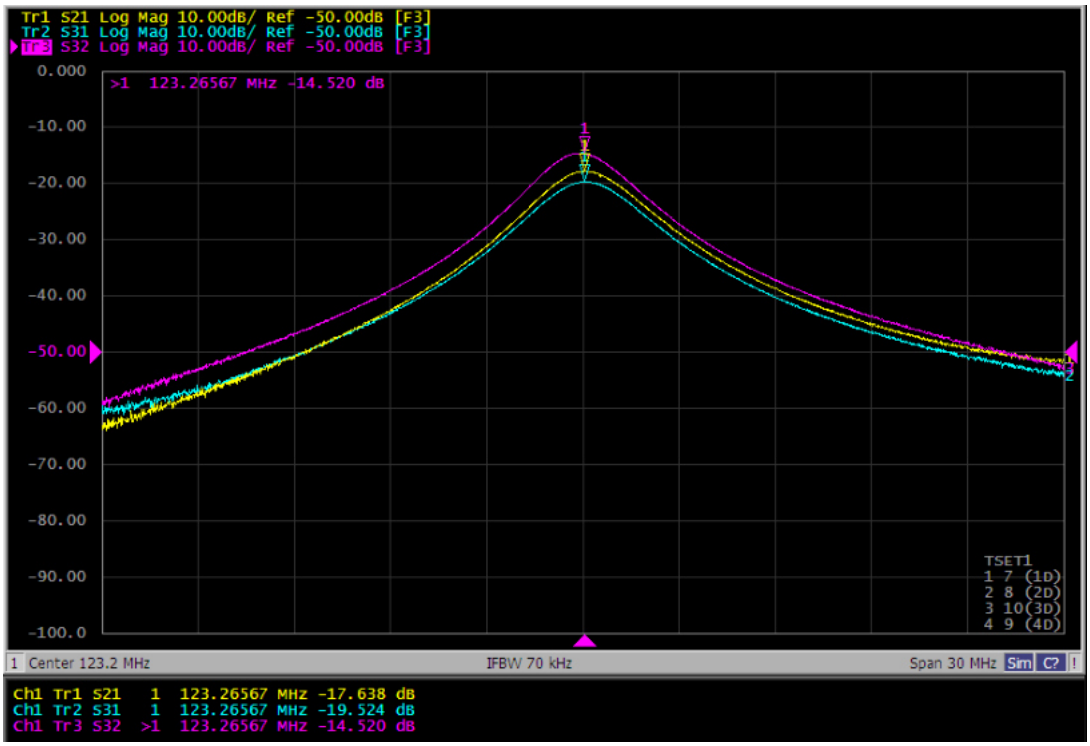

Figure 4.13: S_{ij} parameter measurement for the 3-channel coaxial coil array.

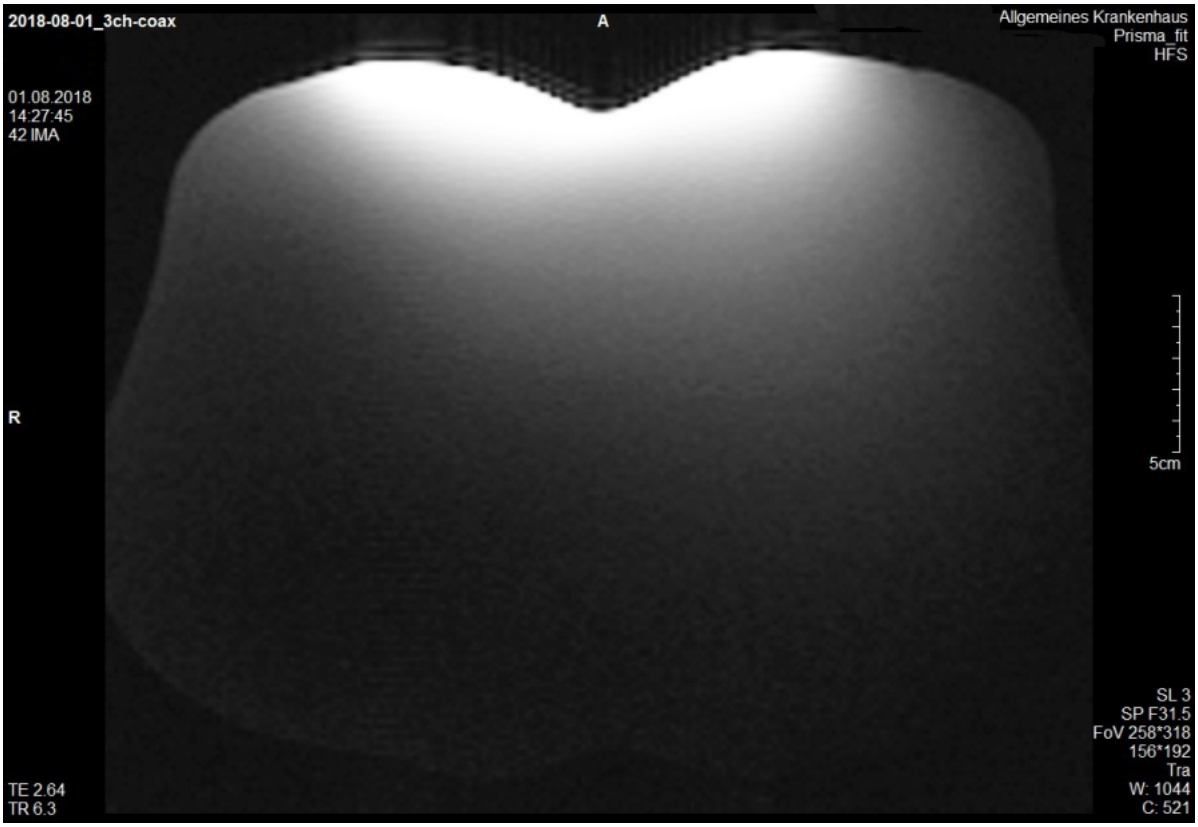

Figure 4.14: Torso phantom image of the 3-channel array.

4.2.2 MR experiments

4.2.2.1 Torso phantom MR experiments

An MR image with the final 3-channel coaxial coil array, as described in Sec. 3.3.3.1 is shown in Fig. 4.14. The noise correlation matrix Ψ is shown in Tab. 4.5. It was calculated from the noise-only data, acquired from the receive coil array without excitation pulse. The correlation values of the different coils were small (< 0.032), this means the coils are very well decoupled. The SNR maps are shown in Fig. 4.15 (coronal) and in Fig Fig. 4.16 (transversal), fully sampled ($R = 1$), and accelerated with $R = 2$, 3. The g-factor maps are only shown for $R > 1$. All maps are shown for right-left acceleration. By accelerating acquisition, artefacts were appearing, which are visible for $R = 2$ close to the center, r.h.s. of the image. For $R = 3$ the artefact is visible a little left to the center. This artefact is due to the very low number of elements in the array. As expected, the SNR values were decreasing with increasing acceleration factor. The g-factor maps are shown below, the values near the coil position are close to 1. The values were increasing with increasing acceleration factor.

Ψ	Coil 1	Coil 2	Coil 3
Coil 1	1.000		
Coil 2	0.036	1.000	
Coil 3	0.035	0.032	1.000

Table 4.5: Noise correlation matrix for the final 3-channel array on the phantom, calculated from noise-only data.

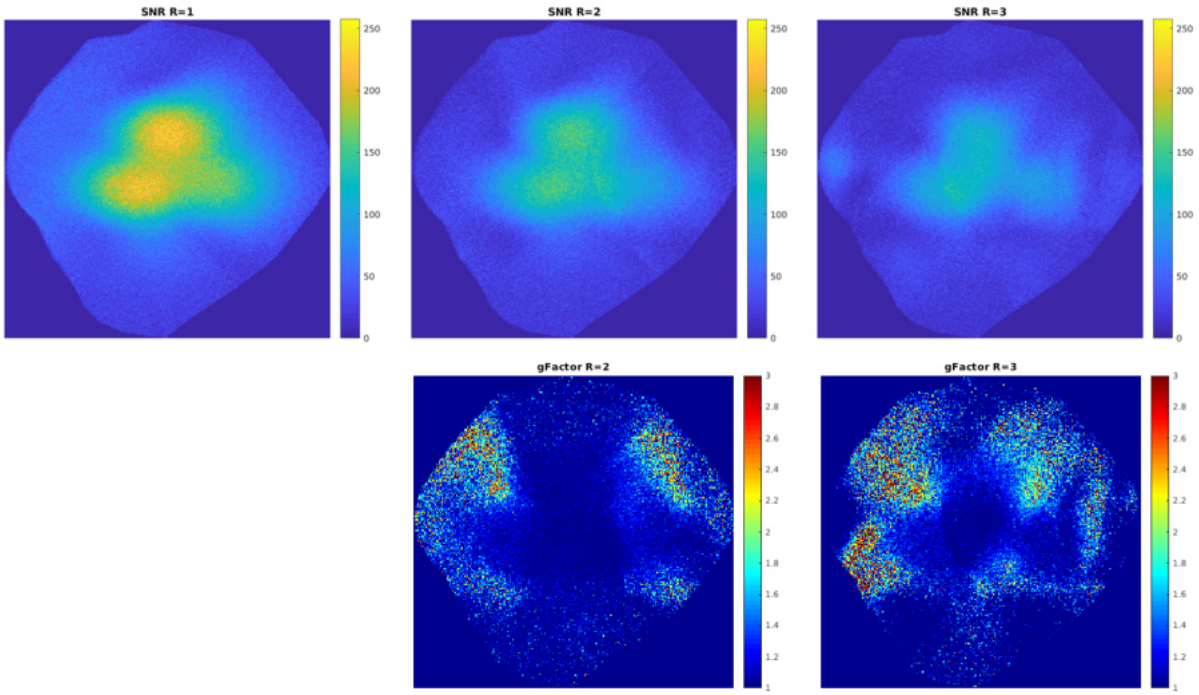

Figure 4.15: SNR maps and g-factor maps for a coronal image.

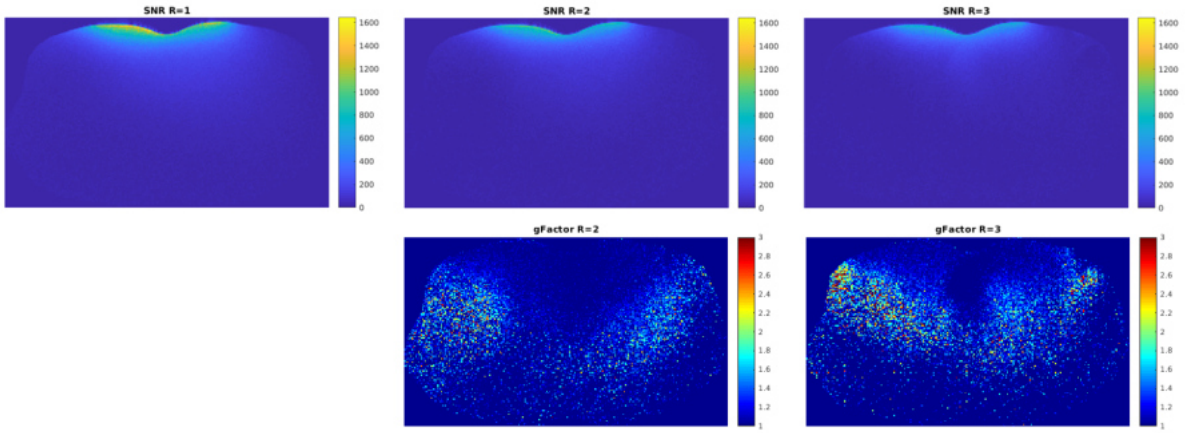

Figure 4.16: SNR maps and g-factor maps for a transversal image.

4.2.2.2 Fruit measurements

The results of the measurement of a pineapple and a watermelon, as described above, are presented.

The images of the transversal and coronal melon scan are shown in Fig. 4.17. In the coronal scan the melon seeds (in the middle of the scan, black), a hyper-intense region close the the seeds (which seems to have a very high water concentration) and the complex fruit body are well depicted. The position of the three coil elements is recognizable by the three bright regions close to the skin at the , and left and right at the bottom of the picture. In the transversal scan the spatial range of the array is visible. Due to the design of a surface array, in the more distant regions only the high-signal area around the seeds is observable. In a maximum intensity projection (Fig. 4.18) of the transversal scan the three elements of the array are pictured. All three elements have a similar brightness.

The MR scan of the pineapple is shown in Fig. 4.19.

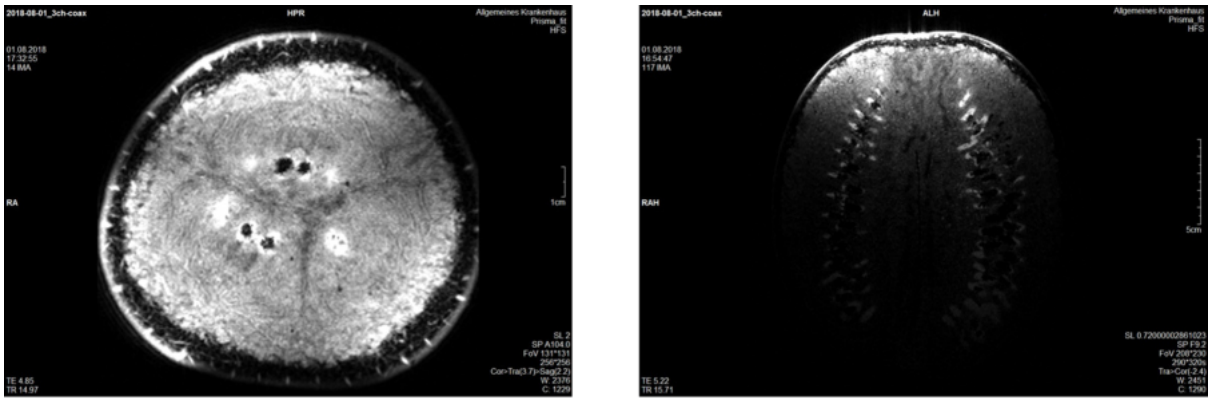

Figure 4.17: Coronal and transversal image of the watermelon.

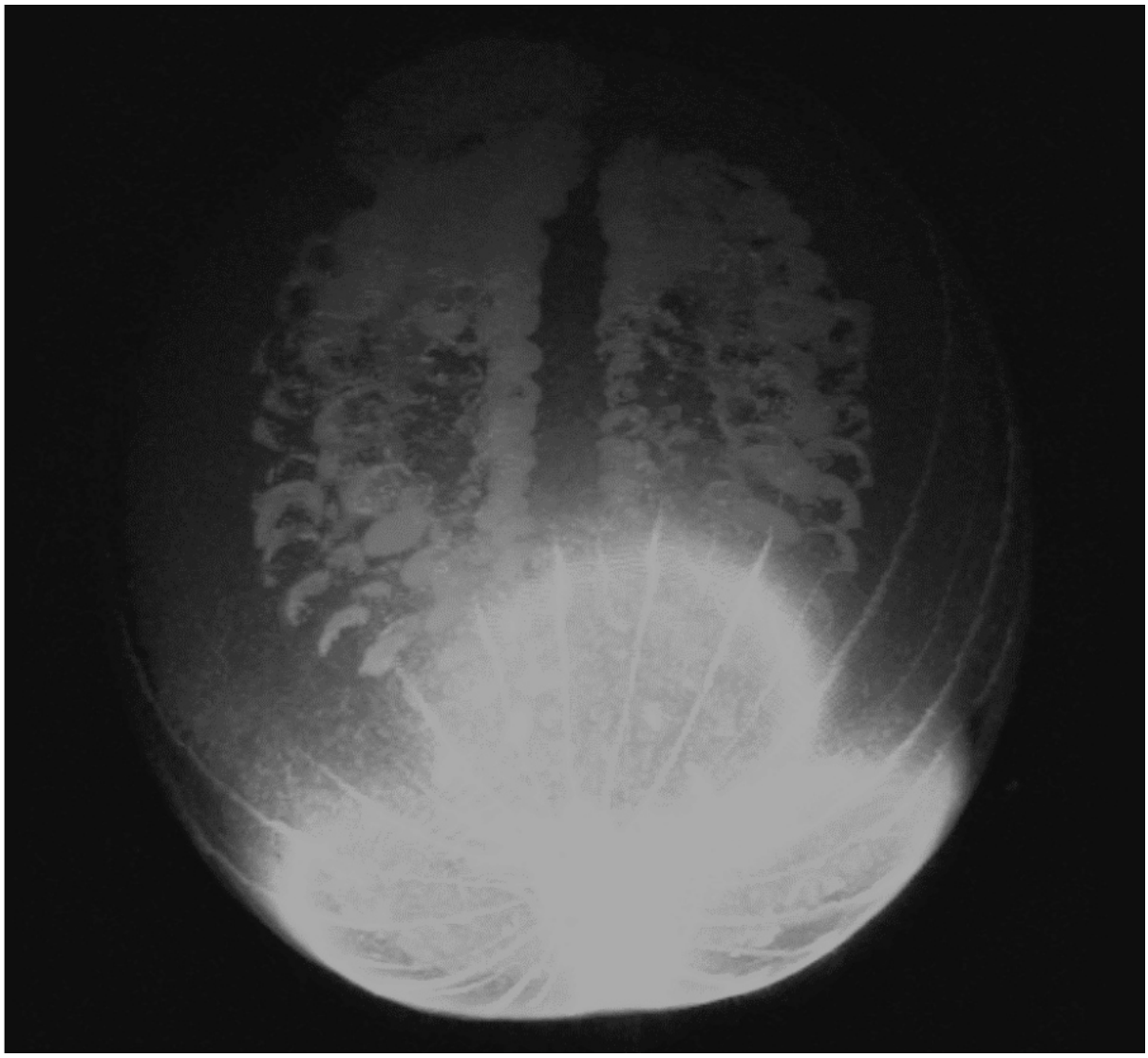

Figure 4.18: Maximum intensity protection of the watermelon.

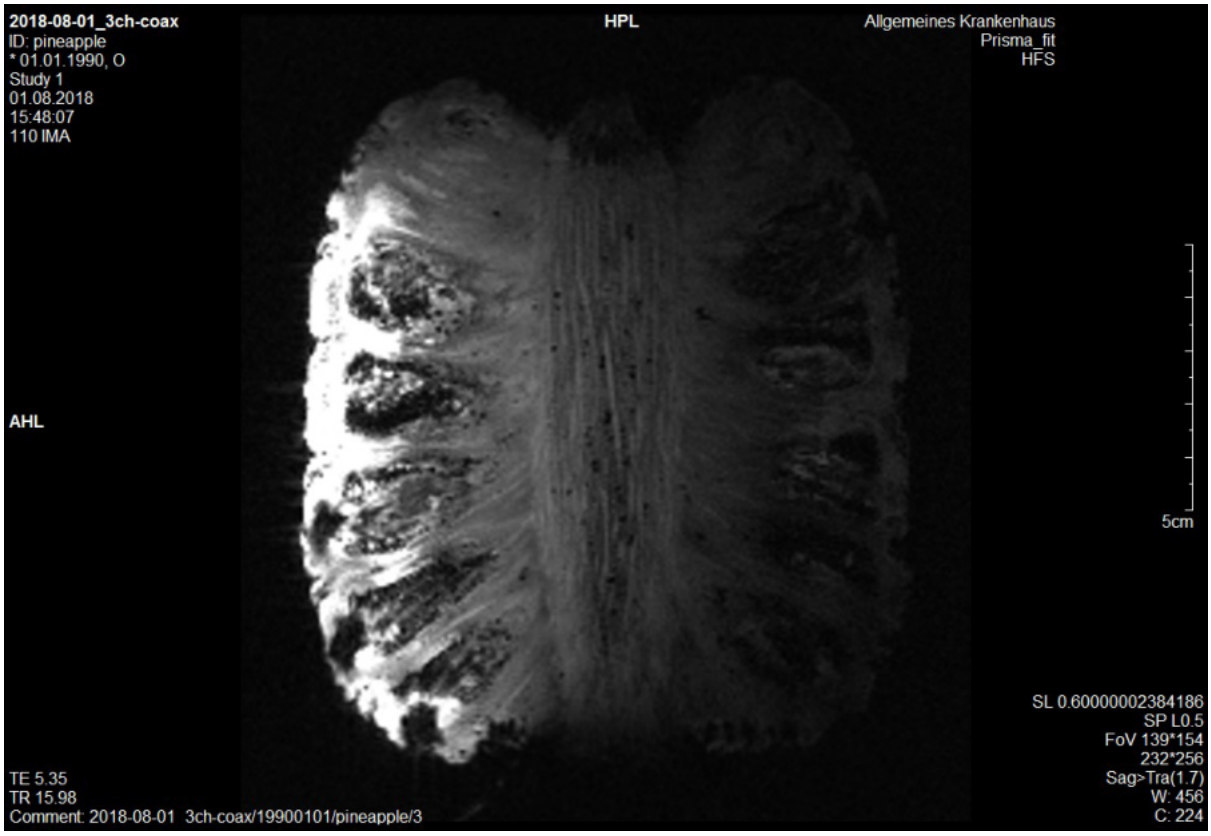

Figure 4.19: MR image of a pineapple with the array located on the side.

Chapter 5

Conclusion

5.1 Summary and discussion

In the presented thesis the successful development of an ultra-flexible 3-channel receive-only coil array made of coaxial transmission line resonators is described. The one-gap coaxial coil array was built for a 3 Tesla magnetic resonance scanner.

Zhang et al. [6] introduced a theoretical model describing the resonance frequency of the coaxial coil, which is only valid for the one-gap coaxial coil. If a particular cable is chosen, a fixed diameter is related to each RF frequency, respectively. To overcome this limitation, the model was extended to a multi-gap coaxial coil model.
The built 3-channel array consists of three coaxial coils with a diameter of 80 mm. Each coil was built from a thin, very flexible coaxial cable with a wire diameter of around 1.2 mm. The cables were prepared with one gap. An interface consisting of tuning, matching and preamplifier decoupling, was developed and studied in detail. By comparing it to the software Pasan, the theoretical description could be compared to reality. Overall, a good agreement of the modules and the theoretical description was obtained. Three similar compact interfaces were built. Three low input impedance and low noise figure preamplifiers were used for amplifying the received signal. For the array design the center of the coil elements were positioned at the corners of an equilateral triangle with a side length of ≈ 62 mm to obtain an optimal geometric decoupling. This value was experimentally determined and it is similar to the theoretical optimal overlap distance for conventional loop coils. However, peak splitting at the resonance frequency was appearing only for a very close approach of 30 mm and below. The coils were woven into a wide-meshed textile which was sewn to additional textile layers for protection and stability.
Several performance tests were executed: Firstly, the single-channel coaxial coil was studied. The resonance frequency f_0 changed only slightly ($\approx 3\%$) between a circular and an elliptic shape. f_0 increased approximately linearly with the number of gaps. The quality factor ratio between unloaded and loaded configuration was measured for the coaxial coils and it increased strongly with the number of gaps. By comparing the values to a standard loop coil it was

found that the ratio was higher for the conventional coil. For the coaxial coil a considerable difference of Q-ratio was found with and without an interface. This behaviour indicated that losses occurred in the electrical circuit of the interface which are not neglectable. Due to the small sample noise dominance, the signal to noise ratio was also reduced: the single-channel MR measurements showed that the SNR was around 1.3 to 1.4 times higher for the standard coils. Additional single-channel measurements with an orange demonstrated an overall well-functioning receive coil.
Secondly, bench tests of the implemented array were performed: The geometrical decoupling of three element array was executed on a flat position of the phantom. The obtained S-parameters showed a good decoupling at the resonance frequency. The S-parameter matrix was also obtained on a bent position on the phantom. It was found that the S-parameter matrix behaves similarly for both setups, which points out the flexibility of the coaxial coil array. Final MR test measurements of the 3-channel array were performed. A good decoupling of the array was confirmed with the calculation of the noise correlation matrix Ψ with values below 3 - 4 %. The geometry factors for an acceleration of $R = 2$ and $R = 3$ were calculated using Ψ. Due to the small number of elements within the array, artefacts were occurring. Overall, close to the array the g-factor stayed small, even for an acceleration factor of 3. Further MR test measurements were performed using a watermelon and a pineapple. Both fruits were well depicted, a similar performance of each of the three coil elements was obtained.

5.2 Outlook

Although the SNR was a little higher for conventional loop coils compared to coaxial coils, coaxial cables prepared with gaps of the inner and outer conductor depict a very promising new development in RF coil development. The source of the rather large losses observed from the interfaces will be subject of further investigations. Also, even with slightly decreased or equal SNR performance, the flexible nature of the coaxial coil array might lead to an overall increased SNR, since it can be positioned more tightly to the region of interest, in particular when the body geometry exhibits strong intersubjective variation. The extended theoretical model of the multi-gap coaxial coil can be even further extended by changing the number of turns of the coil. This is under current investigation in our group. The mechanical flexibility of the coaxial coils in combination with the possibility to robustly decouple the elements of the array, even in a strongly bent position is one of the major advantages of this self-resonant coil type. In combination with their small weight, such coaxial coils could be optimally suited for various applications. One of these is the so-called BRACOIL-project, which is a following study of the new coils with the aim to develop a 32-channel array for breast magnetic resonance imaging. The idea is to implement a receive-only one-gap coaxial coil array for 3 Tesla on a T-Shirt-like textile, which can be easily worn by the patient without additional devices, to be used in supine position (face-up) in the scanner. This represents a change of the standard position for breast MR, which is nowadays the prone position (face down). Advantages are among others the enhanced patient comfort, but the changed position also comes with a major

challenge created by body-motion due to breathing of the patient. Motion sensors will be placed at several positions in the array to detect the motion and extract it from the scanned image. BRACOIL is an FWF funded joint project with ANR (France); the 32-channel array will be developed in Vienna, the motion sensor technology is investigated by our project partners in France at the University of Lorraine in Prof. Jacques Felblinger's group.
The new coaxial coils could also be studied in other interesting research topics such as ultra-high field MR. It has to be kept in mind, additionally to the receive signal it must be taken care of the transmit signal. Especially for the thin coaxial coils this would have to be studied in detail, due to the high current in the transmitting process which could destroy the coil.

Bibliography

[1] E. M. Purcell, H. C. Torrey, and R. V. Pound, "Resonance absorption by nucelar magnetic moments in a solid," *Physical Review 69: 37-38*, 1946.

[2] F. Bloch, W. W. Hansen, and M. Packard, "The nuclear induction experiment," *Physical Review 70: 474*, 1946.

[3] D. K. Sodickson and W. J. Manning, "Simultaneous acquisition of spatial harmonics (SMASH): Fast imaging with radiofrequency coil arrays," *Magnetic Resonance in Medicine 38(4): 591-603*, 1997.

[4] K. P. Pruessmann, M. Weiger, M. B. Scheidegger, and P. Boesiger, "SENSE: sensitivity encoding for fast MRI," *Magnetic Resonance in Medicine 42(5): 952-62*, 1999.

[5] M. A. Griswold *et al.*, "Generalized autocalibrating partially parallel acquisitions (GRAPPA)," *Magnetic Resonance in Medicine 47(6): 1202-10*, 2002.

[6] B. Zhang, D. K. Sodickson, and M. A. Cloos, "A high-impedance detector-array glove for magnetic resonance imaging of the hand," *Nature Biomedical Enineering 2: 570–577*, 2018.

[7] W. Demtröder, *Experimentalphysik 3. Atome, Moleküle und Festkörper.* Springer-Verlag Berlin Heidelberg New York, 2005.

[8] R.W.Brown, Y.-C. N. Cheng, E.M.Haacke, M. Thompson, and R.Venkatesan, *Magnetic Resonance Imaging. Physical Principles and Sequence Design.* John Wiley and Sons, Inc., Hoboken, New Jersey, 2014.

[9] M. F. Reiser, W. Semmler, and H. Hricak, *Magnetic Resonance Tomography.* Springer-Verlag Berlin Heidelberg, 2008.

[10] P. Robson, A. Grant, A. Madhuranthakam, R. Lattanzi, D. Sodickson, and C. McKenzie, "Comprehensive quantification of signal-to-noise ratio and g-factor for image-based and k-space-based parallel imaging reconstructions," *Magn. Reson. Med. 60(4): 895-907*, 2008.

[11] J. Mispelter, M. Lupu, and A. Briguet, *NMR Probeheads for Biophysical and Biomedical Experiments.* Imperial College Press, London, 2006.

[12] J. T. Vaughan and J. R. Griffiths, *RF coils for MRI.* John Wiley and Sons Ltd, United Kingdom, 2012.

[13] P. B. Roemer, W. A. Edelstein, C. E. Hayes, S. P. Souza, and O. M. Mueller, "The NMR phased array," *Magnetic Resonance in Medicine 16(2): 192-225*, 1990.

[14] P. Gonord, S. Kan, and A. Leroy-Willig, "Parallel-plate split-conductor surface coil: Analysis and design," *Magnetic Resonance in Medicine 6: 353-8*, 1988.

[15] S. Serfaty, N. Haziza, L. Darrasse, and S. Kan, "Mulit-turn split-conductor transmission-line resonators," *Magnetic Resonance in Medicine 38(4): 687-9*, 1997.

[16] R. Frass-Kriegl *et al.*, "Multi-turn multi-gap transmission line resonators – concept, design and first implementation at 4.7 T and 7 T," *Jornal of Magnetic Resonance 273: 65-72*, 2016.

[17] R. Ludwig and G. Bogdanov, *RF Circuit Design. Theory and Applications*. Pearson Education, Inc, New Jersey, 2009.

[18] Wikipedia, "Smith chart." `https://en.wikipedia.org/wiki/Smith_chart/`, 2018. [Online; accessed 08.08.2018].

[19] Website-Science4all.nl, "Impedance calculation software pasan." `http://science4all.nl/?Electronics`, 2018. [Online; accessed 15.10.2018].

[20] L. Darrasse and G. Kassab, "Quick measurement of nmr-coil sensitivity with a dual-loop probe," *Review of Scientific Instruments 64: 1841*, 1993.

[21] K. Lange and K.-H. Löcherer, *Taschenbuch der Hochfrequenztechnik*. Springer-Verlag Berlin Heidelberg GmbH, 1986.

[22] D. A. Seeber, J. Jevtic, and A. Menon, "Floating shield current suppression trap," *Concepts in Magnetic Resonance Part B Magnetic Resonance Engineering 21B(1): 26 - 31*, 2004.

[23] Webside-Microwaves101, "High-pass low-pass phase shifters." `https://www.microwaves101.com/encyclopedias/high-pass-low-pass-phase-shifters`, 2018. [Online; accessed 28.08.2018].

List of Figures

List of Tables